KAUNAS UNIVERSITY OF TECHNOLOGY

TAUTVYDAS FYLERIS

THE DEVELOPMENT OF ULTRASONIC ADAPTIVE METHOD FOR INSPECTION OF OBJECTS WITH COMPLEX GEOMETRY

Doctoral dissertation
Electrical and Electronic Engineering, Electronics (T 001)

2020, Kaunas

The doctoral dissertation was prepared at Kaunas University of Technology,
Prof. K. Baršauskas Ultrasound Research Institute during the period of 2014–2019.

Scientific Supervisor:
Prof. dr. Elena Jasiūnienė (Kaunas University of Technology, Electrical and Electronic Engineering – T 001)

The doctoral dissertation has been published in:

http://ktu.edu

Editor:

Dr. Armandas Rumšas (Publishng Office "Technologija")

KAUNO TECHNOLOGIJOS UNIVERSITETAS

TAUTVYDAS FYLERIS

ULTRAGARSINIO METODO SUDĖTINGOS GEOMETRIJOS OBJEKTAMS TIRTI SUKŪRIMAS

Daktaro disertacija
Technologijos mokslai, elektros ir elektronikos inžinerija (T 001)

2020, Kaunas

Disertacija rengta 2014–2019 metais Kauno technologijos universiteto Prof. K. Baršausko ultragarso mokslo institute.

Mokslinis vadovas:

Prof. dr. Elena JASIŪNIENĖ (Kauno technologijos universitetas, technologijos mokslai Elektros ir elektronikos inžinerija, T 001)

Interneto svetainės, kurioje skelbiama disertacija, adresas:
http://ktu.edu

Redagavo:

Dr. Armandas Rumšsas (leidykla "Technologija")

CONTENTS

NOMENCLATURE AND ABBREVIATIONS

ADC	Analogue to Digital Converter
A-scan	time-Amplitude Scan data
B-scan	Brightness amplitude scan or stacked line-by-line multiple A-scans
B-Spline	Basis Spline
CAD	Computer-Aided Design
CGAL	The Computational Geometry Algorithms Library
C-scan	Compound scan
CUDA	A parallel computing platform and application programming interface model created by Nvidia Corporation
DAC	Digital to Analogue Converter
DAS	Delay And Sum
DAX	Dual Apodization with cross-correlation
EIBMV	EIgenspace-Based Minimum Variance
ERM	Exploding Reflector Model
FE	Finite Element
FEA	Finite Element Analysis
FEM	Finite Element Method
FMC	Full Matrix Capture
FP32	The IEEE standard for floating-point arithmetic single-precision floating-point format using 32-bit storage space
FSI	Fluid-Structure Interaction
GPGPU	General-Purpose computing on Graphics Processing Unit
GPU	Graphics Processing Unit
IEEE	Institute of Electrical and Electronics Engineers
MAX	Multi-Apodization with cross-correlation
MDAS	Multiply Delay And Sum
MUSIC	MUltiple SIgnal Classification
MV	Minimum Variance
NSI	Null Subtraction Imaging
NURBS	Non-Uniform Rational B-Spline
PRF	Pulse Repetition Frequency
PSF	Point Spread Function
PWI	Plane Wave Imaging
ROI	Region Of Interest
SAFT	Synthetic Aperture Focusing Technique
SDH	Side Drilled Hole
SIMD	Single Instruction, Multiple Data
SIMT	Single Instruction, Multiple Threads
TFM	Total Focusing Method
UT	Ultrasound Testing
VSA	Virtual Source Aperture

INTRODUCTION

Motivation and relevance of work

The inspection of various components for defects or structural integrity is a critical procedure for such industries as aerospace, construction, or nuclear energy [1]–[3]. There are many inspection methods employed, such as using a laser [4]–[6], X-ray [7], [8], destructive testing [9]–[13] or acoustic ultrasound [5], [14]–[17]. All the presently mentioned methods have their strengths and weaknesses, and the selection of a specific method usually depends on the working environment. For example, in the case of inspection of larger structures, such as bridges, the X-ray probably will not work effectively. For practical *in-situ* inspections, portable inspection methods must be used, and one of the most widely used techniques is ultrasound testing (UT). With current advancements in technology miniaturization [18], probes and devices can be easily handled, which is advantageous in hard-to-reach places.

Comprehensive UT inspection [15], [18], [19] is a readily available method which has the advantage of not using ionizing radiation, offers relatively good penetration into an object, and can be electronically steered with phased array transducer.

As the defect inspection by using ultrasound can be summarized as interpreting reflected echoes [5] or the absence of them, the physical wavefront and reflection paths have to be known in order to extract the position information. As for the wave path propagation modeling, it is a complicated process when reflected data contains signals from the walls as well as structural noise. Additionally, an acoustic wave need to cross the boundary between testing the object and the environment (water or air) which can be complex, irregular, or organically shaped, where the direct analytic approach for the path model is not practical [20]. It is one of UT inspection problems which is not fully answered when it is necessary to have good penetration and information on the position.

The central part of UT inspection is signal generation and, then, listening to echoes. There are two standard modes for signal transmission and reception: using the same transducer for emission and reception (pulse-echo), and the pitch-catch mode where different sensors are used for the emission and reception or various combinations of them for ultrasonic tomography [21], [22]. As for pulse generation, various types are proposed, such as the Gaussian pulse [23]–[25], chirp (signal sweep) [26]–[28] or a complex modulated signal [29]–[33]. One of the most popular options is the Barker code [34], and, if used with multiple transducers (such as the phased array), emission can be made with various combinations of signals. As for quick classification acoustic emission, it can be divided into modulated and unmodulated signals. In the commercial equipment (such as *Gekko M2M* [35], *Dasel SITAU* [36], *Omniscan MX2* [37]), usually, signals are limited to the Gaussian pulse with time delay because of cost considerations [23].

In order to obtain good inspection results, knowledge of the accurate acoustic path of the signal is needed. For an object without planar surfaces (such as being of an organic shape), the path can be very complicated, and there is no easy direct

analytic method to calculate it; yet, Snell's law can provide correct angles. One of the reasons is that the Snell law only gives results for a single ray angle or a wavefront, while completely ignoring the wave spread. Another reason is that the reflected signal can have multiple signal paths back to the sensor. Although, for regular geometry inspections, methods have already been developed [38]–[43], they assume that the boundary between the object and coupling medium is flat, or at least surface deviation will have little impact. When refraction or mode change effects have a significant influence on the interpretation of echoes, inspection can be reduced to finding the presence of defects by using autofocusing methods [44]–[46] or by using only B-scan raw data. On the other hand, autofocusing without external information will only concentrate energy on to the reflector. Various methods can achieve this, such as Time Reversal (TR) [47]–[50], or Minimum variance (MV) focusing [42], [51]–[53]. In other words, the knowledge of the object boundary surface morphology is required in order to find accurate information about a defect.

A flexible UT inspection solution is to use phased arrays as it is possible to create a universal inspection method [38], [44], [45], [54]. First, the transducer can be flexible and can be held against an object's surface [55]–[57]. However, as mentioned before, tracing back the position information of reflections (defects, object bottom or sides) is not a trivial problem. Another form of phased transducer flexibility comes from the fact that focusing in practice is energy concentration, as the main job of an acoustic lens is to delay a wave's traveling time enough to concentrate energy in the area of interest. Focusing can then be achieved by using electronic steering [58], which alleviates the problem of creating various-shaped physical lenses, albeit with a lower reception quality.

Fortunately, when using phased arrays, the interpretation of echoes becomes more extensive due to the ability to record and send signals from different physical positions and because of the employment of various mathematical processing methods. Yet, there is a configuration of the object surface curvature where it is physically impossible to have a sensible reflection, even with a phased array where a wide range of signals can be detected. However, in practice, when there is little or no information about reflection, an assumption is made that acoustic waves will reflect as if from an infinitely small point in all directions with the same amplitude [40], [59]–[61]. It is a mathematical simplification of wave propagation which can be derived from wave equations, and it is known in literature as the exploding reflector model (ERM) [47], [52], [62]–[64]. It works perfectly for reconstructing reflections when there is only one medium of information that can be reconstructed by using straightforward mathematics and when there is only one inversion solution. Hence, in practice, any focusing method can be used, such as frequency domain-based or statistics-based methodologies, which dramatically decrease the computing time. However, these methods start to provide false results when the defect's response signals are correlated and cannot be easily separated, or when there is a reflection from walls which forms multi-path reflections – in other words, there is no one-to-one mapping relationship between signal timings. This problem becomes more complex when more prominent distortion occurs in acoustic waves due to non-regular surfaces. One of the more straightforward solutions is to filter weaker multi-path signals and

only work with the strongest one or few signals, but it is not always possible to reliably separate different signals [65], [66].

A solution when there is substantial interference from multipath and irregular curvature is a complex problem which is not yet entirely solved. One of the solutions is, as discussed earlier, to calculate the acoustic path between water (for the case of immersion) and the object's surface, e.g., when performing the measurement with the adaptive total focusing method (ATFM) with an assumption of the direct and single path [67]. Another method when trying to solve the adaptive part of the object is by using the virtual transducer model [31], [38], [54], [68], [69]. The virtual transducer model is usually preferred when the objects for inspection have a relatively low curvature where there are no abrupt effects in acoustic propagation. For entirely irregular surfaces with a huge number of the multipath of rays, it is difficult to determine the acoustic path with minimal information. However, with phased arrays using many elements or with a wide aperture, it is possible to reconstruct objects with various curvatures.

Inspection of various objects by using only a phased array has the advantage of being able to fully reconstruct objects with non-planar surface profile at a relatively fast time. As it can be seen, one of the advantages of this model is that the inspection can be done *in-situ* and without knowledge of surface profile. Although there are commercial offerings for this type of problem, usually, it is still preferable to do a reconstruction of the surface with a low curvature related to the wavelength and to use a narrow aperture for the reconstruction of data.

Scientific and technological problem. Working hypothesis

By using high-frequency immersion ultrasonic phased arrays (which have center frequency f between 1 MHz and 20 MHz), it is possible to achieve defect position coordinates with an uncertainty error of 1 mm in case of inspection of objects with non-planar surface curvature.

Research aim and object

This research aims to develop methods for the reconstruction of the surface morphology and of the positions of defects by using phased arrays in case of investigating objects with complex geometry when wave propagation solutions are very complicated, or even impossible to solve, due to multiple acoustic paths.

The object of this research is the inspection of solid objects with non-planar surfaces by using high-frequency ultrasonic immersion phased array transducers, and *a priori* information is only the speed of sound in the surrounding medium and the object. The detection results yield the object surface model and the physical position of the defect.

Research tasks

1. Perform the literature review of ultrasonic methods for the detection of defects in objects with surfaces featuring complex geometry;
2. Create and investigate the method for the reconstruction of surface morphology;
3. Create and investigate the method for inner structure reconstruction when surface morphology information is algorithmically obtained;

4. Numerically verify the proposed methodology for surface morphology and volume reconstruction;
5. Experimentally verify the proposed methodology for object inspection and inner structure reconstruction.

Scientific novelty

In this thesis, a new methodology for the inspection of objects with non-regular surfaces is proposed, whereby the developed algorithm automatically adapts to the object surface morphology by using focused ultrasonic data from automatic environment probing. Robust methods are developed for the reconstruction of extreme surface curvature, although, practically, the volume reconstruction is not always possible. Methods are proposed for analytic reconstruction of the surface directly from signals. After gathering the surface morphology information, the inner structure of the object is reconstructed by using the proposed algorithm.

Practical value of the work

The created algorithms and the proposed methodology allow inspections in industry-relevant applications (defect characterization, high-temperature hydrogen attack, porosity detection) where localization information is necessary when a sample of interest features a non-regular surface without accurate computer model information, e.g., such technical components as: turbine blades, axles or other complex-shaped industrial parts.

Approbation

The results of the dissertation were published in two publications: two papers were published in periodic foreign journals referred in the *Journals of the Master List of Thomson Reuters Web of Science*. The results were also presented at two international scientific conferences.

Structure and content of the thesis

The thesis consists of an introduction, five chapters, general conclusions, the reference list, and the list of publications by the author. The dissertation chapters are organized as follows:

- In **Chapter 1**, a review of the standard methods for UT inspection and focusing is presented. The primary aim of the review is the investigation of the reconstruction of the position of defects in 2D space in the dual-medium environment.
- **Chapter 2** discusses and proposes a methodology for surface morphology reconstruction. It is divided into two parts: when an object can be of any form, such as organic forms, and created from planar segments.
- In **Chapter 3**, the characteristics and the proposed methodology are presented for the volume reconstruction of non-regularly shaped objects, and the methodology for numerical investigation is reviewed.
- In **Chapter 4**, numerical evaluation of the proposed methodology is presented, and the model accuracy is investigated with numerical experiments.

- In **Chapter 5,** the experimental investigation is presented with similar to real life samples, which enables to evaluate the proposed methodology.

The overall dissertation volume is 110 pages, including 43 figures, 17 tables, 76 formulas, and 251 bibliographic references.

1 ULTRASONIC INSPECTION BY USING PHASED ARRAYS

Ultrasonic phased arrays were created with advances in computing power. They started to become practical with the introduction of relatively fast processors because using a single transducer with a straightforward acoustic model (delaying signals by its travel path and coherently adding signals [70], [71] or using correlation [72]) does not require advanced signal processing in relative terms [73]. In a typical case, just using an oscilloscope screen is enough, but the visualization of the signal is not easy when using a phased array transducer.

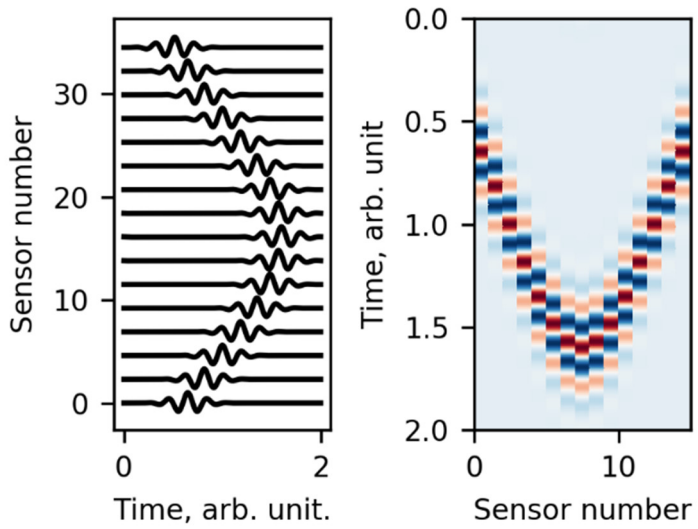

(a) (b)

Figure 1.1 Example of phased array reflection signals: (a) – time amplitude trace (A-scan) and brightness amplitude trace (B-scan)

For example, just from the first glance (Figure 1.1), it is evident that even when showing a modest 16-signal line on an oscilloscope screen, it is not easy to interpret the data. However, if it were possible to process data, it would be much easier to work with echoes, and even a modest brightness amplitude scan (B-scan) offers more visual information.

From the point of view of analogue systems, the possibility of having multiple transmitting elements made it possible to achieve dynamic focusing (so-called electronic steering), which visibly overcame the limitations of a single focused element, albeit at the cost of losing some emitted signal wavefront accuracy. From the physical point of view, having multiple elements transmitting in the case of phased array beams increases the number of problems instead of eliminating them. Even with a higher manufacturing cost and inferior signal quality, with enough computing power, more can be done than with a single, inflexible transducer.

Yet, there is a limit on how a small scatterer (defect) can be interpreted. The defect detection limit is known as the classical resolution limit, and, in an imaging system, it is known as the diffraction limit [74]:

$$d = \frac{\lambda}{2n\ sin\theta} \tag{1.1}$$

where d is the diffraction limit (the minimum feature size in wavelength units), λ is the wavelength, n is material refraction which depends on the material and the lens limit, and θ is the angle between the sensor element and ROI. The classical interpretation will show that any features smaller than half wavelength will be distorted and blurred.

An ultrasonic transducer has an additional property apart from the center frequency, and the bandwidth offers a directivity pattern.

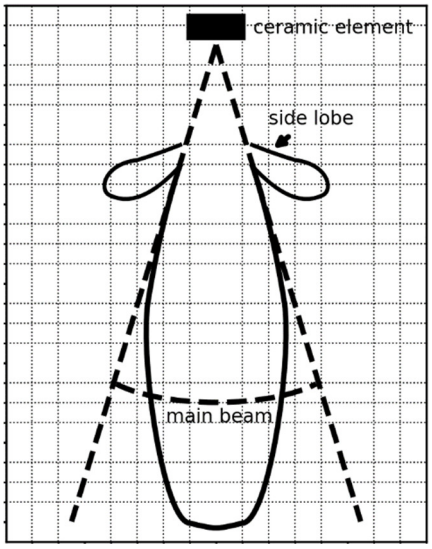

Figure 1.2 An ultrasonic transducer consisting of a ceramic element giving a simplified emission directivity pattern [17], [75]–[77]

Without using complicated math, the directivity pattern can be generally drawn, as shown in Figure 1.2, although directivity is dependent on the quantity of frequency, the radiating area diameter, and the type of the elements [76]. For a single transducer element, when there is necessity to gain the maximum possible information, the directivity property needs to be known. The directivity and sensitivity of a transducer with a relatively simple geometry (circular, rectangular, elliptical) can be mathematically approximated, for example, by using Bessel functions [78]–[81]. On the other hand, because of the dependence on frequency, it is more practical to numerically calculate the emission wavefield even when taking into account a theoretical model of the inspected object, in which, the field is calculated by using various software [82]–[84].

A transducer's frequency response information with a dependence of direction is sometimes called in literature as *sensitivity* [75], [85], [86]. The main usage of

transducer sensitivity information is to reject the signals with too low SNR, as, in practice, more resolution is achieved with a better SNR. The sensitivity processing step is called apodization/shading.

Detailed information about the emission beam pattern and sensitivity map can be significantly achieved with signal equalization [87]–[89]. However, such information requires huge storage capabilities as every point of the inspection grid (at least in ROI points) needs to be calculated (with the exception, for very regular shapes). Although, in practice, it can be approximated with Bessel [78] functions or when using a simple angle filter with a hard threshold to cut all signals outside of the permitted angles (for example, 30 degrees).

The necessity to use numerical methods for acoustic path calculation is taken from the practical point of view because, as mentioned before, there are complex interactions in the physical nature of wave propagation. The most accurate method for acoustic evolution calculation is to use the finite element method (FEM) modeling, albeit it is a resource-intensive task [90]–[92]. In order to decrease calculation time, alternative methods are created:

- KZK (Khokhlov–Zabolotskaya–Kuznetsov) equation, [93]–[95] based on Navier–Stokes differential wave approximation [14] provides a good approximation for acoustic phenomena, albeit the propagated signal is required to have zero mean and needs to be periodic in relation to one axis (a continuous wave).
- The pseudo-spectral method [94], [96]–[98] which is, for example, implemented in the k-Wave software is a fast method for wave propagation modeling if only direct acoustic phenomena need to be considered, for example, nonlinear effects produced in the medium due to heterogeneity are not taken into account.
- Tupholme-Stepanishem method [77], [82], [99], [100] which is used in Field II software is based on the idea of linear systems when finding the spatial response of a space point if apodization is necessary, and a huge number of small points need to be used for calculations.
- The pencil method [83], [101]–[104] is used in CIVA software, and the main advantage is its similarity with raytracing as it models the acoustic propagation path by using rays. For high-quality phenomena numerical results, a lot of rays are required, which will increase the computing time.

Wave propagation can be affected by signal modulation as well; however, the main aim is to increase signal penetration into sample to make it easier to interpret the reflections. Depending on the radar's domain, multiple modulation forms are created:

- One type is the chirp modulation [26], [28], [28], [105]. It is the frequency sweep for the emission and the matched filter for the reception. Due to the sensitivity of the frequency shifts, it has benefits for ultrasounds imagining, although sidelobes in sensors must be below the dynamic range of the image for acceptable performance.
- Digitally coded signals [27], [31], [106], [107] are denoted by the main drawback which is the lower resolution for increased SNR; for transmission

a coded sequence of signals and similar idea to chirp is used, but the signal decoding procedure depends on the signal type, for example, when using Golay or Barker codes [27], [106], that is, the matched filter, whereas Hadamard sequences [31], [108]–[110] use the matrix inverse approach.

In an ultrasound system, usually due to the complexity of the pulser [25], [111]–[115] and the physical phenomena, a high-voltage spike pulse is preferred as it creates vibration in piezoelectric elements at a harmonic frequency [23], [24], [105], [116], which enables to obtain a reflection, albeit with a lower SNR.

1.1 Acoustic signal modeling

The classical system with only one ultrasonic element has an apparent limit as the focus is physically defined by its construction. Even with easily changeable lenses, the problem will only be partially alleviated, and the system will only be usable until the object for inspection is of a shape which has no correctly shaped lenses, and new lenses will then be needed to be manufactured. Alternatively, a flexible solution using the phased array [55]–[57] can be used along with many pre-calculations. Although flexible solutions have very desirable properties, the acoustic path model has increased complexity. On the other hand, if there is an easy reference point, such as a phased array with known positions of sensors, it is possible to 'simulate' lenses. This idea is known as the synthetic lensing method, and it works by creating virtual lenses which manipulate wave travel times like their real-world counterparts (Fig. 1.3).

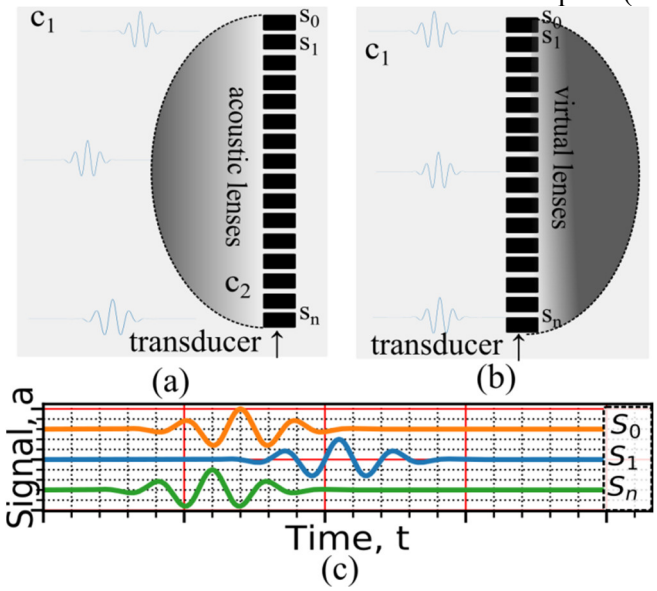

Figure 1.3 (a) phased array with real acoustic lenses; (b) phased array transducer without lenses using numerically calculated delays; (c) when using the same experiment environment, received echoes will be very similar [14], [15], [117]

From Fig 1.3 , the delay for an acoustic signal using real lenses can be written as [14], [15], [117]:

$$\begin{cases} S_0(t) = R_0(-(E_0 * c_1 + L_0 * c_2) + t) \\ S_1(t) = R_1(-(E_1 * c_1 + L_1 * c_2) + t) \\ S_n(t) = R_n(-(E_n * c_1 + L_n * c_2) + t) \end{cases} \quad (1.2)$$

where $S_n(t)$ is the recorded echo, R_n is the scatter response from the impact point, E is the distance between the scatterer and the lens surface, L is the acoustic distance from the surface of the lens to the transducer. The problem with physical lenses is that they are not universal, and, for another ROI, another set needs to be manufactured. This problem can be solved by numerically calculating the signal delay:

$$\begin{cases} S_0(t) = R_0(-(E_0 * c_1 + D_0) + t) \\ S_1(t) = R_1(-(E_1 * c_1 + D_1) + t) \\ S_n(t) = R_n(-(E_n * c_1 + D_n) + t) \end{cases}. \quad (1.3)$$

In Equation 1.3, E is the distance from the scatterer to the transducer element surface, and *D* is a vector that represents the reception delay. The values of this vector are a numerical approximation of real lenses, or, if the scatterer's position is known, *D* vector values show how much time is needed to be able to receive the scatterer's signal at the same time for all elements.

Because of the physical interference phenomena and the reflection from a wide-area/volume, the sensed frequency will be the superposition of the same signal, but with a different acoustic path, which, when the sensor receives the oscillating pressure wave, will be detected as a frequency-shifted signal. Even when ignoring a non-ideal transmitted signal, other signal changes will come from additional sources.

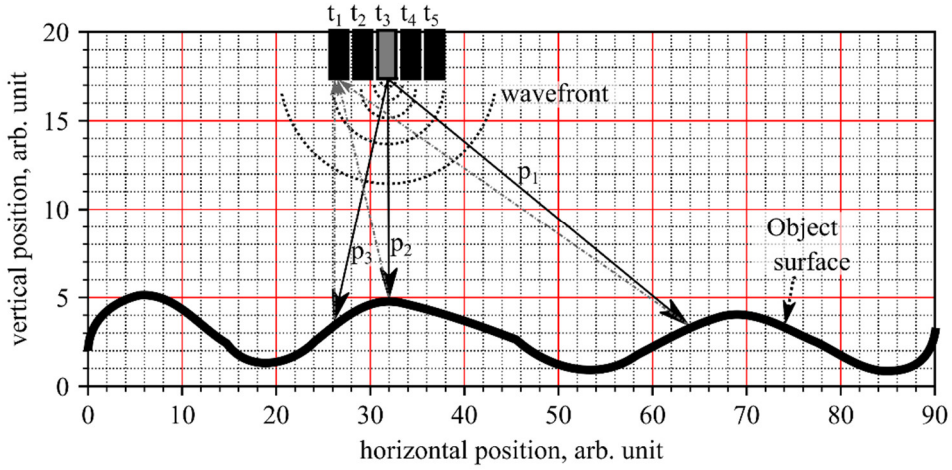

Figure 1.4 One of possible acoustic paths, t_3 is a transducer with a signal source, p_1,p_2,p_3 – possible acoustic paths to t_1 transducer. Acoustic pressure is interference of all possible paths

Figure 1.4 demonstrates an acoustic path which, after creating a wave from one element, can do reflection interference at a sensitive element. It will generate responses which are seen as shifted frequencies, and, mathematically, interference can be approximated with the following equation:

$$y(i) = \sum_{n} \left(S(i) * e^{ipt}\right) * e^{-\beta t} \tag{1.4}$$

where $y(i)$ is a recorded complex signal after reflecting from an object's surface, S(i) is a transmission signal for pulsed impulse, e^{ip} is the phase shift of a signal as p depends on the traveled distance and angle (for the acoustic model), and β is the damping factor of the signal in its environment. It is clear that we have dependence on distance, as well as the reflected angle and time in our model. t is the acoustic path time for the transducer receiving element n.

The main implication of Eq. 1.4 is the demonstration that, even for narrowband transmission, due to the phase shift from reflection of an uneven surface, a wider signal can be 'seen' on the transducer's ceramic element, thus the sensor's sensitivity for the signal is preferred to be as wide as possible.

1.2 Wave propagation in multiple media

Wave propagation in non-homogenous media and its inverse problem can be calculated semi-analytically from differential wave propagation equitation, and additional assumption-born approximation can be used. The solution becomes more complicated when there are media with different sound speeds, or mode conversion (pressure, longitudinal, shear wave or even generated surface waves), and it does not take into account the surface curvature.

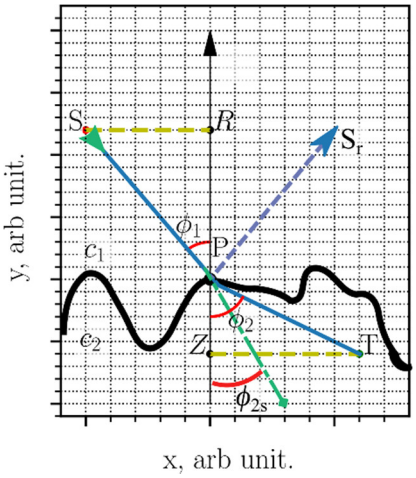

Figure 1.5 Snell's schematic example. From point *S*, via interference (the bold line) point P, and calculated point T. Snell's law for longitude can be expressed as $\sin(\varphi_1)/\sin(\varphi_2) = c_1/c_2$ (the SRP and ZPT triangles). Sr – reflected acoustic path from the surface, φ_{2s} – the created shear wave.

One of the methods to straightforwardly calculate the acoustic path is to use Snell's Law. This method is based on the idea that a pressure wave can be approximated as a ray, and the path which it takes is acoustically the shortest (Fig 1.7). Nevertheless, it has a drawback: Snell's law only works for emission if it is viewed as rays, but when non-regular geometry is involved, the definitive shortest path is not a trivial problem, and the calculations are not straightforward, although,

when discretizing the surface curve into segments and calculating individually, Snell's law can give satisfactory results [118].

The problem is more difficult with physical transducers. Firstly, as mentioned before, directivity is associated with a sensor. Secondly, in a real system, the associated spread is involved, and reflection can stem not from the angles which Snell's law directly solves, but originate from off-axis points where acoustic energy is still relatively strong.

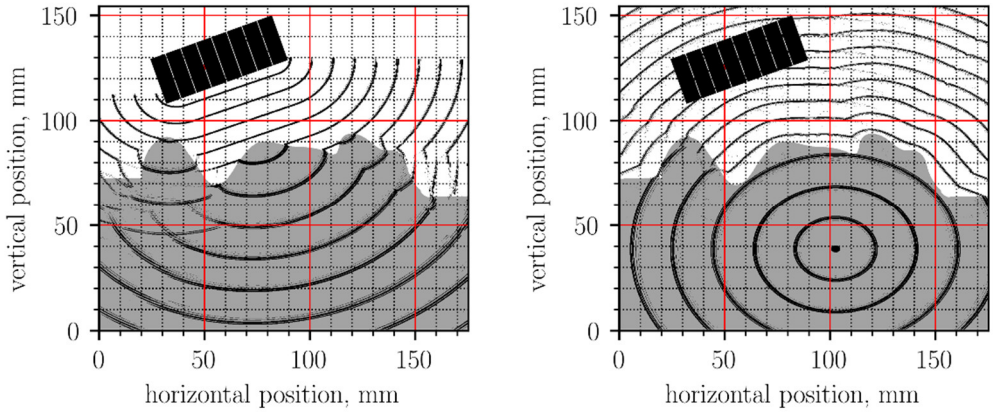

(a) (b)

Figure 1.6 Numerical example of wavefront propagation when using a plane wave (or a wide aperture transducer) displayed in time snapshots (only longitudinal/pressure waves are drawn): (a) – plane wave signal emission, (b) – acoustic propagation from the point size reflector. The white area is water environment c_1 = 1500 m/s, the darker area is the sample c_2=3000 m/s

As seen from Figure 1.6, the calculation of the acoustic path is not a straightforward problem. As for the numerical model, we can see that scattering and wave spread are manifested, which needs to be taken into account [119].

Figure 1.6 schematically demonstrates the advantages of the dynamic propagation model which is very hard to solve analytically because of the absence of wave evolution. On the other hand, when using a high frequency and small apertures, the wave propagation model's approximation will be more similar to the theoretical wave propagation model.

1.3 Focusing methods for phased arrays

Phased array focusing is a procedure which answers the following question: "how much does the signal need to be delayed for the transmission and reception to get meaningful results?" For the most straightforward solution, the delay must be the wave travel time to the chosen region and back. The process of delaying and illuminating the region of interest (ROI) is known as *beamforming*. If the medium is homogenous, there is no need to use iterative methods for acoustic path accounts, which holds for short distances. There has been much research conducted in the past [32], [120]–[122], and interest is still being paid to incremental research on new methodologies [43], [51], [60], [123]–[128]. In practical terms, all beamformers solve

the acoustic path approximation problem when not all the information is known. For reference, we can show one of the classic beamformer methodology equations [3], [15], [122] for receiving echo $r(t)$:

$$\mathrm{r}(t) = \sum_{i=1}^{N} A_{ri} \sum_{j=1}^{N} A_{xj} s_{i,j} \left(t - \tau_{ri} - \tau_{xj} + \frac{2R_{fp}(t)}{c} \right) \tag{1.5}$$

where A_{ri}, A_{xj} are shading functions for the reception and transmission [77], [129], [130], $s_{i,j}(t)$ is the transmission wavefront shape from the transducer element i to the transducer element j, notations r and x refer to the reception and transmission operations. $R_{fp}(t)$ is the distance from the origin point to the center of the desired focal point. τ_{ri} and τ_{xj} are the applied beamformer delays, and c is the speed of sound.

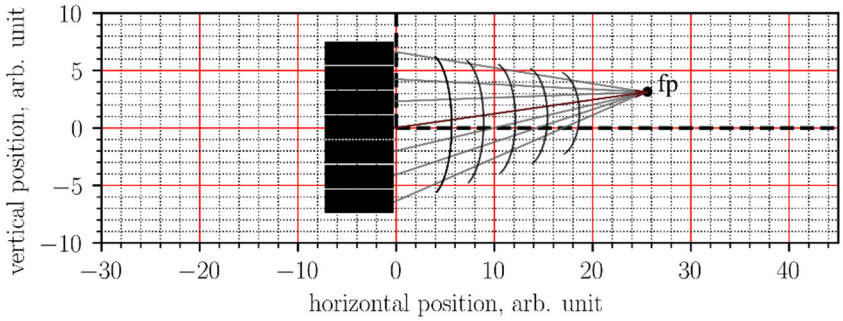

Figure 1.7 Basic geometry for beamforming

One of the calculations of the delay timing $\tau_n$to the chosen focal point can be done with the following equation [39], [122]:

$$\tau_n = \frac{\sqrt{(x_n - x_t)^2 + z_n} - Rfp}{c} \tag{1.6}$$

where (x_n, z_n) is the coordinate of the desired point, Rfp is the focus center distance from the point of origin (Fig. 1.9), and c is the speed of sound. This equation can be used for receiving and transmitting beamforming, as it can be used in physical transmission delays and for post-processing when all combinations of transmitting and receiving pairs are collected. This collection combination is known as the full matrix capture (FMC), while the method focusing on using all the possible signals is commonly known as the total focusing method (TFM).

For taking into account of the surface morphology, the focusing technique from the theoretical point of view does not change much. As long as it is possible to calculate the acoustic path, focusing can be done. Yet, the implementation of the focusing techniques involves more differences which have their advantages and drawbacks. Further in this paper, we shall conduct analysis of the methods candidates to investigate objects with complex geometry.

Surface adaptive ultrasound

Adaptive ultrasound (SAUL) [44], [131] is a feedback-controled autofocusing technique which demonstrates acceptable results in non-regular surface composite structures when only the fact of the presence of a defect is necessary. The main working principle of the algorithm of focusing is maximizing acoustic energy to the sample's surface. This is an active transmitting method and need equipment with configurable emission delay. It is an iterative method with the two following steps of operations in which the user has to:

1) Apply reception Δ_r and Δ_t delays individually to each element of phased array and record echoes.
2) Adjust delays Δ_r, Δ_t until all the reflections of the first echoes from the line in the B-scan (repeat from step 1 until there are no changes in timings). Alternatively, mathematically governing equations[131] are:

$$\begin{cases} \Delta_e^{(j+1)} = \frac{1}{2}\left[\max\left(t_i^j\right) - t_i^j\right] - \Delta_e^{(j)} \\ \Delta_e^{(j+1)} = \Delta_e^{(j+1)} - \min(\Delta_e^{(j+1)}) \end{cases} \tag{1.7}$$

where *(j+1)* is the new time step (iteration), whereas *j* is the previous iteration, Δ_e is the emission delay, t_i is the signal time-of-flight or the time of the first peak in the recorded data timings divided by two of the recorded roundtrip time. and $\Delta_e^{(j+1)}$ finally the emission signal from the alignment operation. As for the reception, it can be written in the following way:

$$\Delta_r^{(j+1)} = \max\left[\Delta_e^{(j+1)}\right] - \Delta_e^{(j+1)} \tag{1.8}$$

where Δ_r is the reception delay, and the second part for the equation is for intended aligning the delay with the wavefront. The graphical representation of Equations 1.7 and 1.8 is demonstrated in Figure 1.10.

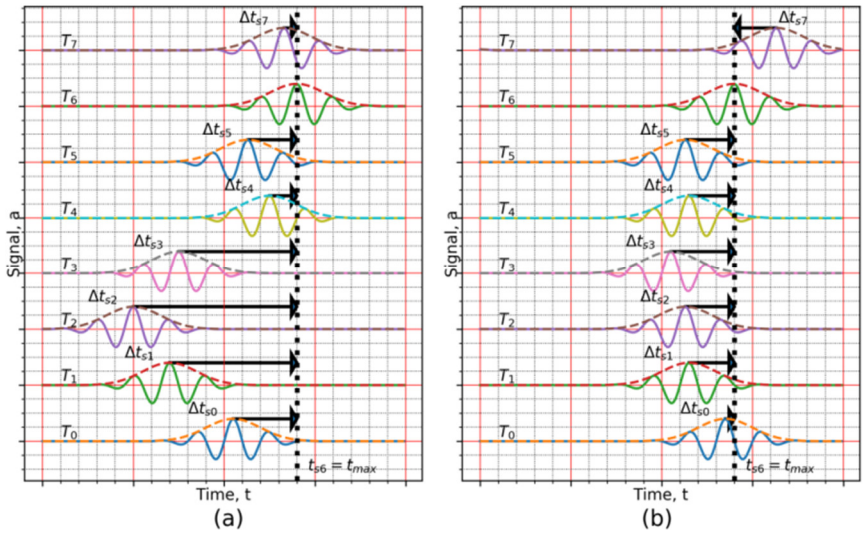

Figure 1.8 Two iterations of SAUL algorithm in A-scan representation: (a) first iteration – with delays 0, (b) second iteration (j+1 in equation) [1]

The absence of the acoustic model processing in this method is both its main advantage and its most significant drawback. Without the acoustic path, the assumption is that the transducer element's delay influence only works on the wavefront, which is delayed on the same element. This assumption is valid for objects of a convex surface; it is easy to prove that the shortest path for reflection is the only direct path under the transducer and that other specular reflections using plane-wave emissions will come later. However, this is not always the case for concave surfaces:

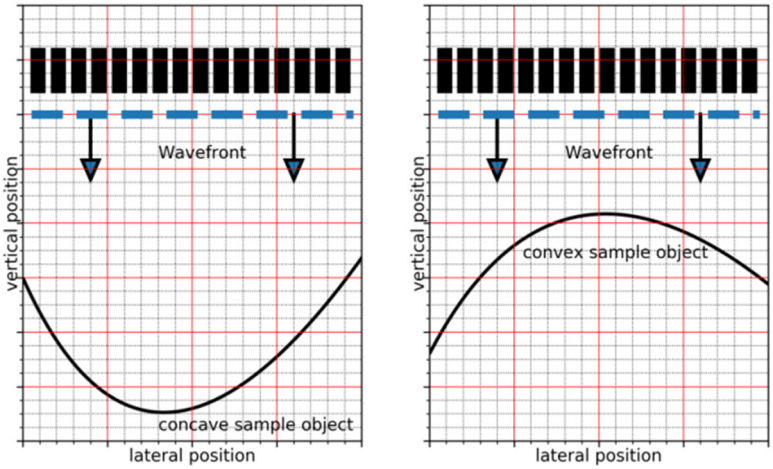

Figure 1.9 Example of reflection and changes in time [44], the black curve depicts the object's surface part

From Figure 1.11, we can note that the method will not have good convergence results when there is a concave surface, and signal reflection has no direct relationship with the transducer's number.

As for the conclusion, the SAUL method can be used for objects with a complex geometry, and, from radar communities, it is possible to reconstruct the surface morphology although the reconstruction is limited to the signal front (envelope) [131] and the specular reflection from the surface object. As for the volume reconstruction, it is necessary to create the complete wave propagation model in order to have the real position relationship.

Time reversal beamforming

The Time reversal (TR) imaging method is similar to SAUL as it is an active method which uses transducer transmission in order to achieve focusing, although, for TR, every active element must be able to emit modulated signals because for SAUL it is enough to use the harmonic frequency.

The reversal beamforming conceptual idea is the same as an optical mirror. Nevertheless, instead of generating a virtual image, the time-reversal mirror generates an image in reversed time. The theory is based on the wave invariance fact that emitted and reflected signals can be changed in places and there will be no physical difference in the wave propagation albeit the reflection is negative in time [50], [85], [117], [132], [133].

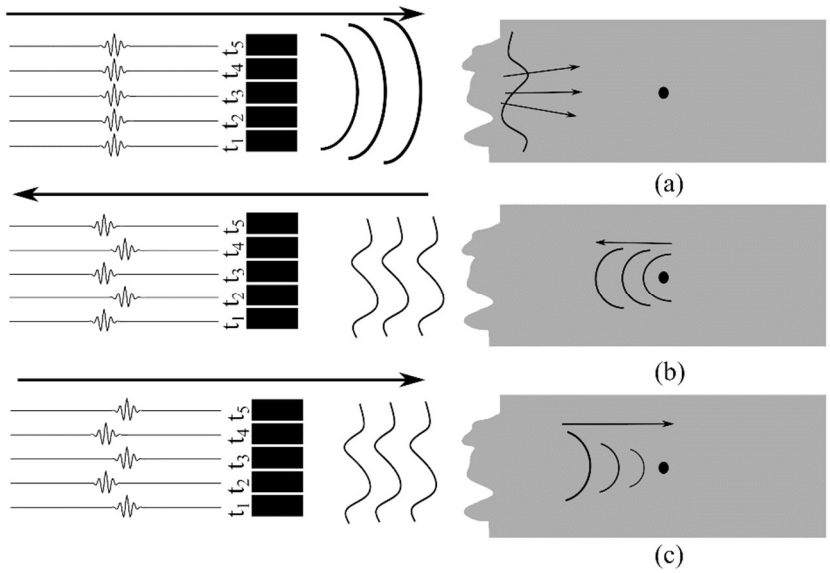

Figure 1.10 Time reversal mirror (TRM) focus operation requires three steps. Firstly, the infonifaction wave is emitted (a). Secondly, echoes are recorded in the forward time (b). Lastly, the time-reversal signal is sent back (c), which focuses energy back to the source [49]

Mathematically, the operation (Figure 1.11) is possible due to the time-invariant nature of wave propagation [49]:

$$\vec{\nabla}\left(\frac{\vec{\nabla}\mathrm{p}}{\rho}\right)-\frac{1}{\rho c^2}\delta^2\frac{\delta^2 p}{\delta t^2}=0 \tag{1.9}$$

where $\vec{\nabla}$ is the differential operator, *p(r,t)* is the pressure function, ρ is the material density, and *t* is time. The equation above is valid for a lossless medium but shows an important property of time reversal in physical sense, r is the travelled distance, and t is time. Because of the second-order time derivative, the equation has two solutions *p(r,t)* and *p(r,-t)*, although if the medium has have frequency-dependent attenuation, the time wave's inverse property is lost, and the time-reversal operator has no solutions. If there are solutions for time reversal in NDT, as various authors claim, there is an additional statistical step in the method for discerning the individual target [17], [47], [49], [50], [65], [85], [117], [132]–[134]

The TR focusing method's main advantage is the possibility to focus energy via a non-regular boundary without any additional knowledge, altiough main weakness of the TR method is if the reflector cannot be correlated or separated in multiple reflector presence methodcannot be used. An additional drawback of this method is the knowledge that the acoustic path must be solved with another method as the method works like a mirror, and energy is concentrated on the reflector. In conclusion, the TR method is not a usable for surface profile reconstruction , but, on the other hand, it can improve the detection quality in volume reflectors.

Total focusing method

The previous two above outlined methods have a drawback that they are active methodologies where acoustic signals need to be sent in order to achieve optimum performance. On the other hand, the methods where only post-processing is necessary are preferred. One of them is the total focusing method (TFM). It is the most 'classical' method for reconstructing an image from the received signals. As for the processing of signals, they are captured by using the full matrix capture (FMC) style: it uses all possible aperture combinations when there is only one active element. The TFM has multiple variations and usually serves in literature as a reference method. The method's idea is to create virtual lenses for the received signals.

The main advantage of this method, aside from its simplicity, is that it is not sensitive to noise, and it is possible to reconstruct images even with a negative SNR as long as there is accurate information on the acoustic path. Image reconstruction can be done by using the following formula [3], [39], [135]–[137] adapted from the classical method TFM:

$$I_{tfm}(x,y)=\sum_{t=0}^{N_t}\sum_{r=0}^{N_r}S_{t,r}(\Delta(t_x,t_y,r_x,r_y,x,y))*Ap(\dots) \tag{1.10}$$

where $S_{t,r}$ is the 3D storage matrix where *(t_x, t_y)* is the transmitter's position, *(r_x,r_y)* is the receiver's position and *(x,y)* is the ROI point, *t* is the index of the active transmitter element, *r* is the receiver's index, N_t is the active transmitter's aperture, N_r is the active receiver's aperture. $S_{t,r}$ is the recorded signal from *t* transmitter to *r* receiver; Ap(…) is the shading/apodization function. Equation 1.12 is one of the possible solutions of theoretical beamformer Equation 1.5.

The main component of the TFM beamformer is Δ – the acoustic path calculation equation. In a single media environment (in water only), it is virtually the total traveled distance between the transmitter, the ROI point, and the receiver. For the dual media (water is the coupling medium, and the solid object is a sample), the function is not straightforward because of the additional refraction, reflection and medium surface curvature boundary.

As mentioned above, the TFM method is straightforward, and, in practice, the acoustic path can be seen as a black box with any dependence. As there are no statistical requirements, it is the right candidate for creating an inspection methodology.

Delay and sum

TFM focusing is easily extended to the use of multiple transmit elements forming a wider aperture and increasing the transmit energy. However, when using the original mathematical expression, the emission is seen only as a single element emission. To extend the processing of a single element, all the aperture elements can be used (it is called the plane wave), which allows the emission wave to steer in various degrees (it is called synthetic steering).

The method which uses the plane wave for illumination is called Delay-And-Sum (DAS) as it is easy to note that it is an extension of TFM. As the main difference, the emission is not treated as a point source. Mathematically, the algorithm is written with only one summation term [5], [125], [137], [138]:

$$I_{das}(x,y) = \sum_{n=0}^{N} S\big(n, \delta(n,x,y)\big) * Ap(\dots) \tag{1.11}$$

where $I_{das}(x,y)$ is the pixel intensity at ROI *(x, y)*, n is the active aperture length, S(n,t) is the signal matrix, $\delta(n,x,y)$ is the delay function which cannot be assumed directly as usually it is a black-box model, and $Ap(\dots)$ is the element shading function.

$\delta(n,x,y)$ for DAS methodology in simple terms is the acoustic path calculation between the plane wave emission and the spherical reflection from ROI. In this equation, the *y*-axis is the vertical position aligned to the transducer's emission, and the *x*-axis is the horizontal line of the transducer.

As the apodization or shading function's primary purpose is to reduce sidelobes in the generated picture, in more general terms, it couples the signal sample with a physical quantity such as limiting the sample region (for example, removing back-wall reflection from data) or ignoring angles where the element has no sensitivity where TFM focusing is less critical because the emission of the signal is assumed from the infinitely small point, although, when the plane wave is used, it has to be taken into account. For primary cases, it can be a rectangular window with a 30-degree spread:

$$Ap(n,x,y) = \begin{cases} 1, \left|atan2(y, dx * n - x) - \dfrac{\pi}{2}\right| \leq \dfrac{\pi}{6} \\ 0, otherwise \end{cases} \tag{1.12}$$

where Ap (n, x, y) is 1 when the angle between the ROI point (x, y), and the receiving transducer element *(dx*n,0)* is less than 30 degrees (pi/6).

Even when the DAS method looks good on paper and has a non-quadratic execution, it is usually not enough to reconstruct data with sufficient reconstruction quality [126], [139], [140] where it would be easy to interpret the features. To increase the reconstruction quality, coherent compounding can be used, and the equation is shown below:

$$I_{das_{coherent}}(x,y) = \sum_{s=0}^{N_s}\sum_{n=0}^{N_a} S_s\big(\delta_s(n,x,y)\big) * Ap(\dots) \tag{1.13}$$

The additional term s is the shot number which usually means plane wave transmission when there is the steered angle (and a different position, if necessary), and the other δ_s is a function which depends on the shot's number. We can note that the DAS method is very similar to TFM, but, when using DAS, a very similar quality could be obtained by using fewer shots. Like TFM, DAS can reconstruct an image by using very low SNR [39], [140]. By original design, DAS was created for inspecting objects with planar geometries. However, with virtual sources, it is possible to increase the quality for inspection when using complex geometry [38], but most research has been done within a limited scope where multi-path reflection can be easily blocked, and the surface influence has a limited effect.

The method is denoted by excellent capacity to reconstruct object surfaces because of higher energy emission compared to a single element, although, by using this method for non-regular geometry, the acoustic path's solution becomes very complex due to multi-path, scattering and wave spread.

Delay Multiply and Sum beamformer

DMAS [33], [124]–[126], [141], [142] is a natural extension of the DAS methodology with the introduction of a multiplication step. From a high-level point of view, the algorithm changes from signal interference to an autocorrelative approach. By using the correlation, the method increases the contrast from highly correlated reflectors.

DMAS works similarly to the DAS method with an introduction of multiplication before the summing response (for the exact point of view, it can be viewed as a correlation function). The first step of the algorithm as in DAS is the acoustic path calculation, and then an additional step is performed:

$$I_{dmas}(x,y) = \sum_{i=1}^{M-1}\sum_{j=i+1}^{M} S_i\,(\delta_i(x,y) - \Delta_i)S_j(\delta_j(x,y) - \Delta_j) \tag{1.14}$$

where (x,y) is the ROI point is the transducer signals, and Δ_i, Δ_j is the acoustic delay's difference from (x,y) to i and j transducer; S_i, S_j are the recorded signals. In practice, the results of this beamformer will be the squared amplitude and the loss of dimensionality information.

Because of this lost signal sign information, envelope detection cannot be performed correctly. To overcome this problem, Matrone *et al*. [125] proposed an 'equivalent RF-signal' by using the 'signed' root approach:

$$\hat{s}_{ij}(t_i, t_j) = sign\left(S_i(t_i)S_j(t_j)\right) \cdot \sqrt{\left|S_i(t_i)S_j(t_j)\right|} \tag{1.15}$$

where t_i, t_j are the acoustic delays, sign is the mathematical sign function (it can be defined as $sign(x) = x/|x|$ or –1 for a negative number, 1 for a positive number and zero). Thus, the DMAS beamformer becomes:

$$\dot{I}_{dmas}(x, y) = \sum_{i=1}^{M-1} \sum_{j=i+1}^{M} \hat{s}_{ij}\left(\delta_i(x, y) - \Delta_i, \delta_j(x, y) - \Delta_j\right) \tag{1.16}$$

where the full equation now is rewritten by using Eq. 1.15 as the base operation from Eq 1.14. Mathematically, Eq. 1.16 beamformer calculates half autocorrelation [42], [125] and only takes the sign of raw samples before an operation. The first drawback of this method is the appearance of a second harmonic signal in an image that needs to be filtered, as it is essentially a heterodyne multiplication operation, but, for taking image results, the DC component is necessary. Thus, the main weakness is of this method is the sensitivity to the correlated signals reflections [140], wherein, for the inspection of objects with complex surfaces, there are a lot of correlated responses.

Minimum variance beamforming

There is one more approach for DAS beamforming which is called the Minimum variance (MV) beamforming. Even though it was first introduced by Capon in 1969 [143] for seismic data processing, it is a method that is still in use today as its main drawback is the long calculation times. The standard component of this method is the construction of a covariance matrix and calculation of its inverse, but the drawback is the enormous storage space requirements and the $O(n^3)$ computational cost (when using the most recent approach, it is possible to achieve $O(n^{2.529})$ computation complexity [144]). Nowadays, more effective approaches of beamforming are proposed, such as the use of predefined apodization functions, the use of a part of aperture, or the use of signal transformations [51], [52], [85], [129], [145]–[147]

The MV beamforming method works by dynamically changing the apodization vector's (in the literature, this may also be called the shading vector) weight, which in turn minimizes its variance (energy) while maintaining the unity gain of the total sum which can be written as follows:

$$Y_{MV}(k) = \sum_{i=1}^{N} x_i\,(t) w_i(t) = w(t)^H X(t) \tag{1.17}$$

where $w_i(t)$ is the MV weight (or, in on other words, the delay-and-sum beamformer apodization weights), $x_i(t)$ are the signal values at time *t* in *i* transducer, $w(t)^H$ is hermitian (complex conjugate) transformation of apodization weights and $X(t)$ are delayed signal samples (signal observations):

$$X(t) = \begin{bmatrix} x_1(t) \\ x_2(t) \\ \dots \\ x_N(t) \end{bmatrix} \tag{1.18}$$

Also:

$$w(t)^H = [w_1(t) \quad \dots \quad w_N(t)]^H \tag{1.19}$$

As for the calculation approach, it is an optimization problem that can be formulated as [147]:

$$\begin{aligned} &\min_{w(t)} w(t)^H R(t) w(t) \\ &subject\ to\ w(t)^H a = 1 \end{aligned} \tag{1.20}$$

where a is a steering vector or have value of ones if the signal is already focused on the ROI and R(t) is:

$$R(t) = E[X(t)X(t)^H] \tag{1.21}$$

where E is the Eigen decomposition function. $R(t)$ is a spatial covariance matrix, and there is proof that a direct solution for optimization formula exists:

$$w(t) = \frac{R(t)^{-1}a}{a^H R(t)^{-1}a} \tag{1.22}$$

However, in practice, the R(t) matrix is unavailable and is usually replaced by the sample covariance matrix:

$$\hat{R}(t) = \frac{1}{N}\sum_{n=1}^{N} x_i(n)x_i(n)^H \tag{1.23}$$

N is the number of the received samples which is then used as a real covariance matrix. It is best known as the Capon beamformer [143], [148]. In order to achieve faster computation speed, the Eigenvalues approach was proposed. The Eigenvalues approach utilizes the property that the input matrix can be divided into the signal subspace and the noise subspace [149] and can decompose the covariance matrix by Eigen components [53], [120], [149]–[151].

One of the visible drawbacks of this method is the slow calculation for finding the inverse of the covariance matrix, which limits the usage of the algorithm in real-time processing. Another approach was proposed to alleviate slow processing. One of these is an Eigen-space based solution exploiting the covariance matrix with virtual sources suggested by Moghimirad Zadeh *et al*. [152] or Bai *et al*. who in his paper combined the multiple apodization function with plane wave steering [153] by using multiple advanced beamformers to combine for a higher quality image: Eigenspace-Based Minimum Variance (EIBMV) [120], Multi-Apodization with Cross-correlation (MAX) and Null Subtraction Imaging (NSI) [153], [154], by using a multiple filter (Dual Apodization with cross-correlation) DAX methodology [155]. After using these approaches Chi Seo and Jesse T. Yensuggests tuning the relative parameters, such as adjusting the number by using Eigenvectors or Eigenvector values used as PCA

samples. The idea for real-time imaging arises from the possibility of calculating the estimation weight values offline.

In conclusion, minimum beamforming methods have an advantage in lateral resolution compared to the classical DAS. However, the main drawback of this method requires many calculations done for signal estimation; another drawback is the sensitivity to noise and the requirement for a robust acoustic path model in order to have meaningful variance information for focusing.

Wavenumber or frequency-based algorithms

Frequency domain-based methods are a direct evolution of the conventional heuristics-based methods; the main advantage is a much lower usage of computing resources, especially when using FFT transformation. They do not solve perfect inversions but do provide an approximation, which is good enough for practical purposes. The most common inversion implementations are the use of FFT-based transformation with which they share the wavenumber name because ISO 80000-8:2007 Standard suggests using the wavenumber name for transformation units [156].

Wavenumber methods were developed for the use in seismology by Stolt [157] in order to reduce the computing time. In practical implementations, the computational gain comes directly from the Fourier transformation efficiency [158]. In other words, wavenumber algorithms solve the spectrum mapping problem (or wavenumbers) in order to pinpoint scatterer coordinates.

In more recent times, these methods have been receiving much attention from the radar and sonar community as they are a natural augmentation of time-domain focusing techniques for the synthetic aperture radar and sonar (SAR/SAS). Because of active signal transmission, specialized methods have been created, each with its respective advantages and drawbacks, such as range-doppler (RDA) [59], [159] and Chirp scaling algorithms (CSA) [160] which is a natural evolution of RDA. The main reason for using these additional methods is to solve spectrum transformation more easily and to avoid full inversion processing.

The generic wavenumber methods, sometimes called omega-k [62], [161]–[163], often solve the direct inversion problem. The method works on the assumption that all scatters are infinite small (point sized), and the response pulse matches the Green function. The reflection from the source matches the ERM [133]. This means that reflection generates a spherical wave to all sides with the same amplitude and directions.

When using the ERM principle, the acoustic pressure is assumed that the wave travels in inhomogeneous media. For a less error-prone calculation, transducer sensors are placed on a regular shape (a line and a rectangle on a plane) [164]. The derivation of the method starts from writing the frequency domain expression of the scatterer pulse:

$$E(\omega, x, z) = \iint_{-\infty}^{+\infty} f(x, z) G(\omega, x - u, z) G(\omega, x - v, z) dx dz \tag{1.24}$$

where G is a two-dimensional Green formula, and *f (x, z)* is the scatter position function. Besides, ω is the angular frequency, $G(\omega, x, z)$ is the Green function.

When using an assumption about ideal point defects, we decompose the Green function by using Wyel identity [165]:

$$G(\omega, x, z) = \frac{-i}{4\pi}\int_{-\infty}^{+\infty}\frac{e^{ik_x x - i|z|\sqrt{k^2-k_x^2}}}{\sqrt{k^2-k_x^2}}dk_x \tag{1.25}$$

where k is $\frac{\omega}{c}$ a wavenumber. Thus the complete equation can be written as follows:

$$\begin{aligned} E(\omega, u, v) = \frac{-1}{(4\pi)^2}\iint_{-\infty}^{+\infty}\frac{e^{ik_u u + ik_v v}}{\sqrt{k^2-k_u^2}\sqrt{k^2-k_v^2}} \\ * \left[\iint_{-\infty}^{+\infty} f(x,z)e^{-j(k_u-k_v)x}\right. \\ \left. - i\left(\sqrt{k^2-k_u^2}\sqrt{k^2-k_v^2}\right)dxdz\right]dk_u dk_v \end{aligned} \tag{1.26}$$

It forms the spatial integral, and we can recognize 2D Fourier transformation from the scatter function. Let us call it F (k_x, k_z) and take the transformation from u and v, which can then be rewritten as:

$$E(\omega, k_u, k_v) = \frac{-F(k_u + k_v, \sqrt{k^2-k_u^2} + \sqrt{k^2-k_v^2})}{(4\pi)^2\sqrt{k^2-k_u^2}\sqrt{k^2-k_v^2}} \tag{1.27}$$

where the wavenumber with coordinates can be written as follows.

$$\begin{aligned} k_u &\approx k\sin\phi_1 \\ k_v &\approx k\sin\phi_2 \end{aligned} \tag{1.28}$$

The frequency-domain transformation yields a nonlinear coordinate system, as shown below.

$$\begin{aligned} k_x &= k_u + k_v \\ k_z &= \sqrt{k^2-k_u^2} + \sqrt{k^2-k_v^2} \end{aligned} \tag{1.29}$$

k_u, k_v and k map to k_x and k_z is known as Stolt mapping. This is basically a coordinate system transformation from the time domain to the frequency domain. However, there is one caveat: the forward model mapping has a one-to-many transformation (or, in other words, the physical position can be expressed by to two different variables in equation 1.29 coordinates space), and Stolt mapping is ill-determined and needs to be corrected by holding one of the parameters constant. When we hold k_u as a constant, as suggested by Hunter *et al*., [40], [166], it yields the following expression:

$$F(k_x, k_z|k_u) = -(4\pi)^2 S^{-1}\left\{\sqrt{k^2-k_u^2}\sqrt{k^2-k_v^2}\right\} \tag{1.30}$$

where:

$$k_v = k_x - k_u$$

$$k = \pm \frac{\sqrt{k_z^4 + 2(k_u^2 + (k_x - k_u)^2)k_z^2 + k_u^4 + (k_x - k_u)^4 - 2k_u^2(k_x - k_u)^2}}{2k_z} \quad (1.31)$$

is an inverse Stolt mapping with k_u constant parameter and $S^{-1}\{\ \}$ is its operator. This model works by ignoring the angles between the transmitter, the receiver and the scatter. It is not a big limitation for the scatter, which is far away, and the angles that influence it can be ignored, but, for short distances, apodization/shading is required to correctly interpret the results, which can be a problem.

The mapping can be improved with an additional weighting vector, which penalizes the received signal for large angles [139], [162], [167]. Calculating the vector values is done by assuming that every scatter point in the image can be modeled by taking its point spread function (PSF) and noise convolution [168], which obviously works with point scatters but will calculate the wrong results when the reflection is from linear boundaries.

The other class of the usage of wavenumber algorithms which are currently used generates state-of-the-art beamformers for PWI. However, the quality when using the maximum possible information (by coherent compounding) will give the same quality as when using DAS, although it would take a much shorter time, and, as mentioned above, the model works by ignoring the angles. Thus, the shading function is more critical. Additional weakness of this method is frequency transformation whose environment with multiple reflections will require an additional filter to remove unrelated signals. Because of the point source assumption, it is much harder to interpret results from the surface reflection; another drawback is a tough-to-create coordinate transform when the irregular boundary line is involved, which makes it is hard to use for processing the signal with complex geometry objects.

Super-resolution methods: Multiple signal classification (MUSIC)

Multiple signal classification (MUSIC) [63], [169] is a method initially invented to estimate the direction of arrival in signal processing. Generally, this method uses Eigen decomposition into signal subspace and noise subspace, and, as we know, these subspaces are orthonormal.

The MUSIC method can perform super-resolution focusing and can recognize defects or scatters with a size smaller than the diffraction limit for ultrasound applications. Of course, this comes with the usual drawbacks: noise must be kept as minimal as possible; if there are multiple targets, then they cannot exhibit correlation; noise must not have any correlation, and the scatter size is infinitely small (point-like), phased array elements should be put in line with the half wavelength pitch.

First, this method creates the following reflector model:

$$S_{source}(t) = a_{amp}(t) * e^{i(f(t)+\phi(t))} \quad (1.32)$$

where the signal is divided into two parts: a_{amp} amplitude and e phase in a complex form, ϕ is the signal phase from the scatterer, and t is the signal travel time.

The signal in the equation below will be sensed in the following form when it is directly before the receiver for a phased array with the first element as the reference. The signal that is received will be written in the following form [169], [170]:

$$S_k(t)e^{\frac{-i2\pi d_{p*}(p-1)*\sin\phi_k}{\lambda}} \tag{1.33}$$

where d_p is the spacing between transducer element p and p-1 element, ϕ_k is the phase offset from k source, λ is the wavelength. For signal sensing, we can write the following equation:

$$J_p(t) = \sum_k^F S_k(t)e^{\frac{-i2\pi d_p(p)\sin\phi_k}{\lambda}} + n_{p(t)} \tag{1.34}$$

The new n_p variable is a noise function, although for MUSIC to work correctly, only the Gaussian noise is preferred. Now, we can write a matrix representation of the signal:

$$J(t) = AS_{source}(t) + N(t) \tag{1.35}$$

where N is the noise matrix received by all the elements, A is a 'steering' vector, and J(t) matrix is represented as follows:

$$J(t) = [J_0(t) \quad J_1(t) \quad J_2(t) \quad \dots \quad J_n(t)]^T \tag{1.36}$$

Similarly, we can write the signal source matrix as:

$$S(t) = [S_0(t) \quad S_1(t) \quad S_2(t) \quad \dots \quad S_n(t)]^T \tag{1.37}$$

as well as the steering matrix [171] whose representation is:

$$A = [\,\beta(\phi_1) \quad \beta(\phi_2) \quad \beta(\phi_3) \quad \dots \quad \beta(\phi_n)] \tag{1.38}$$

This matrix forms the signal subspace, and its elements are defined as follows:

$$\beta(\phi_k) = [_1 \quad e^{\frac{-i2\pi d_0(p)\sin\phi_k}{\lambda}} \quad e^{\frac{-i2\pi d_1(p)\sin\phi_k}{\lambda}}] \tag{1.39}$$

And, lastly, the noise matrix is formed:

$$N = [\,n_1(t) \quad n_2(t) \quad n_3(t) \quad \dots \quad n_n(t)] \tag{1.40}$$

The MUSIC algorithm calculates the angle estimation by performing Eigen decomposition received signal into signal and noise subspaces as these subspaces are orthonormal. For the inspection of objects with complex geometry, the method for surface reconstruction in the original sense cannot be used because of strong point scatter requirements. For signal detection, it can still be used, albeit it calculates the angle of arrival and cannot be used directly, but, as an advantage, it can do super-resolution reconstruction.

Overview of focusing methods

Table 1.1 Comparison of methods

Classical	Modern
• Limited by diffraction. • Uses sample data directly, and noise has a limited impact.	• Not limited by diffraction. • Works in the frequency domain. • Noise has an impact on results.

• Intuitive math (for example, knowing the acoustic path is possible to get meaningful results). • Usually works in the time domain.	• Defects are usually point-sized sources. • There are limits to what can be processed. • Uses second-order statistics.

It can be noted that the primary difference between the terms 'classical' and 'modern' is the method's sensitivity to noise (or, in more scientific terms, if a method was derived by using the Green function [172] or Born approximation [78], [173], [174]). In an ideal environment, the statistical math-based methods outperform the classical methods, and calculations take a much shorter time (for example, when using FFT transformation-based algorithms).

Table 1.2 Selected methods for review table

Chosen for detailed review methods with group example	
• Electronic synthetic focusing (SAFT) • TFM [39] • DAS [138] • Delay, multiply and sum (DMAS) [124], [125], although it is a time-domain algorithm, for faster calculations can be computed by using the methodology of wavenumber algorithms • Double stage DMAS[127] • SAUL (surface adaptive ultrasound) [44]	• Wavenumber algorithms [40], [59], [164], such as frequency domain TFM versions [40], are also known as Stolt-k migration [62], [157], [161], [162], [167] • Multiple signal classification [41], [175] • Time reversal [41], [41], [48], [148] • Minimal variance beamforming [51]–[53], [120]

In Table 1.2, electronic synthetic focusing is a group of methods that performs the lensing operation on transmitting and receiving.

1.4 Method adaptation for surface reconstruction and inspection

Surface reconstruction can be avoided only if the fact about the presence of a defect is necessary, and only if a focusing adaptation can be performed, for example, by using the autofocusing property of the SAUL method.

However, when it becomes necessary to identify the positions of scatterers, surface morphology information must be known:

- For known geometry where the computer-aided design (CAD) model is available, the problem is attempting to match the received signals from geometry by using a computer model, such as FEM, or focusing calculated by back projection.

- Laser scanning can be used to make an accurate object bounding shape, but the object must be reflective to a laser, which is not always possible
- X-ray tomography can be used for creating a 3D model of an object and using ultrasound testing as a complementary tool.

The main problem with the methods mentioned above is the necessity to hold accurate spatial coordinates in a computer system between various processing stages. Even if the CAD model, which holds the digital representation coordinates of the model, is not in the physical world position, the mismatch of the acquired coordinates will have a huge effect in the determination of the position. The reviewed methods which directly deal with this problem use one or more additional assumptions [44], [131], [146], [176]–[179].

- Simple geometric formulas can approximate the object geometry, and applying Snell's law is relatively straightforward.
- An object's surface is usually convex, and all reflection goes out of objects. In other words, the curvature plane normal vectors do not intersect.
- If the object has concave segments, it will produce correct results as long as the curve is relatively small and the reflected rays intersect behind the transducer.
- There are no multiple path reflections.

These assumptions arise mainly in order to reduce computation time. For example, taking into account the multi-path reflection using ray tracing for the acoustic path calculations will take much time. The concave assumption ignores uncertainties and phantom data in the final result because, otherwise, a differential wave equation model will need to be solved. This process can use many computing resources to improve the results, which will not always be much better than in the case if the uncertainties are simply ignored.

What concerns the reconstruction methodology, we see that there is a compound problem to solve: 1) the acoustic path calculation in the measurement environment; 2) methods for surface morphology calculation – as it is seen – because of correlated reflection, there is an additional implication regarding the use of FFT or statistics-based methods; 3) the acoustic path in an object takes into account the surface curvature which essentially can be assumed as a black box. Thus, with regard to the full methodology, the time domain methods have the advantage of treatment of the acoustic path as the black box and immunity for noise.

1.5 Noise and its filters

One of the fundamental problems with real data is the presence of noise. The noise problem in the inspection can be found in the received raw data, and the noise is often still present after running various reconstruction methods. The noise in a reconstructed image is called the speckle noise, which is a noise artefact generated in the algorithm execution, the measurement system noise, or the sample structural noise. It can be both additive and multiplicative, and various methods are used to reduce its effect. Without any specifics, speckle noise can be written as:

$$f = uN \tag{1.41}$$

where f is the final value of a pixel or a texel, the data is in three dimensions, u is the signal and N is the independent noise term. The term is usually presented with the matrix and is time-dependent. Various algorithms have been developed to filter the image from the speckle noise.

The simplest way to remove speckle noise is to use a median image processing kernel, a Gaussian blur filter, or an FFT-based transformation to remove high-frequency noise [180]. Another proposal for a speckle filter was made by Perona Malik [181] who proposed a simple method for image filtering based on the energy diffusion principle. The diffusion principle has the advantage of holding image edges more accurately than Gaussian smoothing.

There are also other methods, such as:

- The Laplacian pyramid-based nonlinear diffusion method [182]. In theory, this filter has both decomposition and interpolation styles and has multiple stages, which first transform the image into the Laplacian pyramid domain [183], [184] and then remove high frequencies. After that, the method uses a Perona Malik filter to preserve the edges and then reconstructs back to the original image.
- Speckle Reducing Anisotropic Diffusion (SRAD) [185].
- Bayesian non-local means filter (OBNLM) [186].
- Other algorithms for de-speckling [187]–[191].

Yet, the reviewed algorithms can improve the image quality without *a priori* information about the environment or with the ability to physically increase the SNR of inspection in the noise reduction limits.

There is additional noise introduced in the system from the physical world that affects the measuring system. These uncertainties can be roughly divided into three phenomena: jitter [192], gain nonlinearity (although, in the working bandwidth, the gain nonlinearity is very low or even non-existent) [116], [193], and conversion-sampling errors [194]–[196] when the knowledge of the physical environment is not fully available. In terms of reviews, errors can be divided into two groups: the physical environment errors and digital errors.

In general, visible distortions are reconstruction errors from the ADC signal. Even if the electronics produces the correct signal shape, final sample values are produced in ADC. In the ideal case, inaccuracies can be approximated as a Gaussian process with a particular deviation.

A particularly prominent type of digital error is the floating-point numbers format error [197]. However, we should note that floating-point operations in computers are not commutative, and their order matters (multiplication, subtraction, sum), although the simplest solution is to use more comprehensive floating-point number formats or to rewrite the operation in order to improve accuracy [198].

Another source of digital errors with a low impact is that not all numbers, such as 0.1, can be expressed in binary formats. As a result, there are rounding rules, which the author, by default, has left unchanged.

The errors can be summarized in the following table:

Table 1.3 Errors summary table

Equipment part	Impact	Explanation
Transducer manufacturing process	High	Needs to be calibrated separately
Pulser electronics	High	From an incorrect central frequency to generate a voltage that is too low for correct vibrations
ADC	Low	The intristic 1–2 sample variation delay and assuming that the voltage-to-value conversion is in the have 1LSB error limit

The practical implication of errors is the state of the transducer and the correctly working pulser. ADC also has a huge impact, but it is usually calibrated by the manufacturer.

1.6 Numerical modeling

Because of the large amount of time required for finite element simulation, other methods were also invented. One notable method is a pencil used in CIVA [83], [101]. It is a relatively simple method for homogeneous media, and it works by treating the sound source as a point source and an emitting plane wave.

For plane-wave modeling methods, Foldy [199] and Lax [200] methods were proposed, although the proposal was made a long time ago. Recently, more useful algorithms have appeared [95], [96], [201]–[204].

The main advantage of this method is that simulating a wave field does not require the solving of partial differential equations. Depending on how the method is used, different shortcomings will be manifested – for example, for KZK-based methods [93], [95], [97], [205], simulation is only possible for far fields.

The transducer model is a key component in a high accuracy model [71], [206]–[208]. However, it requires the usage of a large number of resources and a known accurate physical model. Detailed manufacturer information is kept a trade secret and is not shared publicly. On the transducer datasheet, only the element delay function is calculated, and the sensitivity is calibrated in a controlled environment. For this thesis, only pressure modeling was done in order to approximate the ideal transducer.

As it was mentioned above, some of the effects can be mitigated by introducing virtual elements [28], [130]. Suppressing the transducer-limiting effects is called apodization or shading [77].

The near field involves the case of the moment when the transducer sends a signal, and, a short time after, it is blinded by itself, but research has been conducted with attempts to reduce this effect [89].

It is necessary to produce methods calculating in the fastest possible way. For the methods developed by using General-Purpose computing on the Graphics Processing Unit (GPGPU) methodology, NVIDIA's CUDA system is currently being used [209]–[213].

1.7 Conclusions of the First Chapter and tasks of research

The analysis of methods for the inspection of objects with a complex surface morphology and volume reconstruction demonstrated that there are no straightforward algorithms to achieve reconstruction, as the currently available methods usually assume a single environment without explicit dual media reconstruction. Or, in the case of dual media, the reconstruction is limited by point sources reflections, and it ignores the geometry information. For the inspection of an object with the known CAD model, the algorithm can do offline calculation of the acoustic path. Yet, the use of FEM can impose enormous requirements on time and computing resources. Therefore, it is necessary to investigate faster methods for acoustic path calculation.

As for the reflected signal interpretation, each method has its advantages and weaknesses as the methods can be divided into two groups by their reflection approximation assumption. One type of methodologies is to assume that the reflector is of the point size, and that imaging can be calculated as the solution of inverse wave propagation. Its core advantage is the relatively fast calculation times and the possibility to interpret correctly the reflection information over the diffraction limit, but the noise needs to be Gaussian, and, for multiple reflectors (defects), there need to be no signal relations (i.e., no correlation).

The problem of the inspection of arbitrary objects is the complicated prediction of the acoustic path due to various effects, such as refraction, wave mode change and various interactions between them. Prediction is required when the position of the defects of the object needs to be known because with the knowledge of the object's boundary, it is possible to interpret the signal with confidence; another drawback with the arbitrary boundary is the hard-to-find direct acoustic propagation solution – thus, statistics-based algorithms are hard to design.

In this work, it is required that the developed method should work in the 2D space. It can be viewed as a limitation, but, in practice, it can be extended to the 3D environment straightforwardly, although there will still be some limitations involved. The conversion from 2D to 3D space algorithmically can be viewed as a more complex shading function. Although, complex spherical interactions for the acoustic path calculations should be noted, which suggests that it is not a trivial solution. Another view towards 3D reconstruction is to reconstruct defects from the 2D space and to interpolate the data.

Therefore, in order to develop a methodology for complex object inspection, the following tasks have to be solved:

- Create and investigate the method for the reconstruction of surface morphology for the 2D case.
- Create and investigate a method for volume reconstruction when the surface morphology information has been algorithmically obtained.

- Numerically verify the proposed methodology for surface morphology and volume reconstruction.
- Experimentally verify the proposed methodology for object inspection and its inner structure reconstruction.

2 DEVELOPED ALGORITHM: RECONSTRUCTION OF OBJECT SURFACE MORPHOLOGY

This chapter discusses the object surface geometry reconstruction problem, and how it can be solved. It can be avoided if the model of the surface is known *a priori*. However, even if the information about the object surface morphology is known, the matching coordinate system over the object outline with a known computer model can be a non-trivial task due to the misaligned angle or the changed object position, and the transducer will 'see' from a different angle, or even there will appear an error in the sound speed. In the worst-case scenario, the knowledge of the surface morphology coupled with wrong positioning will produce wrong results, or, in extreme cases, it will reconstruct only noise without any relevant information.

The surface can be reconstructed in various ways, such as the use of methods outlined in the literature review, but, currently, we shall focus on the reconstruction by using only a phased array in a rigid stand (or, in other words, in a stable position), with *a priori* knowledge of the sound speed in water. Although focusing can be done with multiple methods, such as PWI, TFM, or statistics-based methodology, but because the continuous surface has a correlated reflection response [60], [61], [149], [173], [214], the point reflection assumption (the main assumption for these methods) is false.

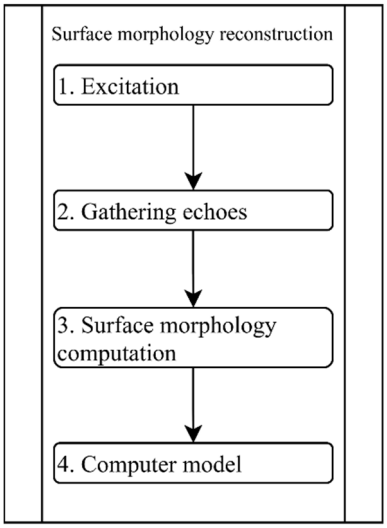

Figure 2.1 Flowchart of the steps of the proposed methodology

This chapter shall describe the methodology from signal emission to surface morphology reconstruction. It is the first part of the proposed methodology (a detailed overview of the steps is presented in Figure 2.1). Two different approaches are proposed. Firstly, we describe the one which is based on the time-domain

reconstruction. Then, in Subchapter 2.2, we describe the second one which is the author's developed analytic method with the limitation of planar segments.

Table 2.1 Surface reconstruction methodology steps when assuming work with raw data without any additional processing

Step No.	Step procedure	Short description
1.	Excitation	Excitation procedure PWI or FMC
2.	Gathering echoes	Delay alignment and if it necessary multiple shots combination
3.	Surface morphology computation	Filtering, detrending and back wall removal
4.	Computer model generation	Interpolation step from discrete points to the continuous model

Table 2.1 generalizes the necessary methodology steps for creating a computer model or a boundary zone between dissimilar environments (for example, water and plexiglass). It is required for volume inspection and the detection of defects.

2.1. Surface morphology reconstruction

Step 1. Excitation

The first step of the methodology is to generate an impulse for excitation [28], [77]. One of the most natural and practical methods is to generate a high-voltage spike pulse and to leave the transducer to resonate on its resonant frequency [25]. Even for a complex relationship, the pulse can be approximated with the sine function by using a Gaussian distribution window:

$$s(t) = \begin{cases} 0, t < \delta \text{ or } t > \delta \\ \sin(t) * g(t - \delta) \end{cases} \tag{2.1}$$

where t is time, and δ is the signal width. In the modeling part, it is used to describe the time where the energy of vibrations can be picked up (which is not interpreted as noise). $g(x)$ is a Gaussian distribution function where deviation values depend on the transducer's physical conditions and the center frequency. The Gaussian distribution can be written as:

$$g(t) = \frac{1}{\sigma\sqrt{2\pi}} e^{-\frac{(t-\mu)^2}{2\sigma^2}} \tag{2.2}$$

where t is the time position, μ is the distribution median (the highest point) position in signal modelling (for simplicity, we can leave it as 0 (the coordinate start)), and σ is the standard deviation width for the peak which naturally depends on the frequency. The exact values of distribution in real environments need to be numerically or experimentally calculated.

Phased arrays can excite emission pulses in various ways when there is a possibility to control individual elements. Usually, due to limitation, only spike pulse excitation and pulse delay methodologies are used. The two primary methodologies are to use one element emission or the plane wave; they have two main differences:

for one element, the beam pattern in the calculations can be assumed as circular emission from the point source (Fig. 2.2a), and, for the plane wave, the shape is a cone, albeit the energy is much higher (Fig. 2.2b).

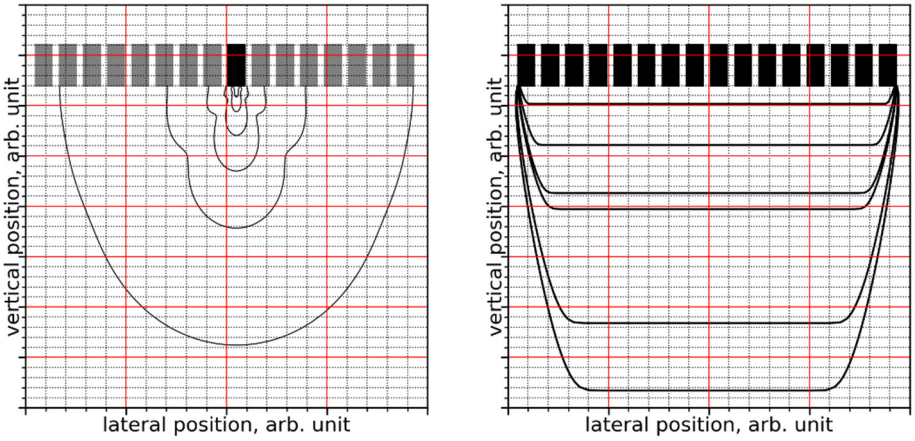

(a) (b)

Figure 2.2 Single element and plane wave beam patterns (darker elements are the sources), the lines are pressure isolines (shown at arbitrary time positions), (a) is a single element; (b) is a plane wave without steering

In the mathematical sense, when using the FMC excitation mode, the formula for the acoustic path is straightforward and less prone to errors. On the other hand, when using the plane-wave, the assumption of the point-like source is lost, but practically it can be compensated by using coherent compounding due to the fact that the beam has a conic cut [215], and, with the requirement of the apodization function, as for quick acoustic pressure approximation, a *sinc* based function can be used (Fig 2.2a):

$$\mathrm{sinc(x)} = \begin{cases} 1, x = 0 \\ \dfrac{\sin x}{x}, otherwise \end{cases} \quad (2.3)$$

where x is the angular component.

Even with analytic representation and when doing a lot of approximation, it is not trivial to calculate a single transducer's emission pattern; the problem is more complex for a phased array where there are multiple transmitting elements, for example, if we take a phased array with 128 elements and emit various configurations of sound waves (Table 2.2).

Table 2.2 Model parameters

Parameter	Value
Sound speed	1480 m/s

Absorption parameters α, coef	α=0.75 [dB/(MHz^y cm)], coef=1.75
Element sizes	0.6mm, 0.75mm, 1.0mm
Apertures to investigate	One element (single element aperture) and PWI
Center frequencies	2.25MHz, 5MHz, 10MHz

This investigation visually demonstrates the frequency dependence of the emitted energy that is visible from the absorption parameters and various beam patterns for the outlined methods:

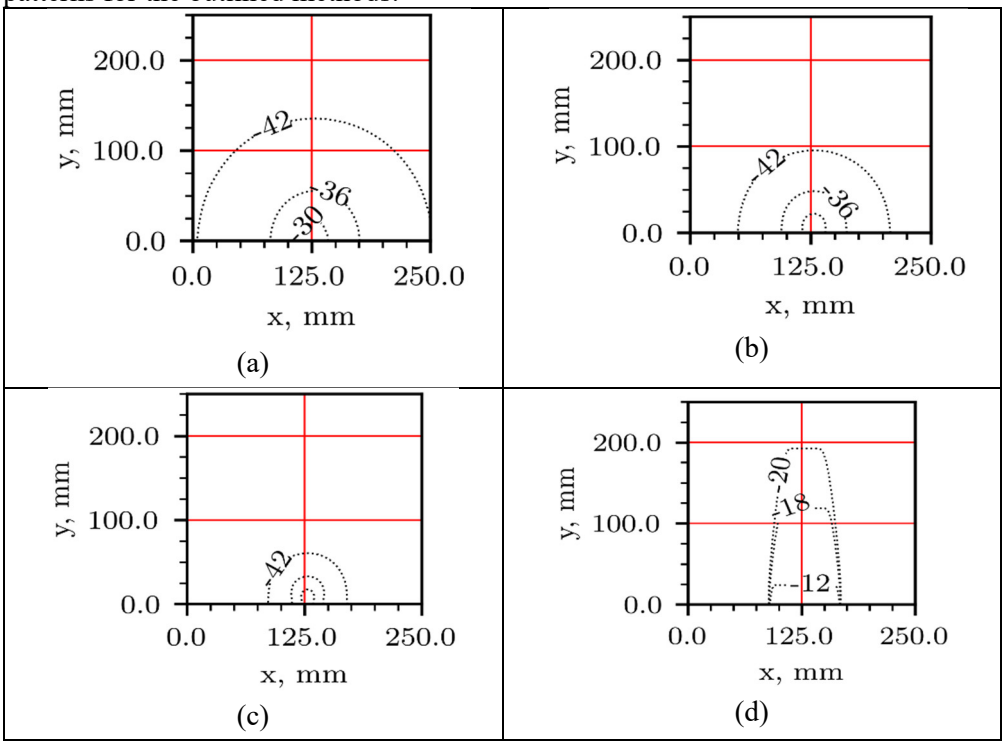

Figure 2.3 Beam patterns numerical models developed when using Table 2.2 parameters (the unit in isolines is dB, the reference number is emission pressure): (a) – 2.25 MHz single element, (b) – 5.0 MHz single element, (c) – 10 MHz single element, (d) – 10 MHz 128 element aperture plane wave

As we see from the numerical calculation of beam patterns (Fig. 2.3), we can notice the following observations regarding the emission pulse:

- When using the plane wave (Fig. 2.3d), the beam pattern starts to become egg-shaped (a cut cone), or it produces side lobes in the image if the effects are not mitigated, this is one of the reasons why coherent compounding is necessary;
- When using a single element (Fig. 2.3a–c), the near-circular pattern of pressure can be noticed as it is created by straightforward mathematical approximation operations.

- Moreover, from the numerical experiment, we can determine that there is a trade-off between the object detection sharpness (the wavelength size/frequency) and the damping effect. As it is evident, the lower is the frequency, the better is the emission pulse (Fig. 2.3a vs. Fig. 2.3c).

The main reason to use unfocused (the case of FMC) is the ability to universally post-process data after its acquisition. Although, it is still possible to post process and excited signals with different shapes or modulation – but with a much increased computing cost due to the losing point source emitter assumption.

Step 2 Gathering echoes and data preparation step

A short reminder of the representation data of phased array results (B-scan) is a matrix form, as shown in Eq. 2.3 when using the column-major order [216], as the practical implementation is always to use the 2D matrix format for one shot and to stack it when there are signals from multiple positions and for the physical position information use lookup table:

$$S_n(r,t) = \begin{bmatrix} S_{n,0,0} & S_{n,1,0} & \dots & S_{n,r,0} \\ S_{n,0,1} & S_{n,1,1} & \dots & S_{n,r,1} \\ \dots & \dots & \dots & \dots \\ S_{n,0,t} & S_{n,1,t} & \dots & S_{n,r,t} \end{bmatrix} \tag{2.4}$$

where S_n is the received signal sample matrix, n is the receiver's number, and t is the discrete-time in samples (it is the B-scan). The following data forms a 3D matrix when using multiple shots (or iterations). If we possess additional memory, the less error prone method is to pad the matrix with zeros (thus aligning time offsets):

$$\hat{S}_n(r,t) = \begin{bmatrix} \delta(r,0) & \delta(r,0) & \dots & \delta(r,0) \\ \delta(r,1) & \delta(r,0) & \dots & \delta(r,0) \\ \dots & \dots & \dots & \dots \\ \delta(r,t) & \delta(r,0) & \dots & \delta(r,0) \\ S_{n,0,0} & S_{n,1,0} & \dots & S_{n,2,0} \\ S_{n,0,1} & S_{n,1,1} & \dots & S_{n,2,1} \\ \dots & \dots & \dots & \dots \\ S_{n,0,t} & S_{n,1,t} & \dots & S_{n,R_n,t} \end{bmatrix}, where\ \delta_i = 0 \tag{2.5}$$

where δ_i is the zero values (or empty samples) which are shown in this form for convenience. The question remains as to how much delay needs to be applied. In practice, it needs to cover the signal which we are interested in. In other words, we can imagine that the receiver is already turned on, after signal emission, but the recorded interval does not start from the first sample.

The common DSP signal pre-processing tasks cannot be avoided in real-world equipment. Even if there is no calibration data, and the equalization step is not done, one of the first visible distortions is the linear trend (a systematic data increase or decrease), and the bias value (the constant input value which can be either negative or positive).

On the other hand, the extension for the matrix transducer when using the same matrix is only the physical position information table extension, although the algorithms for focusing still need to be changed.

Step 3. Object surface morphology CAD model

Even when having the correct CAD data, it is still necessary to match the known CAD template physical parameters (relative position and angle) with the data of signals, which can be a tedious task with a system that has limited calibration information. In order to make the method more universal, it is preferable to use the same transducer for the inspection and for the morphology reconstruction.

As for the sensor energy information from the object reflection mathematically can be approximated as the cosine Lambert law [217]–[219], which in the simplified case depends solely on the angle, thus ignoring other surface properties, as, from the pure mathematical sense, the reflection is spherical to all sides. It can be written as the cosine rule:

$$I = I_0 \cos(\alpha)\, e^{-x\beta} \tag{2.6}$$

where I_0 is the initial energy, α is the angle between the sensor and the normal of the reflecting surface, β is the damping factor, and x is the distance.

The next problem is the transducer sensitivity, which depends on the reflected soundwave incident angle, and, for the initial approximation, it can be used as the sin function reflection rule:

$$I_r = I_{r0} \sin(\gamma)\, e^{-x_r\beta} \tag{2.7}$$

where I_{r0} is the initial reflected energy (the damping coefficient is the same as for the emission), and x_r is the reflected acoustic path, β is the damping coefficient which depends on the material, γ is the reflection angle between the sample surface and the transducer.

In order to make the math slightly more straightforward, while assuming that the acoustic path is 'short', the damping part can be dropped, and thus the emitted and reflected energy can be written as a single equation which depends on the angles:

$$I_t = I_0 \cos(\alpha) * \sin(\gamma) \tag{2.8}$$

I_t is the reflected energy without the damping part.

To simplify the formula, γ serves as the symmetric response assumption (the emission and reflection angles are same):

$$I_t = I_0 \sin^2(\alpha) \tag{2.9}$$

where I_t is the reflected energy, α is the angle difference between the transducer and the surface when the direct incident wave is calculated as 0 degrees.

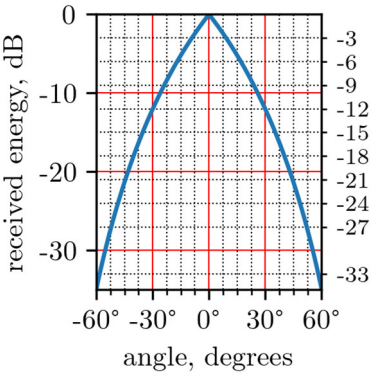

Figure 2.4 Reflected energy from a flat surface when transducer is rotated by $\boldsymbol{\alpha}$ degrees (Equation 2.9)

Equation (**2.9)** and its visual representation in Figure 2.4 shows of a physical limitation of the transducer element which listens to reflected echoes.

For focusing, GPGPU implementation based algorithms should be preferred. The main advantage of the graphics processor is that it has more computing power for the number crunching application. Another problem domain (3D graphics rendering) is that the reconstruction algorithms must have a good fit (see Appendix A1 algorithm).

As for the surface reconstruction problem when the sample object have an irregular profile shape it is visible the reconstruction problems with focusing limitation because of the different angles the interference from the acoustic path can have a low SNR, and the trivial method to get maximum value will not work (Fig 2.5 shows the regions with strong SNR in bold). Therefore, data collection for surface information needs to take the acoustic wave travel time and use the first echo data even with a much lower amplitude.

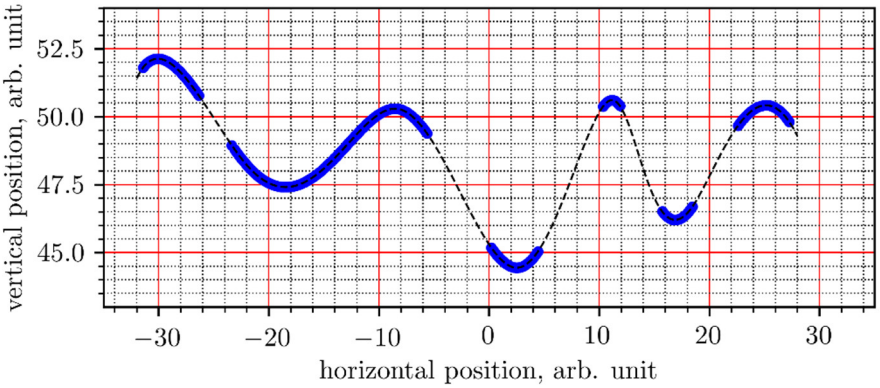

Figure 2.5 Example of surface reconstruction when using experimental data. Without numbers, blue lines are a reflection with high SNR, and dashed lines are the CAD model overlay

When focusing images are generated, the object boundaries reconstruction step can be started. As we have seen from the equation above (Eq. 2.9 and visual representation in Fig. 2.4), the object boundary line points have varying interference values and involve missing data (for example, the incident wave is at a critical angle). With wide energy differences, multiple points must be taken for boundary point decision. Mathematically, $(x, y)_k$ -point can be written as:

$$< (x,y)_k \,|k \in P > \tag{2.10}$$

where k is a candidate point in area P which is around the peak. However, in order to generate point set P, it is necessary to take into account wide interference values in the focusing step (see Fig 2.5 as only the strongly reflected part can be taken for true values), as, more practically, the operator-limited region D should be provided (for the vertical position interval, see Fig 5.7 for examples of experimental results); mathematically, it can be written in the following form:

$$P_x = arg \max_{x \in D}(x,y)_k \tag{2.11}$$

where P_x is the peak value coordinates in the operator's selected region D for the boundary point. As for the reflection from the surface, as an advantage, it can be noted that there is no wave signal inversion seen on the receiver's side.

After collecting the points and taking the peak value coordinates along the scanning axis (for example, y coordinates), the computer model of the surface can be created. First, a continuous model is necessary for accurate processing.

The model can be created by using b-spline interpolation.

$$Y_i(t) = a_i + b_i t + c_i t^2 + d_i t^3, t \in [0;1] \tag{2.12}$$

$Y_i(t)$ is a segment position equation where a, b, c and d are coefficients that need to be calculated [220]. It is a common problem, and the solution is not given (for example, the spline function in the Mathworks [221] software or *scipy.interpolate.BSpline*[1] using the Scipy Python package [222]). Yet, there are various interpolation methods for such an issue, e.g., by using a different order of splines or Non-Uniform Rational B-Spline (NURBS) curves, but accounting for the practical limitations of the UT inspections system, when the b-spline is sufficiently simple to implement, and errors from the system have a much higher impact than the interpolation function.

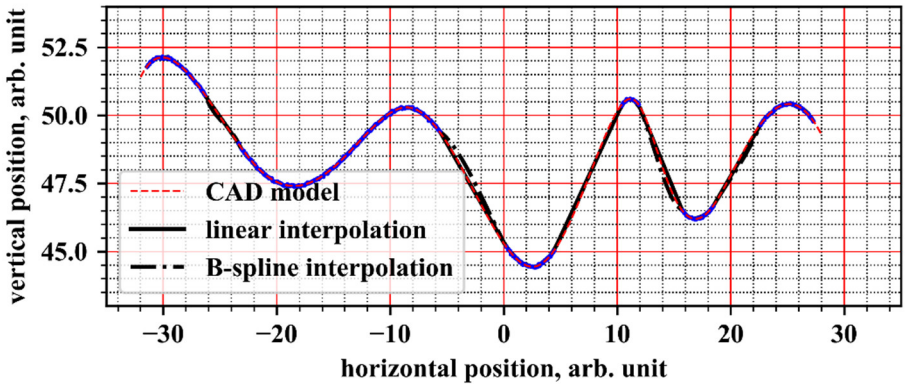

Figure 2.6 Example of CAD model interpolation; the values for interpolation have added random noise to make the impact of errors more visible

The calculated surface CAD model (Figure 2.6) serving for practical purposes has to be checked by the operator, and the interpolation method has to be tested, as, in practical application, B-spline interpolation can be used and yield good results, but, for example, in Figure 2.6 with noisy points, linear interpolation visually yields better results.

Step 4. Computer model generation

The environmental illumination and surface reconstruction are a critical part of the proposed methodology. The bigger impact of the mismatch factor is due to the non-regular boundary line (surface) than due to the plane surface. The impact of the accuracy of the speed of sound and the transducer model for the surface model visually has a relatively little impact as it can be viewed as a coordinate transformation operator. Although, for the accurate physical representation, the reflection impulse and position in the sample need to match.

[1] https://docs.scipy.org/doc/scipy/reference/generated/scipy.interpolate.BSpline.html

The practical part of the computer model is a format which can be used for object inspection. One of its practical representations is a list of points with physical coordinates, as one of the weaknesses of this list is the calculation how many points need to be saved in order to have accurate profile representation even when having the interpolated model is not very practical (if considering the associated computing time) for performing calculations. Another point of the computer model is that it can be interchanged with the original CAD model or employed while using other means, such as a laser.

2.2. Planar segment reconstruction

It is possible to use algebraic methods for complex geometry reconstruction if it can be approximated by linear segments which are visible on an unprocessed B-scan. The advantage of the algebraic approach is the rapid boundary reconstruction, but the main disadvantage is that the method does not calculate the lateral position.

The solution of linear segments starts from a schematically drawn acoustic path model and selecting the first transducer element coordinates as (0,0), which is the origin point. It can be viewed that the calculation is done as usual, but the transducer is rotated, and the object surface is in the horizontal position (Figure 2.7):

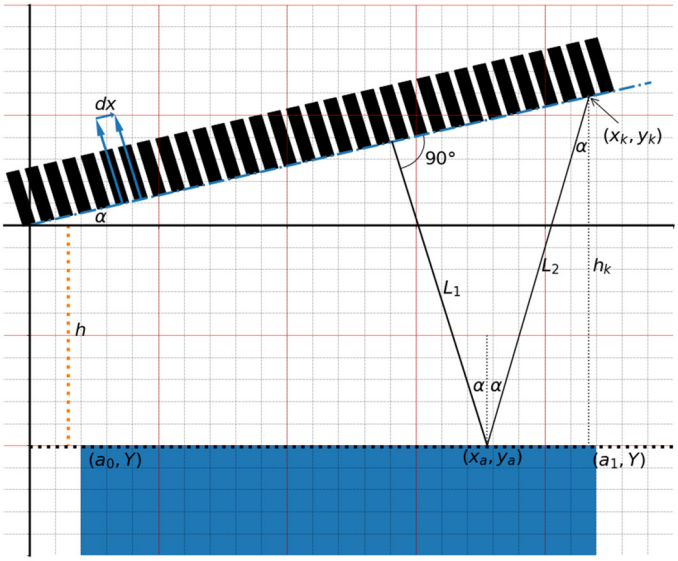

Figure 2.7 Diagram of one possible acoustic path to a sensor with coordinates (x_k,y_k) when the relative angle between the transducer and the sample is alpha α

The following variables can be described (Figure 2.7): the emitting element is always on the left side, and the receiving element is on the right side:

- **h** – distance from the first element to the object surface line.
- **α** – transducer anglerelative to horizontal line.
- **dx** – the pitch between the elements.
- **Y** – the object's vertical coordinate, basically, the height (necessary for further calculations).

- $\mathbf{a_0}$, $\mathbf{a_1}$ –known corner coordinates of the object.
- $\mathbf{(x_a, y_a)}$ – acoustic impact point.
- $\mathbf{h_k}$ – shortest length between the receiving element and the object boundary line.
- $\mathbf{L_1}$ – shortest acoustic path between the object and the emitting element's position.
- $\mathbf{L_2}$ – shortest acoustic path between the received element and the object's surface.

From the first observation in the diagram, it can easily be seen that the time taken from the emission to the reception has the following relationships:

- The sound wave travel time increases linearly with the distance at all angles – it is a linear component.
- When the transducer is rotated, the time at which sound propagates has a trigonometric relationship with the incident angles.

In this model, the acoustic path propagation time from the emitter to the receiver depends on two independent variables (the distance and the angle), which contribute equally to the travel time. We can demonstrate that it is possible to calculate the relative angle of the segment while only knowing the travel time between the two transducer elements. However, if it is only the relative angle information without the y-axis (depth), we call it angle α and have following trigonometric relationship with the acoustic travel path and the angle:

$$\Delta D = (dx \cos^3(\alpha) + dx \cos(\alpha)) \sin(\alpha) \tag{2.13}$$

where ΔD is the difference in the traveled distance (the reflection time) between elements which are separated by dx length with a relative angle between the elements and object surface α; the sizes can be seen as unitless, and only the dimension between ΔD and dx needs to have logical interpretations.

On the other hand, the distance information requires time information based on the real world transmission information (the sample number has physical meanings), and the expression for the calculation is the following:

$$Y = (i-1)dx \sin(\alpha) - \frac{C_w t_i}{2\cos(\alpha)} \tag{2.14}$$

where i is the transducer's element number, numeric values start from 1, dx is the pitch between the transducer's elements, t_i is the known signal peak time, C_w is the speed of sound in water.

Detailed derivation of the method is based on a line equation:

- For line $Ax + Bx + C = 0$, coefficients can be found by using the following system:

$$\begin{cases} \mathrm{A} = \mathrm{Y}_2 - Y_1 \\ B = (x_2 - x_1) \\ C = -Ax_1 - By_2 \end{cases} \tag{2.15}$$

where Y_2, Y_1 are a vertical coordinate endpoints; x_2 and x_1 are end points of horizontal coordinates.

- We transform the length equation:

$$\mathrm{D}_{\mathrm{line}}(A, B, C, x_p, y_p) = \frac{|Ax + By + C|}{\sqrt{A^2 + B^2}} \tag{2.16}$$

The above formula calculates the distance from the line which has A, B, C equation coefficients to an arbitrary point (x_p,y_p), or, in this case, to a point on the surface or the transducer. We note that this formula calculates from the line with an infinite length and not a line segment.

The proposed methods work with the following constraints to make the math simpler:

- The X-coordinate is the lateral position; the Y-coordinate is the height.
- The first ultrasonic element center coordinates are 0,0 – this is the origin point (Fig. 2.7).
- The object is always below the first element (it thus features negative coordinates) (Fig 2.7).
- All other elements' X and Y coordinates are increasing: $Y_0 < Y_1 < Y_2 < Y_n, X_0 < X_1 < X_2 < X_n$. If this is not the case, the coordinate system must be translated and transformed. If the transformation is done by using the affine transformation matrixes, it must satisfy the condition $\det(M) = 1$. In other words, no shear or scaling should be involved.

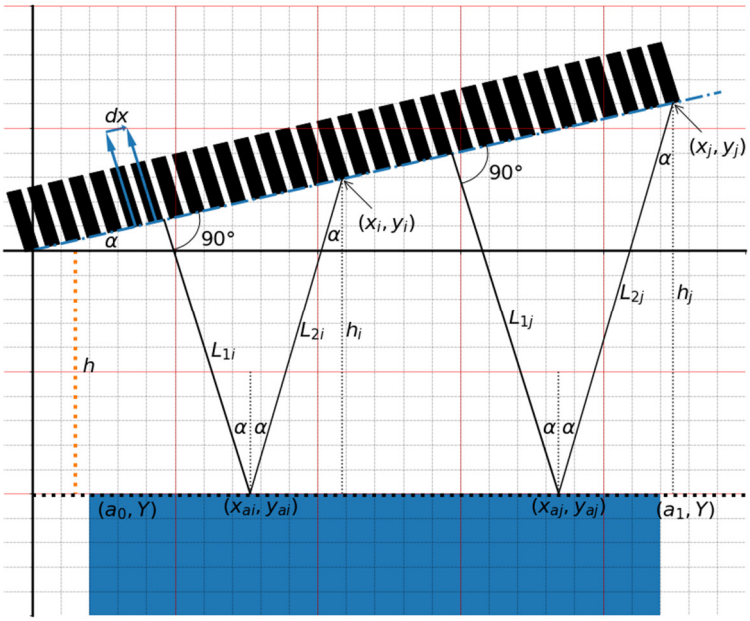

Figure 2.8 Acoustic paths of two receiving elements. In this figure, the transmission and the reflection can be described by right-angled triangles

The total travel distance can be expressed as:

$$D = L_1 + L_2 \tag{2.17}$$

where L_1 is the emitted sound pressure path, and L_2 is the reflected acoustic path (the distances can be found by using Eq. 2.16).

The recorded time conversion to distance which is highly dependent on the speed of sound in water can be written as:

$$D = \frac{t}{C_{water}} \tag{2.18}$$

When having only the sample time, it is more effective to use the time difference information and to sequentially get the angle and then reproject the distance information:

$$\Delta D = \left(L_{1j} + L_{2j}\right) - \left(L_{1i} + L_{2i}\right) \tag{2.19}$$

When using the following constraint: $i < j$ and expanding the line equation (Eq. 2.16), L2 distance can be calculated by using the right triangle cosine rule:

$$L_{2i} = \frac{\left((a_0 - a_1)dx\, i \sin(\alpha) + (a_0 - a_1)h_i\right)\cos(\alpha)}{\sqrt{(a_0 - a_1)^2}} \tag{2.20}$$

$$L_{2j} = \frac{\left((a_0 - a_1)dx\, j \sin(\alpha) + (a_0 - a_1)h_j\right)\cos(\alpha)}{\sqrt{(a_0 - a_1)^2}} \tag{2.21}$$

Eqs. 2.20 and 2.21 can be interpreted in the following manner:

- The dominating part is a line distance equation (D_{line} Eq. 2.16) using algebraic y point position expression (y=dx • i • sin(α)) using formulas. Because of the chosen coordinate system which always has positive x and y values, the modulo operator in solving the square root can be ignored.
- x coordinates are expressed by using the right triangle rule x • cos(α).

In order to minimize independent variables, we replace j -> (i + 1):

$$L_{2j} = \frac{\left((a_0 - a_1)dx\ (i+1)\sin(\alpha) + (a_0 - a_1)h_j\right)\cos(\alpha)}{\sqrt{(a_0 - a_1)^2}} \tag{2.22}$$

L1 path expression is written in the following way:

$$L_{1i} = \frac{(dx\ i\ cos^3(\alpha) + dx\ cos(\alpha)\ )\sqrt{a_0^2 - 2a_0a_1 + a_1^2}}{a_0 - a_1} \tag{2.23}$$

The total distance equation interpretation is as follows:

- The line equation is used twice: first, to calculate the (x_a, y_a) point and again for L2 point calculation (L2 line is used for x_a, y_a point).
- The cubed cosine value indicates that we are combining the alpha angle multiple times, which is visible in the graph.

The total distance when using L1 and L2 combinations is algebraically solved by using Sage mathematical package [223] (it is an algebraic combination of $\Delta D_{i+1} - \Delta D_i$ equation; due to the huge number of terms in the expression, only the final solution is shown):

$$\Delta D_{i,(i+1)} = \frac{(dxcos^3(\alpha) + dx\ cos(\alpha)\ )\sqrt{a_0^2 - 2a_0a_1 + a_1^2}\sin\alpha}{a_0 - a_1} \tag{2.24}$$

Terms $(a_0 - a_1)$ and $\sqrt{a_0^2 - 2a_0a_1 + a_1^2}$ can be reduced because negative results for this method have no physical interpretation in the solution:

$$\Delta D_{i,i+1} = (dx\cos^3(\alpha) + dx\cos(\alpha))\sin(\alpha) \tag{2.25}$$

α angle can be solved by various numerical optimization methods, such as the Newton-Raphson method [224], [225].

Having solved angle α, we proceed to calculate the object surface line relative to the first transducer element. As mentioned above, the method does not calculate the lateral position, thus we choose dummy object-side coordinates, and, for easier math, we use -1 and 1.

Line $Ax + Bx + C = 0$ equation coefficients can be rewritten as follows:

$$\begin{cases} \mathrm{A} = 0 \\ B = -2 \\ C = 2Y \end{cases} \tag{2.26}$$

By using Sage symbolic math software [223] and solving *L1* and *L2* equations, when knowing only the angle and the transducer element's sample time, the relative element distance from the sample surface line is expressed as:

$$D = \frac{dx|\cos(\alpha)| + |2\,dx\cos^2(\alpha) - dx\,|\cos(\alpha)\,i\,dxsin(\alpha) - Y|}{dx|\cos(\alpha)|\cos(\alpha)} \tag{2.27}$$

After rearranging the equation for the *Y* variable, it can be written as follows:

$$|i\,dx\sin(\alpha) - Y| = \frac{D\,dx\,|\cos(\alpha)|\cos(\alpha)}{dx|\cos(\alpha)| + |2\,dx\cos^2(\alpha) - dx|\cos(\alpha)} \tag{2.28}$$

In the left part, the term $i\,dx\sin(\alpha)$ is the active element vertical position (or in other words vertical offset). Taking into account the fact that Y is always negative (it is a natural assumption that the object is always below the transducer), and the angle is always less than 45 degrees, which never yields negative values, the equation can be rewritten in the following form:.

$$Y = i\,dx\sin(\alpha) - \frac{D}{2\cos(\alpha)} \tag{2.29}$$

With Equations 2.29 and 2.25, it is possible to algebraically calculate the linear segment's distance and the angle from the transducer, although the lateral position information is lost and needs to be reconstructed by using other methods.

For the lateral position, the discussion is omitted because on the object's corners the reflection from the plane wave are weaker, and, without experience of the operator, automatic errors with high values will be obtained.

2.3. Conclusions of the Chapter Two

1. The proposed method for surface model reconstruction shows preference to using a FMC style signal capture as its advantage is a more straightforward approximation because, for compensating the weaker signal, the lower frequency can be used, and captured data is ready for the subsequent object inspection step.
2. The weak reconstructed parts of focusing when TFM is used can be interpolated by using B-spline, as it has interpolation properties which are denoted by good match with the real components.
3. A method for the reconstruction of the object's surface by using line segments has been proposed.

3 DEVELOPED ALGORITHM FOR VOLUME RECONSTRUCTION OF A COMPLEX OBJECT

This chapter shall describe the second part of the proposed methodology which involves object volume reconstruction (in this context, object volume reconstruction is a defectoscopy object sample in the 2D dimension). The proposed methodology can be used independently as long as the calibrated CAD model is available, where transformation between samples in the data and in the real world position is known and accurate.

The volume reconstruction focusing (or beamforming) method is created by using the time-domain approach. There are two reasons for using these classical methods. The first is that a reflection from the boundary is difficult to approximate as a point target where most statistics-based methods work correctly. Secondly, when there is a non-regular surface due to complex phenomena, such as diffraction, the refraction of the acoustic path needs to be reconstructed by using the non-analytical approach. The figure below schematically shows the algorithmic route of the volume reconstruction:

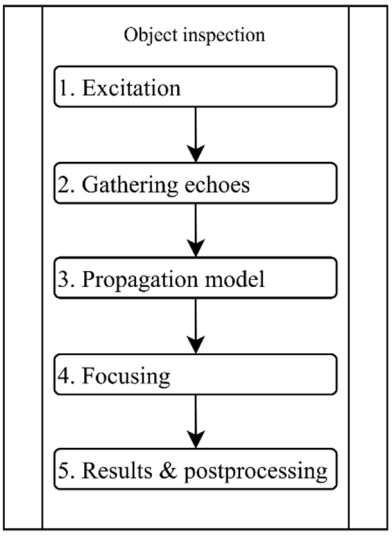

Figure 3.1 Flowchart of the proposed methodology and the required steps

We note that FMC data can be reused for the surface reconstruction, but, due to the limited dynamic range of the equipment, the practical solution is to execute FMC twice with analog hardware of different gain.

Other subparts of the method are independent and are briefly described from the theoretical point of view.

Table 3.1 Object inspection methodology steps; the table is assumed to work with raw data without any additional processing

Step No.	Step procedure	Short description
1.	Excitation	Excitation procedure PWI or FMC
2.	Gathering echoes	Delay alignment and if it necessary multiple shots combination
3.	Surface morphology calculation	Filtering, detrending and backwall removal
4.	'Surface' focusing	Creation of 'image' from B-scan data
5.	Results & post-processing	Results post-processing

The summarized steps are shown in Table 3.1. The volume reconstruction procedure is in practice very similar to the surface morphology procedure, albeit with additional restrictions. One of the constraints is the much lower energy reflected back to the sensors, although it is countered by the advantage that defects can be approximated as point reflectors where it is possible to use statistics-based math.

3.1 Object inspection

The following chapter shall describe the steps necessary for executing the volume reconstruction methodology step by step with an assumption that surface morphology reconstruction has already been performed.

Step 1. Excitation

As it was mentioned in the previous chapter, the main problem of excitation is twofold: firstly, the energy delivery for ROI, and, secondly, the numerical path approximation while using computing resources as little as possible.

Step 2. Gathering echoes

This 'gathering echoes' step faces the same concerns as the aspect of surface morphology. As mentioned above, the relationship between data samples and physical positions needs to be accurate.

Steps 3-4. Surface morphology calculation and focusing

For straightforward propagation modeling, where it is necessary to focus energy from the transducer to ROI, we can derive a fast-approximation method which is based on finding Snell's law angles from the source point, and modeling reflections as ERM. This ERM assumption for Snell's angles is calculated for all the pixels in the image; it is a form of SAFT where only the forward path is taken into account.

For an efficient minimization method, the author has created an indirect Snell's law solution where it is possible to use numeric optimization algorithms for angle searches. Detailed derivation is given in the author's paper [118], and only the principal equations are shown in this chapter, such as the one shown below:

$$\left((T_x - r)^2 + T_y\right)(S_x - r)^2 c_2^2 - \left((S_x - r)^2 + S_y^2\right)(T_x - r)c_1^2 = 0 \qquad (3.1)$$

where *T(x, y)* is the target point coordinates, *S(x, y)* is the source point coordinates, *r* is a point where Snell's law holds, and c_1 and c_2 are the speed of sound

in S and T point's media. The main problem of this equation is that, before calculation, the source and target points need to be transformed and scaled where the boundary line (the border between the media) is in the coordinate space with (0,0) and (1,0) thus doing the length normalization step.

The value of Equation 3.1 is 0 when Snell's law is correct. Otherwise, there is a numerical error value, which is better when it is smaller. This value is simply a numerical expression. After finding the root of the equation, it is necessary to do a final check to make sure that the results match with Snell's law refraction because, mathematically, it is possible to get a physically meaningless result:

$$a_1 sgn(S_x - r) + a_2\left(sgn\, S_y\right) + a_1 sgn(Tx - r) + a_2 sgn\left(T_y\right) = 0 \qquad (3.2)$$

where *sgn* is a sign function, and a_1, a_2 are non-zero arbitrary integer constants whose purpose is to quickly numerically check that Snell's law is valid between the source and the target points (*S* and *T*). Originally, the method was developed to calculate the delay law for ROI where the object boundary is an arbitrary line. For calculation, it is possible to use GPGPU computing because this method can be used in the SIMT multiprocessing mode when using Newton-Raphson root finding. It can be limited by a reasonable number of operations that are between 8 and 10. The solved Snell's law path is set out below.

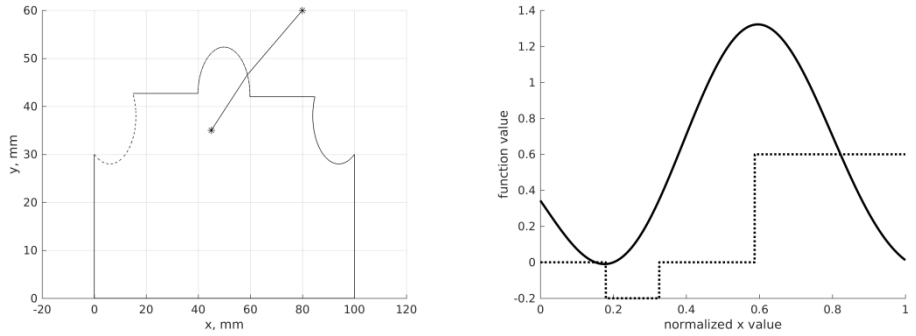

(a) (b)

Figure 3.2 (a) Example figure for Snell's law solving, (b) is the solution space where the solid line is result of Equation 3.1, and the solution is shown for Eq. 3.2 when a_1=0.1 and a_2=0.3

Figure 3.2(b) shows the effects of the fast Snell's solution and why it is necessary to use Equation 3.2. In the mathematical sense, it is a fourth degree equation with multiple correct results, and it is necessary to check if there is a physical meaning.

A more detailed solution of Equation 3.1 is based on the algebraic solution of Snell's law:

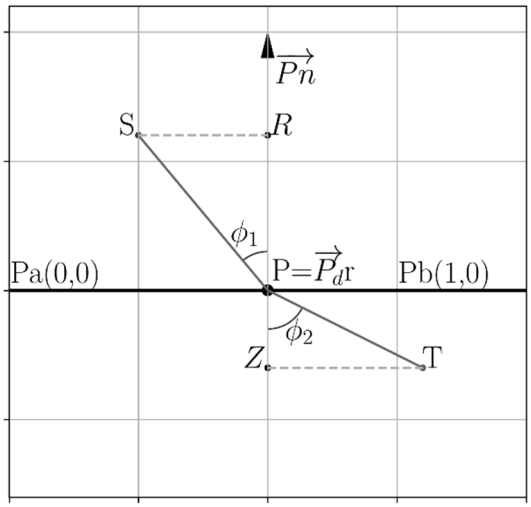

Figure 3.3 Principal sketch of Snell's law

Figure 3.3 shows a principal sketch of Snell's law and **S** (source), **P** (impact), **T** (target) points. As we see, the coordinates along the horizontal axis are in the normalized system between 0 and 1, thus the impact point can be written as vector $\mathbf{P_d}$. With this, Snell's law has the following expression:

$$\sin(\phi_1) = \frac{\sqrt{Pd_x^2 s_r^2 + Pd_y^2 s_r^2}}{\sqrt{(Pd_x s_r + Po_x - S_x)^2 + (Pd_y s_r + Po_y - S_y)^2}} \tag{3.3}$$

$$\sin(\phi_2) = \frac{\sqrt{Pd_x^2 s_z^2 + Pd_y^2 s_z^2}}{\sqrt{(Pd_x s_z + Po_x - S_x)^2 + (Pd_y s_z + Po_y - S_y)^2}} \tag{3.4}$$

where s_r and s_z are the point length from *S* point (vectors) to the subscript point. The terms in the equation are distance expressions, and, after combining formulas, with respect to $\mathbf{P_d}$ and by reducing variables, we get:

$$\frac{-(Pd_x^2 r_x^2 + Pd_y^2 r_z^2) c_1^2}{(Pd_x r + Po_x - T_x)^2 + (Pd_y r + Po_y - T_y)^2} + \frac{(Pd_x^2 r_r^2 + Pd_y^2 r_r^2) c_2^2}{(Pd_x r + Po_x - S_x)^2 + (Pd_y r + Po_y - S_Y)^2} = 0 \tag{3.5}$$

where r_x, r_z, r_r are supporting triangle vectors; most of the equation can be reduced because the use of normalized values gives a lot of reductions, and it makes the formula fully constrained. With the coordinate transformation (the line where the

impact point x is between 0 and 1, and y is always 0), Equation 3.5 can be reduced further:

$$\frac{-(T_x - r)^2 c_1^2}{(T_x - r)^2 + T_y^2} + \frac{(S_x - r)^2 c_2^2}{(S_x - r)^2 + S_y^2} = 0 \tag{3.6}$$

Now Snell's law equation has no trigonometric expressions, and it is in a simplified form, although Equation 3.5 needs to be rewritten in the quadratic form to make its form suitable for the optimization method. Thus Equations 3.1 and 3.2 are required due to reductions.

The advantage of using this method is the possibility to avoid solving nonlinear Snell's law equations [226] or to create virtual elements for limited inspection cases relatively quickly [100], [123], [128], [163], [178], [227], yet with coordinate transformation as the initial step. Although the speed of the proposed method depends on the initial segment size for complex curved objects, most time will be lost in point recalculations for small segments [118].

As it follows from our analysis, direct Snell's law model can be used in the emission mode for an increase of the focusing energy, as, for the receiver, it can be viewed as a SAFT procedure where time delays are controlled. Still, the SAFT style digital lensing method has an advantage as it concentrates its energy on ROI.

In general, the SAFT solution is sufficient for reconstruction so that the acoustic path is modeled by using homogenous media – for example, by using the shortest path methodology. A similar equation can be derived if the object's surface boundary is a line. However, for an irregular shape, where there is no obvious shortest path between the transducer and ROI (Figs. 1.6, 2.3), an alternative model needs to be created. One solution is to calculate only the 'strongest' reflection and to ignore other acoustic reflection in the multi-path environment. Another problem is that multi-path reflections in statistic model-based methods cannot map one-to-one coordinates, which creates an ill-possessed problem (or, mathematically: there are multiple correct results, but it is hard to make a physical interpretation of them). Many methods need improvements in order to work for curved objects, although the relatively low curvature object problem has solutions [45], [46], [54], and the proposed method extends the solution to non-regular curved objects (for example, to organic curves).

In the practical implementation of the method, computer resource limitations need to be taken into account. As a consequence, the alpha-shape direct solution cannot be used, thus the solution needs to be additionally approximated while taking into account the processing power. As we can note, GPGPU [73], [210], [216], [228]–[230] computing can be seen as the natural fit for the algorithmic solution.

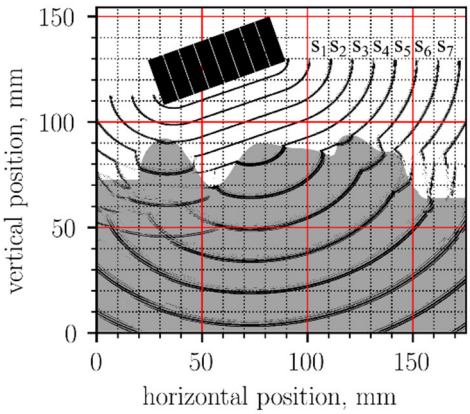

Figure 3.4 Various isolines of wave evolution from phased array transducer

The knowledge of the acoustic propagation model is the critical part. The proposed model is based on Huygens plane wave approximation by using the α-shape (convex hull generalization [231]–[233]), as, from Fig 3.4, we can note that the wave evolution follows the path which can be approximated with the α-shape. It offers an advantage of having an elegant solution of the acoustic path with an additional advantage when an irregular wave front creates splits due to peaks and valleys. Yet, due to resource requirements for computing the α-shape, it can be relatively quickly solved by using the table approach.

As focusing can be done by using Snell's law, it will provide an image limited by the ray nature of Snell's law. This way, it ignores the wave spread effects, as, for other methods, they usually focus only in one environment or, when using limited aperture settings, such as ATFM [163], [176], [234], or else when using the virtual source method [54], [235]–[237] and assuming that the sample boundary is a transducer.

The α-shape [231]–[233], [238]–[242] can be described in the following steps, as suggested by Edelsbrunner *et al*. [232]:

1) Construct the Delaunay triangulation [242]–[244] of the point set;
2) Determine α-extreme point sets;
3) Determine α-neighbors of points (Delaunay triangulation provides the necessary information);
4) Output the α-shape.

Although the algorithm to create the alpha shape is given in simple steps, in practical terms, it is far from being a trivial task for huge point sets, and it takes time to process. This is one of the disadvantages of the proposed algorithm.

The backward model works in the same manner, but it is executed from all the ROI points until all the aperture points are met.

The final step of the method is to sum up the calculated timing results. The formula can be viewed as a conventional TFM method but with a completely different acoustic path model.

When using the GPU solution, the forward propagation modeling approach can be performed by taking the following steps:

a) Creation of the wave evolution model – it is a table in which every point has a wave propagation time.
b) Impact time calculation t0 – calculation of the physical time up to the impact in the coupling medium (water) – for a single transducer model, it can be viewed as the shortest distance between the sample and the transducer's surface
c) The computation of the acoustic wave propagation time while taking into account t0 (graphically, it is a solution of isolines demonstrated in Fig 3.3) is as the effective approach is to use precalculated wave evolution tables (a table with wave propagation times).

The CUDA algorithmic solution is a two-step process. The calculation of the wave propagation time from the object boundary points (algorithm A2 in Appendix) is a straightforward process as long as there is the vector of the initial information (point x,y coordinates and wave propagation beginning), as we can refer in Figure 3.3. With the information regarding approximated acoustic propagation in the sample, the focusing process can be executed by using a method similar to TFM (the pseudocode is presented in Appendix A3).

The solution can be described as the calculation of the shortest acoustic path from the emitter to ROI (by using the wave evolution approximation) and back to the receiver. The main complexity of Algorithm 3.2 comes from the limitation of the GPGPU processor, as there is a huge number of ROI points (as an example, a 2000x2000 pixel table size with 128 emission apertures has 512 million forward acoustic solutions).

The main disadvantage of this approach is that the method is iterative and that using small boundary segment sizes (points) can still take a long time. The initial step of the procedure is to spherically calculate the acoustic path to all the chosen points, or, in other words, to the emission offsets which were saved in set *P* (Equation 2.19).

The proposed method focuses on a procedure which, from the first look, is a modification of the classical TFM while taking into account the GPU limitations [209], [212], [213], [216]. Although TFM is a basic focusing technique which uses only an assumption of the correct acoustic path, but, on the positive side, it only undergoes minimal influence by the noise and other factors, although it still suffers from a lower quality than the statistics-based method. On the other hand, naturally, MV beamformer can be used, which can increase the quality of the point size reflection with additional computing resources.

3.2 Conclusions of Chapter Three

1. For applying energy to ROI, a fast method is proposed. Although the fast Snell's law solution can be used as a SAFT focusing method, it does not solve directly the reconstruction problem, thus an alternative approach is required.
2. The alternative approach to reconstruction is developed by using the spherical wave evolution approach, and it is an approximation with the alpha shape, but, due to the high demand for computing resources, it is necessary to recalculate as much information as possible.
3. The proposed algorithms for GPGPU are created, as, for the final focusing step, the method can be viewed as a modified TFM or as another form of ATFM where only the ultrasonic information is used. One of the algorithm's limitation is the necessity to possess the knowledge of the approximate size of the object.

4 NUMERICAL RESULTS

The purpose of this chapter is to demonstrate the mathematical approximation of the proposed method by using FEA analysis and to create inspection simulation for experiments in a controled environment where all the parameters are entirely known.

The analysis is divided into two parts:

- FEA analysis [91] (due to the limitation, it is performed with a single emission element) – its primary purpose is to demonstrate the first step of the proposed method acoustic wavefront approximation.
- Use of the pencil method (CIVA [83] software) – the numerical experiment is conducted in a controled environment for reconstruction demonstration.

4.1 FEA numerical results

There are multiple problem-solving software packages available, such as *Ansys* [245], which is the composite solution for multiple physics problems, or *Abaqus*. The GRINS Multiphysics Finite Element Package [246], [247] focuses on finite elements, and preparation must be done in the programming language. Even though it is a full software package and, in theory, ready to use, there is still much to be done when preparing a model.

For numerical simulations and resource limits, only single element emission is chosen. It is first, because of the size problem, which, for short waves, uses vast numbers of finite elements, it will take about a week for a single element to be processed even with powerful resources. Second, because of the specifics of the problem and other available modeling methods, there is no point in doing complex FEA analysis. The results can be used to crosscheck theoretical models with wave propagation.

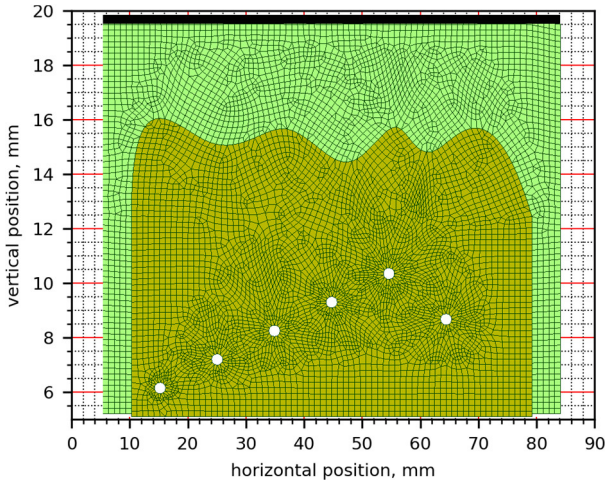

Figure 4.1 Numerical experiment sketch. The black line is an imaginary transducer which creates a pressure wave on the neighboring elements

Table 4.1 FEM experiment parameters

Parameter	Value	Comment
Modeling software	Ansys 19.1	MPI distributed solver using default libraries
Element size	0.05 mm for water 0.1 mm for material	
Timestep	1 ns	
Water element	FLUID29	Ansys 2-D acoustic element,
Solid element	PLANE183	Ansys 2-D structural element with quadratic displacement behavior
Water density	1000 kg/m^3	
Sound speed in water	1499 m/s	
Water element boundary admittance (MU)	0.2	
Material density	1190 kg/m^3	Plexiglas (sound speed of shear waves is 1463 m/s; sound of speed of longitudinal waves is 2730 m/s)
Material elastic modulus	3.1 GPa	
Poisson's ratio	0.37	

Table 4.1 shows the conditions of the numerical experiment, whereas Figure 4.1 shows the experiment sketch. The sample for model is chosen with the idea of having the highest complexity surface for wave propagation (such as convex and concave surface segments). Due to resource limits, only one emission is done, and the main purpose of the FEA model is to show the ability of the proposed methodology to approximate the wavefront.

Table 4.2 FE numerical results

Time step (part in the sub figure)	Explanation
t0 (Fig. 4.2a)	Snapshot of the acoustic front before the impact with the object's surface

t1 (Fig. 4.2b)	Snapshot of the wave propagation in the sample before the reflection from SDH
t2 (Fig. 4.2c)	Snapshot of the wave propagation in the sample after the reflection from SDH

Table 4.2 shows the chosen time steps for the demonstration of approximation; the positions for demonstration are chosen by following this logic: first, the snapshot is the image of the wavefront (t0) before the impact with the surface, second, a snapshot is taken after the impact with the surface before the reflection from SDH (t1), and, lastly, the wavefront is registered after the reflection from SDH and after passing back to water (t2). It is enough for a quick inspection if the method creates interpretable wavefront approximation patterns.

t in Figure 4.2 represents three-time snapshots of finite element method simulations:

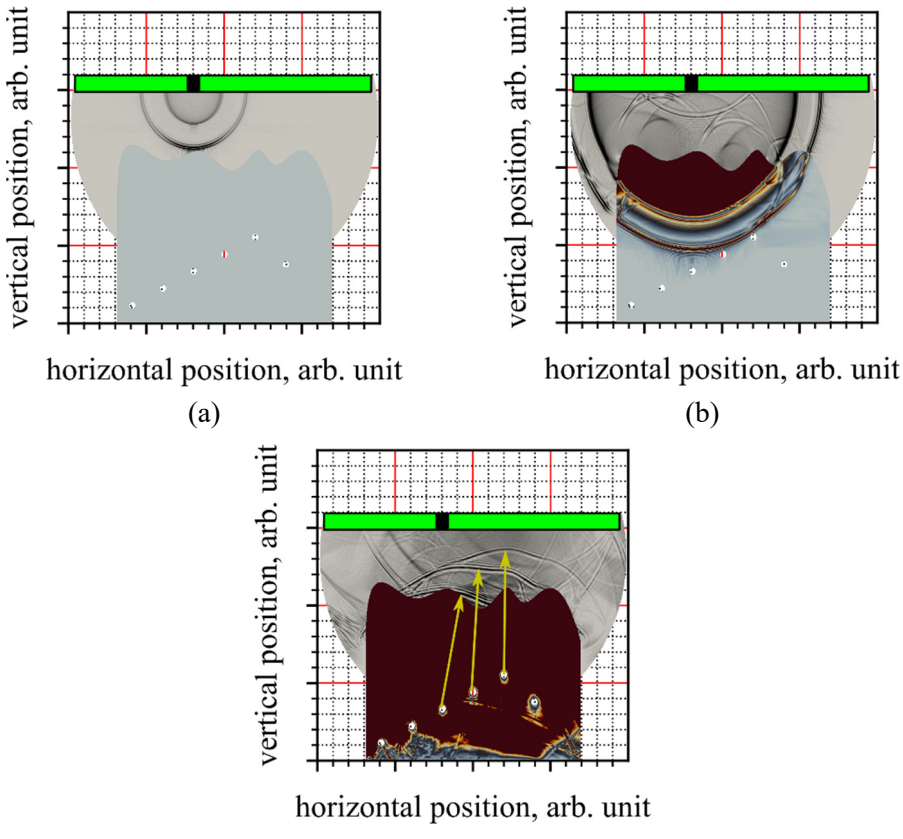

Figure 4.2 Numerical model of the acoustic path propagation (single element emission). The dark spot in the middle is pulse emission; (b) wave evolution before impact against the object; (c) wave evolution after some time has passed, with visibly reflected parabolas from holes

The wavefront is even less intuitive when the surface is curved (Fig. 4.2). The most obvious problem is dispersion which cannot be calculated by using a

straightforward method. As we note, the α-shape is a good candidate method for approximation because of the wavefront structure, and, on the other hand, in order to use this method practically, additional approximation needs to be made as it is shown in Chapter 3.

4.2 Pencil method for phased array inspection methodology

This section discusses the methodology of using the pencil method for fast inspection modeling. For modeling, the CIVA software inspection package is used [101], [104]. The mathematical process is derived with the idea of approximating the plane wave propagation, and it works by calculating the amplitude for distance *r*. When a non-trivial structure is involved, it is still possible to obtain a divergence factor DF, which is based on the given evolution of amplitude. The value of DF can be obtained by calculating the cross-section of the so-called pencil dS by $d\Omega$ solid angle, and it has the following relationship:

$$DF^2 = \frac{d\Omega}{\mathrm{dS}} \tag{4.1}$$

where DF^2 is the divergence factor for the pencil, dS is the cross-section of the pencil, and $d\Omega$ is the amplitude function of the chosen angle.

For the description of the pencil evolution, we can denote the pencil vector: ψ (dx, dy, ds_x, ds_y) and one additional vector which represents paraxial rays. There, we can link the ψ vector with its evolution ψ' (dx', dy', ds'x , ds'$_y$) with the following relationship:

$$\psi' = L * \psi \tag{4.2}$$

where L is the propagation matrix which will be described later. The equation above shows the pencil evolution relationship. The L matrix has the following form:

$$L = \begin{bmatrix} A & B \\ C & D \end{bmatrix} \tag{4.3}$$

where A, B, C, D is a 2x2 submatrix.

4.3 Semi-analytical method results and verification

In this section, numerical verification of the proposed method shall be demonstrated. The analytical results of using the CIVA software package for inspection simulation are shown. The FEM results were not obtained because of the limitation of resources.

The specimens were designed to be similar to real-world shapes. While taking into account the CIVA software limitation, the three main shapes are used (at the time of writing, CIVA software was not supported with b-spline curves at 2D space). The main purpose of the shapes is to involve reconstruction corner cases. What concerns SDH, the defects are chosen randomly:

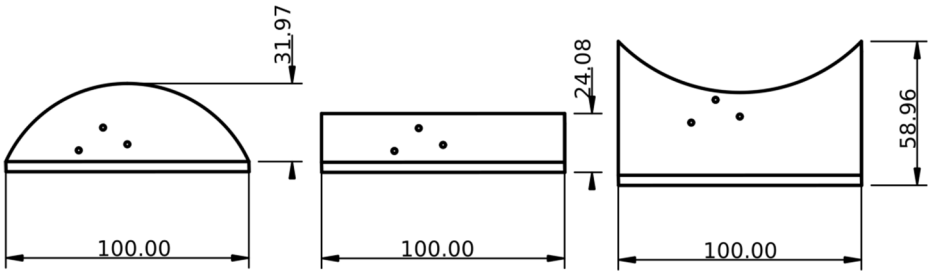

Figure 4.3 CAD sketches for the semi-analytical model. All the sizes are in mm

For the numerical experiment, three distinct surface types are chosen (Figure 4.3), namely, convex, flat, and concave surfaces with known positions of SDH holes with a diameter of 2 mm. The numerical experimental setup is shown in Figure 4.4.

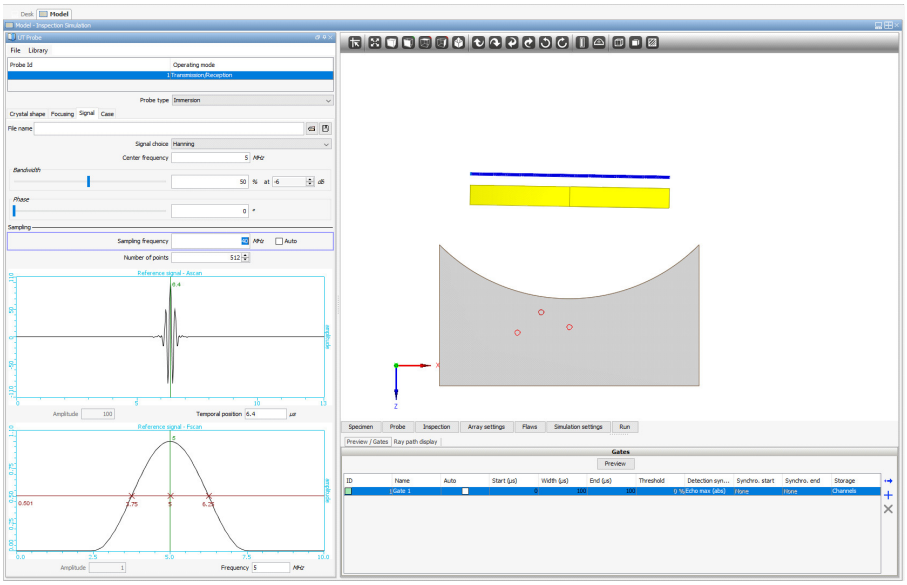

Figure 4.4 CIVA experimental window. The settings for other samples are the same, only the model is changed

First, for the numerical calculation, we performed a PWI B-scan with 2.25 MHz, 5.0 MHz and 10 MHz center frequency pulses while using a 40 MHz sampling rate. The plane wave was mainly used for testing the surface reconstruction method. Then, FMC was performed for the inspection data. The angle between the transducer and the object is kept at 1 degree in order to simulate imperfect conditions which are faced in the real environment.

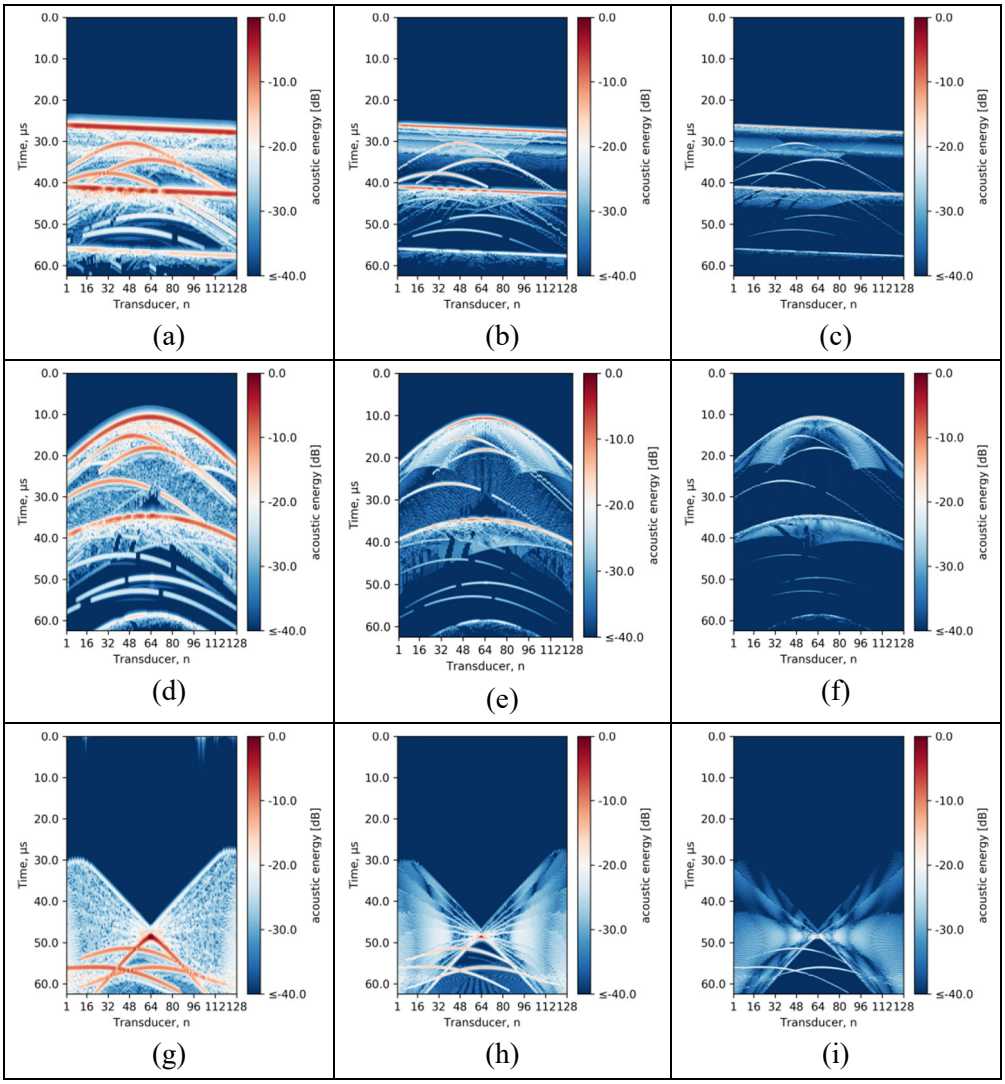

Figure 4.5 Non-filtered numerical results of B-scan when using PWI: (a) is 2.25 MHz central frequency flat object, (b) is 5 MHz flat object, (c) is 10 MHz flat object, (d) is 2.25 MHz convex object, (e) is 5 MHz convex object, (f) is 10 MHz convex object, (g) is 2.25 MHz concave object, (h) is 5 MHz concave object, and (i) is 10 MHz concave object

The numerical results shown in Figure 4.4 were created by using PWI (we note that the computer model used a 128-element transducer with a 0.67 mm pitch, which resulted in more noise in the high-frequency images), the collection interval was set at 60μS; we used 1483 m/s sound speed in water and 2730 m/s sound speed in the material. As the sample is made from Plexiglas, we note from the figure that there is a relatively high level of the numerical noise. The transducer for the experiment used 0.67 pitch and began with the 5 MHz center frequency, while only the pulse center

frequency changed. The acoustic energy is measured with the emission pulse reference signal.

By using the sample object in this experiment, we can note the following points: Figure 4.4(a)–(c) shows the surface curvature for a relatively simple case where it is easy to distinguish reflections from defects, and the parabolas are easy to discern. For Figure 4.4(d)–(f) with a convex surface, object reflections are not obvious, and defect parabolas are coupled with the surface shape. Although a concave surface object is shown in Figure 4.4(g)–(i), we can still note that the reflections from the surface can intersect with the reflections from defects. Therefore, it will be difficult to reconstruct the surface by using any ray-raced methods. On the other hand, we can clearly see the effect of the central frequency on the reflection correlation with the environment. The effect should be treated in the numerical experiment carefully because the visible noise is part of the results of numerical instability. Yet, the higher is the frequency the more expressed is the reflection from the non-regular components, such as the surface and SDH.

By using the already known information about the position and having a digital B-scan by using PWI, we can calculate the accuracy of the flat surface position reconstruction by using the fast method (see Subchapter 2.2):

Table 4.3 Accuracy table when using the flat surface reconstruction method (the method which is proposed in Chapter 2)

Sample with a flat surface and rotated at 1/3/5 degrees		
Frequency	**Calculated angle, degrees**	**Absolute error, degrees**
2.25 MHz	0.919/2.884/4.851	0.08 (8%)/0.116 (4%)/0.149 (3%)
5 MHz*	0.919/2.885/4.861	0.08 (8%)/0.115 (4%)/0.148 (3%)
10 MHz*	0.919/2.886/4.862	0.08 (8%)/0.114 (4%)/0.147 (3%)

As we see from the table obtained by using digital analysis, it is possible to achieve very high accuracy with a relatively negligible effect of the center frequency (as the main reason for this is that the algorithm works by calculating the peak signals).

Although the method can generate results quickly, even without the lateral position, which can be ignored when using large components, it only works with flat surfaces. For other types of surfaces, the reconstruction needs to be performed by using a more conservative methodology:

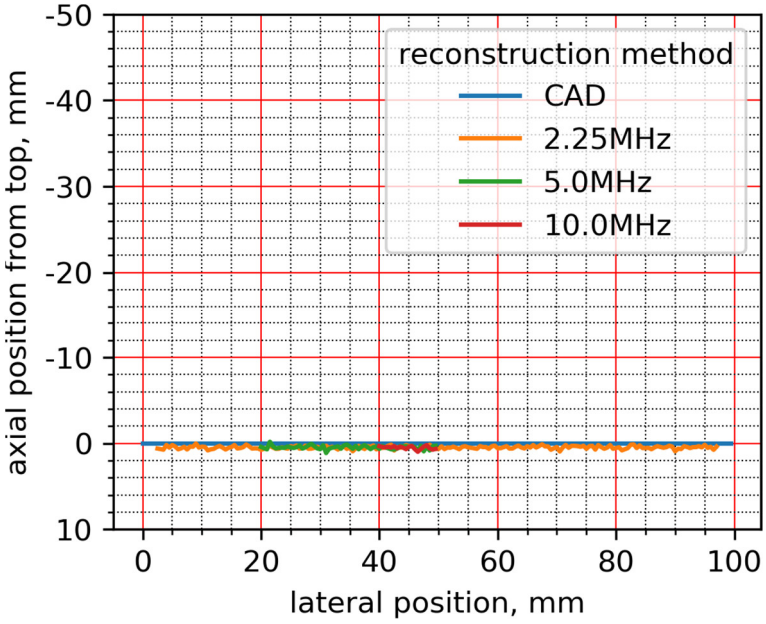
reconstruction method
CAD
2.25MHz
5.0MHz
10.0MHz
axial position from top, mm
lateral position, mm
-50
-40
-30
-20
-10
0
10
0
20
40
60
80
100

(a)

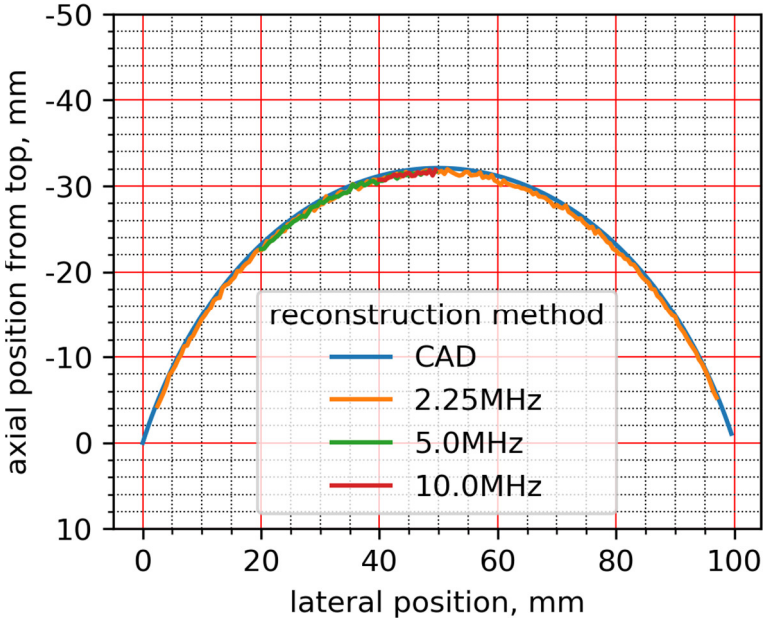
reconstruction method
CAD
2.25MHz
5.0MHz
10.0MHz
axial position from top, mm
lateral position, mm
-50
-40
-30
-20
-10
0
10
0
20
40
60
80
100

(b)

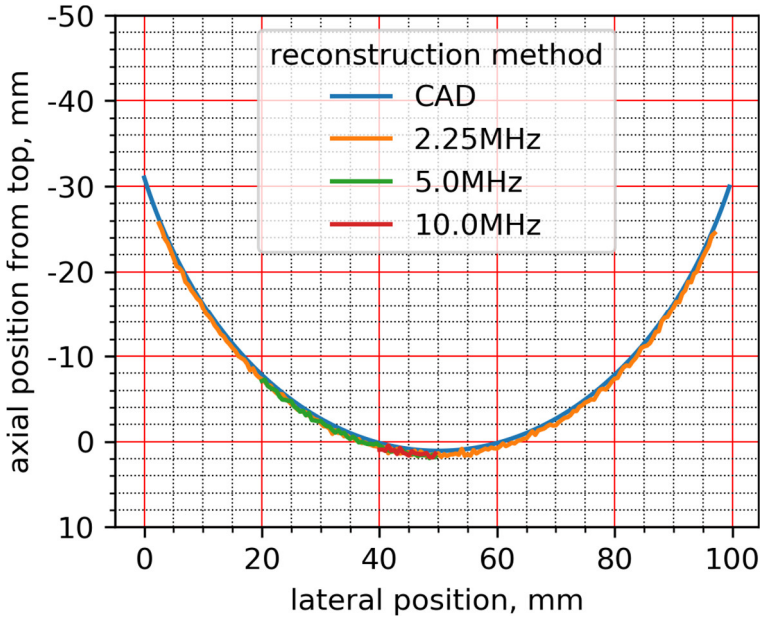

(c)

Figure 4.6 Reconstructed surface from numerical results when using 2.25, 5, and 10 MHz centre frequency. (a) – flat object , (b) – half-circular convex object, (c) – concave object

Figure 4.5 shows visible reconstruction errors. When using the data of a numerical experiment, there are no substantial changes between different frequencies. For numerical measurement, the reconstruction accuracy with the CAD model has to be checked. Because of the numerical experiment environment and the fixed sample rate (40 MHz), as it is expected, the surface reconstruction can be done with virtually minimal errors, although, in the real experiments, the reconstruction error is much more prominently expressed.

The numerical error of surface reconstruction is presented in Table 4.4, and the method for the reconstructed data with the CAD model was aligned by using the least square method (see Eq 5.1 for the principal equation), thus the position in Figures 4.4–4.6 is based on the CAD model coordinate system:

Table 4.4 Numerical simulation surface reconstruction accuracy table

Sample	**Error, average (Maximum absolute) mm**		
	2.25 MHz	5.0 MHz	10.0 MHz
Flat	0.3 (0.5)	0.3 (0.5)	0.3 (0.5)
Convex	0.81 (2.45)	0.81 (2.45)	0.81 (2.45)
Concave	0.81 (2.45)	0.81 (2.45)	0.81 (2.45)

From Figure 4.6, we see that there is no correlation with the wavelength size, especially in the curved areas (although in real experiments the correlation is visible).

Yet, in numerical experiments, for the surface reflection, the error due to the absence of noise is not visible. This is mainly because reflected energy with lower frequencieshave less algorithmic noise..

The experiments were done by using the golden standard total focusing method (TFM) with the sound speed as the reference; then, we performed the fast iterative SAUL algorithm (it should be noted that CIVA implementation uses idealized surface information) and implemented the proposed method.

As for numerical accuracy, we can calculate this by using the manual ‘stencil’ mode. The next step in our verification is to execute the proposed algorithm before comparing the final result with the known model. In Figures 4.7–4.9, the visual representation of results is shown:

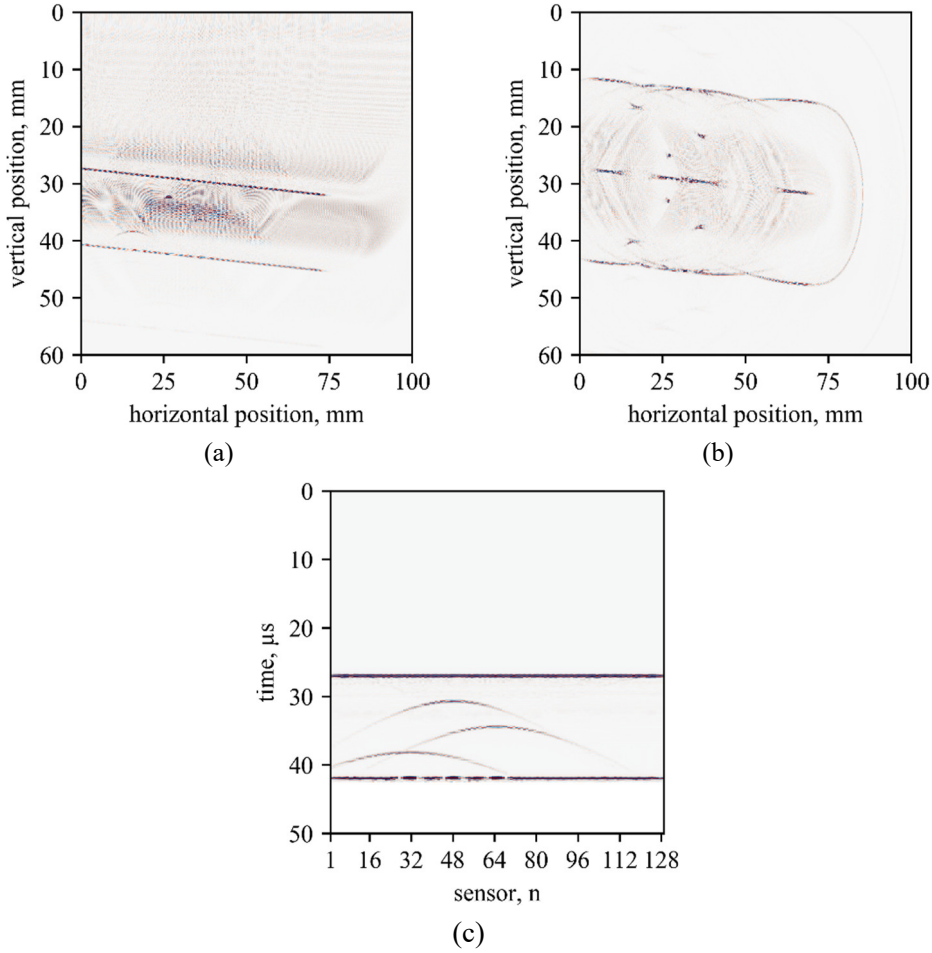

Figure 4.7 Comparison of results of a figure with a flat surface: (a) – classical TFM, (b) – the proposed method (when using 16, 48, 64, 112 emission results) and showing raw results, (c) – SAUL

In the unprocessed results, there is a symmetric pattern due to the negative axis (Fig. 4.7b). For the reconstruction, we used 4 emission elements, and, due to this fact, the ‘reconstructed’ surface has holes. Additionally, it can be noted that with the absence of real damping, the quality of the reconstruction suffers from sidelobes.

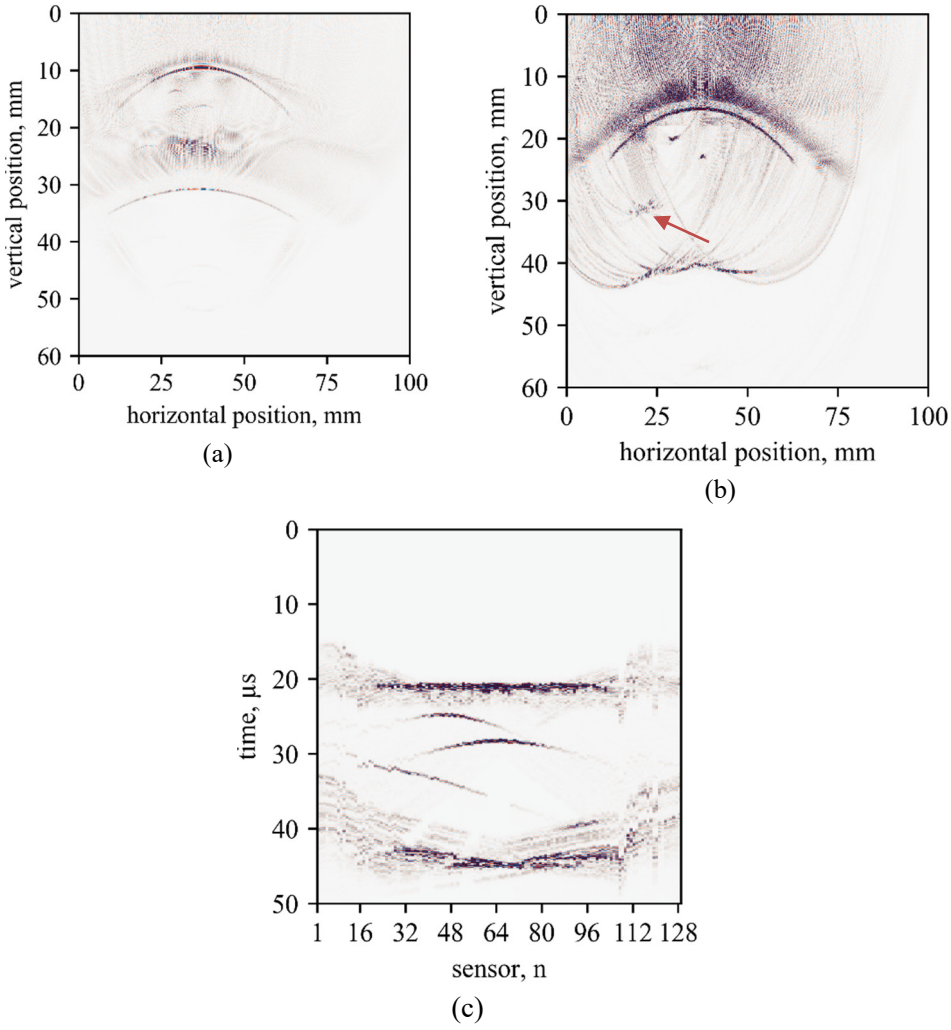

Figure 4.8 Comparison of results of a figure with a flat surface: (a) – classical TFM, (b) – proposed method (when using 16, 24, 48, 80 emission results) and showing raw results, (c) – SAUL

For the case of a convex object, the numerical experiment was influenced by the wave propagation interaction due to the transducer’s angle. We obtained the level where the bottom defect (Fig. 4.8b) can be noted as visible, but still has poor resolution, additionally, for the sake of clarity, Fig. 4.8b results are a composite image with TFM surface reconstruction.

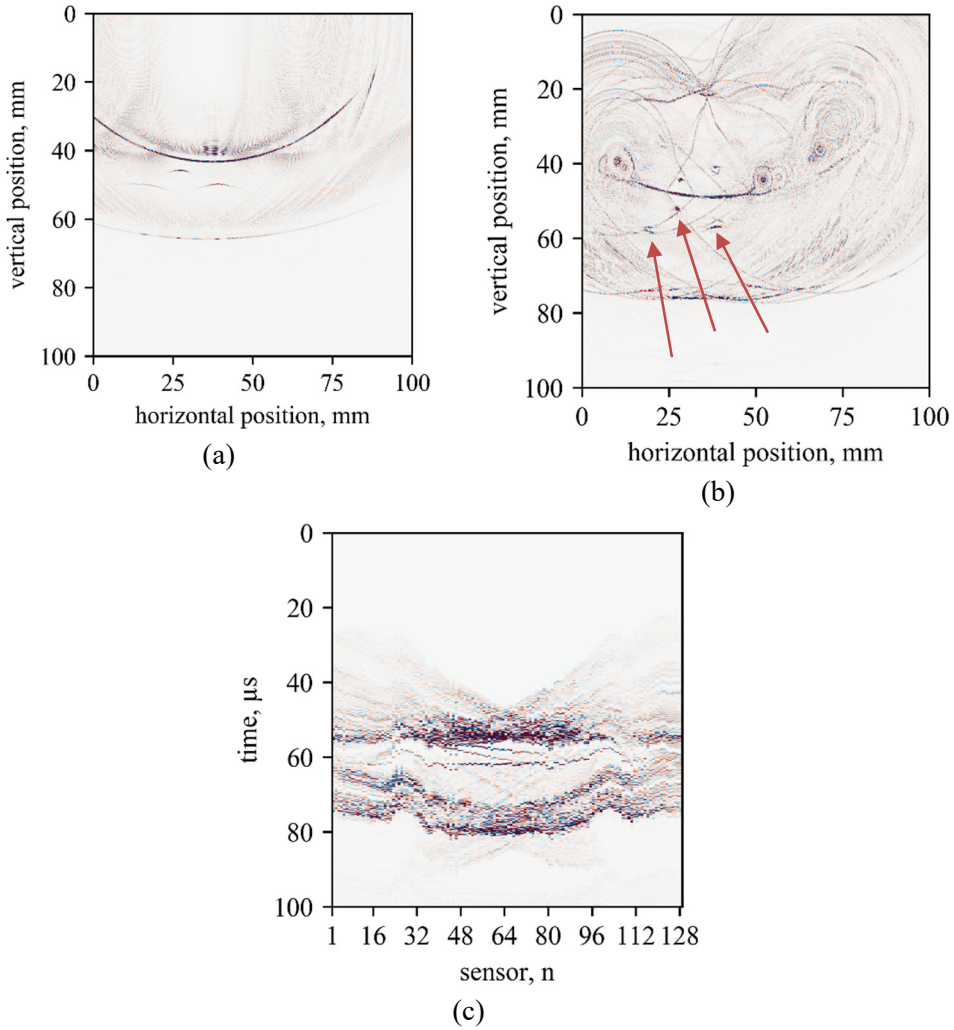

Figure 4.9 Comparison of results of a figure with a flat surface: (a) – classical TFM, (b) – proposed method (when using 16, 48, 64, 112 emission results) and showing raw results, (c) – SAUL (CIVA implementation diverged)

From Figures 4.7 and 4.9, we see that there is an error associated with the algorithmic processing and noise, known as the speckle noise. As this is a reconstruction, additional speckle noise removal does not need to be processed. Additionally, with an irregular surface, approximation errors (or speckle noise) are visible too, with coupled surface reconstruction irregularities as shown in Fig. 4.9. have visible results in final image and without additional guidance is hard to interpret.

The numerical values of the positions are presented in the following table:

Table 4.5 Positions of the reconstructed defect (only taking the best results)

	Defect (SDH) position error from the CAD model, (Δx, Δy) mm		
Object	SDH1	SDH2	SDH3
3.8a	(0.1,0.2)	(-0.1,0.2)	(0.1,0.3)
3.8b	(0.2,0.3)	(-0.2,0.3)	(0.4,0.5)
3.8c	(0.4,0.6)	(-0.3,0.5)	(0.6,0.7)

From the Table, we can note that the digital noise wave exerts a huge influence on the methodology as the speckle noise has a negative impact. On the other hand, the reconstruction demonstrates the method's feasibility for the detection of the position.

4.4 Conclusions from Chapter Four

1. Modeling using FEA can approximate the most accurate physical behavior, but it uses a lot of computing power, whereas, when using the CIVA software, a full FMC can be modeled using by less resources. Although FEA does capture all the phenomena which can be displayed for further analysis, CIVA or raytraced modeling create final modeling results which are similar to using the real hardware for inspection, although the numerical noise is still visible.
2. The performed FEA numerical results demonstrated the complexity of the wavefront in the case of a sample with complex geometry.
3. The performed CIVA numerical simulations demonstrated the algorithm's performance in the idealized environment without complex damping phenomena which have an influence on the results, although, with the performed algorithm, it is still possible to detect the fact of the presence of defects.
4. The proposed method with the chosen shapes provided the accuracy in the range of 2mm in controlled envirioment, although accuracy is calculated on the grounds of an assumption that as long as there is acoustic energy and it touches any region of SDH, it is assumed to be a good match.

5 PRACTICAL APPLICATIONS

What concerns the practical application of the proposed methodology, it is the inspection of various objects when the only known information is the speed of sound in water and the speed of sound in the material. Further practical experiments are divided into two parts: first, surface reconstruction, and then, full inspection after the surface reconstruction step has been completed.

5.1 Samples with the known CAD model

The practical application verification is done on samples with known CAD models and defects, as shown in Figure 5.1. The samples were made in order to depict the extreme cases of real objects. Flat surfaces were used to perform relatively straightforward verification of the proposed methodology possible. The samples are made from Plexiglas ($C_{plexigas}$=2.830 m/s). The defects are two mm-diameter side-drilled holes with known coordinates. The coordinates are fixed from the left bottom corner point of view (Fig. 5.1):

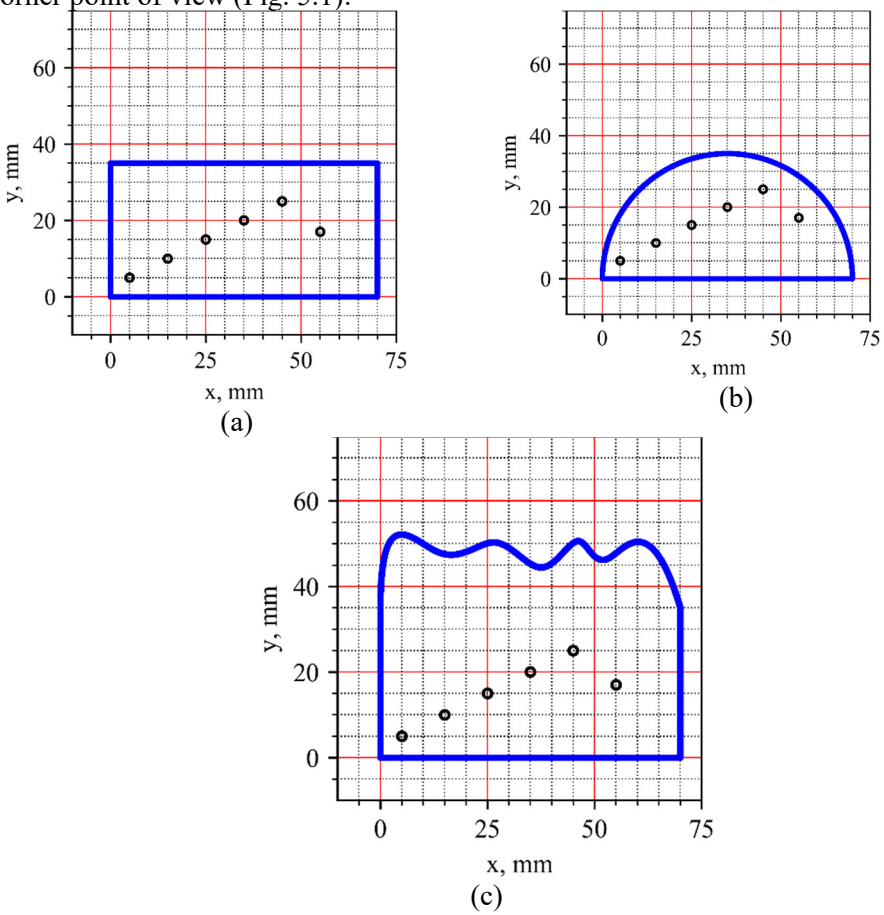

Figure 5.1 CAD models of experimental samples

As the samples are real objects, they are 35mm thick along the Z-axis. As for the position of the defects, it is given in Table 5.1 below (the coordinates of the defects begin at the bottom left corner):

Table 5.1 Sample SDH positions

	Defect (SDH) center position, (x, y) mm					
	SDH1	SDH2	SDH3	SDH4	SDH5	SDH6
Position	(5,5)	(15,10)	(25,15)	(35,20)	(45,25)	(55,17)

In the course of our real-world experiments, it is better to express the SDH positions in relative terms. There are two advantages of this expression: one is that the sample position does not need to be calibrated with respect to the transducer, and the other is that the positions are pre-calculated for relative mathematical stencil-matching and can be used for numerical error expressions.

Table 5.2 SDH with the relative position. For convenience, the highest SDH is taken as 0,0

	Defect (SDH) position, (x, y) mm					
	SDH1	SDH2	SDH3	SDH4	SDH5	SDH6
Position	(-40, -20)	(-30, -15)	(-20, -10)	(-10, -5)	(0,0)	(10, -7)

The relative positions table is calculated with the 'highest' point as the reference start. In the mathematical sense, there is no difference whichever point is chosen, but, from the experimental point of view, it can be noted that, due to losses, SDH5 will have the highest energy reflection.

5.2 Equipment for practical application

The equipment used for practical application was *Dasel Sitau*. The parameters used during experiments are given in Table 5.3:

Table 5.3 Experimental parameters

Component	*Value (comment)*
Phased array equipment	DASEL SITAU 128:128:1
Sampling rate	40 MHz
Probe center frequency	2.25 MHz
Probe pitch	0.75mm
Probe aperture	128 elements
Pulse	220ns length 100v amplitude spike
Reception delay	1600 samples (40 μS)
ADC	13 bit signed

Storage	4096 samples 128 channels
Pre-process$_1$	Signal detrend
Filtering	Low-pass 10Mhz transition frequency
First element movement positions	0, 62mm, 107.1mm
GPU for processing	NVIDIA 1080
CPU	Amd Ryzen 2700x with 2999 Mhz DDR4 RAM

As for the numerical calculation, the data grid is 2000x2000 points size using a 0.05 mm horizontal and vertical pixel size. The time taken for inspection using NVIDIA GTX 1080 is stable, although it depends on the data due to internal processing, in Table 5.4, it can be divided in the process of inspection into two steps with their own times:

Table 5.4 Inspection time

Calculation component	Time, s	Comment
Environment focusing (TFM)	~8s	Depends on the area and sample data
Object inspection	~4.5s	Depends on the sample data, GPU boost speed

It should be notes that object inspection is for one emitter, as, for using 128 elements aperture, the total processing time is 10min (8s + 128 aperture*4.5s, although the part of the object's inspection can be parallelized with multiple GPUs).

The experimental setup (Fig. 5.2), apart from the UT equipment, involved a container for water and a synchronized control system for the *Dasel* equipment.

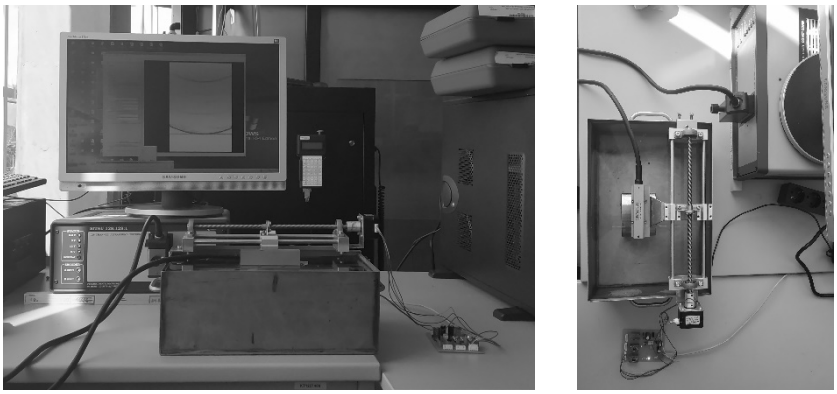

(a) (b)

Figure 5.2 Experimental setup (a) – Side view; (b) – Top view with an immersed sample

Physically, the most critical part is the computer-controlled scanner of the transducer. If the scanner is not sturdy enough, then the results between multiple sessions can be distorted. The principal sketch is presented in Fig. 5.3.

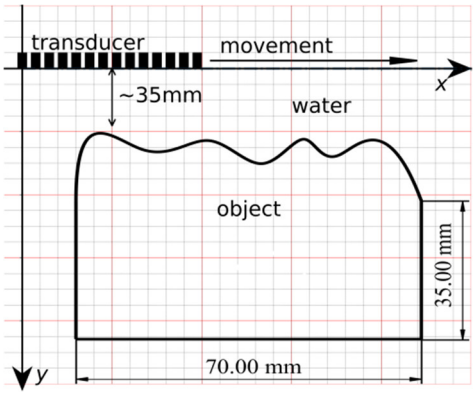

Figure 5.3 Sketch of the experimental setup, for example, a wavy object is shown

Figure 5.3 shows a sketch of the experiment where the object is in water, and the scanner moves in one direction only. The distance between the transducer and the object is about 35mm or more, and the main profile of the object is aligned with the transducer having the minimal possible rotation.

One problem in practice is the oversaturation of results, or, in other words, when the pressure of the wave is out of scale. This can be picked up by the equipment.

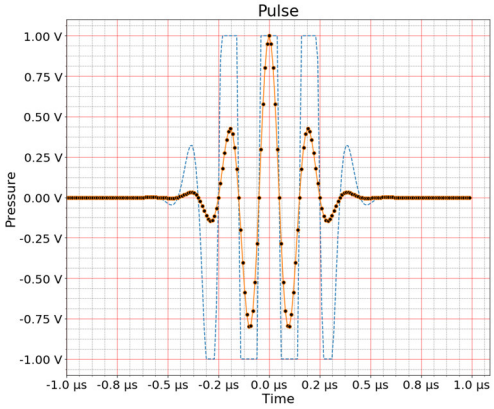

Figure 5.4 Example of ideally reflected and oversaturated pulse. The units are normalized (1V – maximum transducer pressure)

In practical terms, ADC has a limited resolution and voltage [248]. For the experiments, *Dasel Sitau* 128:128 equipment with 12-bit resolution (4,096 distinct values) and 40 MHz sampling rate was used (Table 5.3). Another problem which directly affects the results is the gain parameter that can be set automatically (for example, an incorrect gain setting will result in the saturation of the results – we highlight the dashed line in Figure 5.4).

The most trivial solution to avoiding over-saturation is to reduce the gain or to use a weaker pulse signal. However, the sample and the environment do not change rapidly, and the gain can be manually adjusted by the operator or computed algorithmically by using multiple shots – for example, by using a high pulse on the sample, as shown in Figure 5.5.

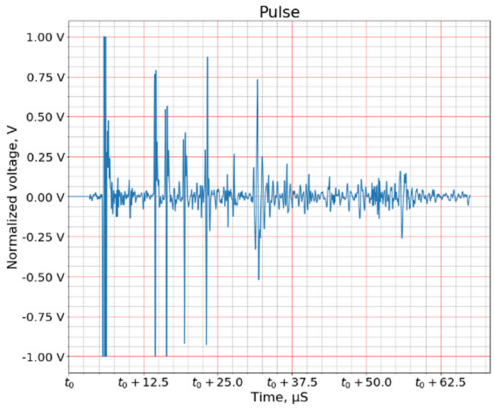

Figure 5.5 Real A-scan of the experimental sample. The first peak is a reflection from the surface, while the second peak is from the back wall of the sample. Other reflections (peaks) are reflections from multiple paths. The signal is for demonstration purposes only

Figure 5.4 visually shows the gain problem, and the first peak is saturated (the maximum voltage value). If only the signal envelope is necessary, the saturated gain can be ignored, but if direct signal processing is involved, oversaturated values simply introduce wrong signal positions. On the other hand, if the gain is lowered, the reflections from the defects (the peaks between the first peak and the second peak) are barely visible, as shown below.

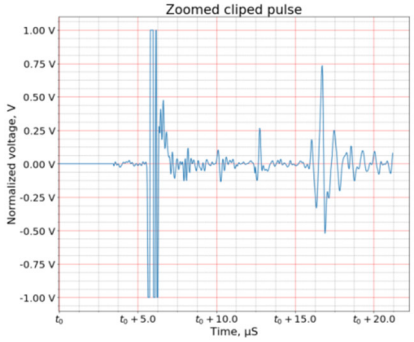

Figure 5.6 Same pulse as the previous figure, but with a weak visible reflection

The gain problem is more visible when the figure is complex, and only a certain fraction is reflected. One of the solutions would be to scan the item with multiple gain settings – for example, by using low gain settings for the surface reconstruction and high gain settings for inspecting the object, or else to use automatic gain correction

methods [249], [250]. However, this setup adds complexity and jitter to the measurement system.

5.3 Experimental results

The surface reconstruction experiment shows the feasibility of the surface reconstruction algorithm when using only an ultrasonic transducer. The experiment was conducted by using three different shapes as shown in Figure 5.1, and the experiment was conducted by using the following procedure:

1) A prepared container with water and the calculated speed of sound in water.
2) The sample is put in a container, and it is scanned in the following way:
    a. By using PWI (operator-adjusted hardware gain in order not to oversaturate the reflection).
    b. By using FMC for the surface (adjusted hardware gain).
    c. By using FMC for object defects (adjusted hardware gain by SDH3 reflection.
3) Collected data is filtered and detrended.
4) The surface calculation methods are performed (case of Fig. 5.1d is displayed).
5) The object defectoscopy algorithm is performed.

As for results, the DAS, TFM and MDAS method for surface inspection is demonstrated in Fig 5.7:

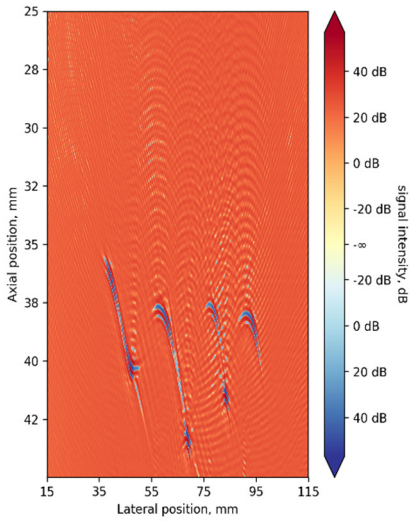

(a) DAS 1° step

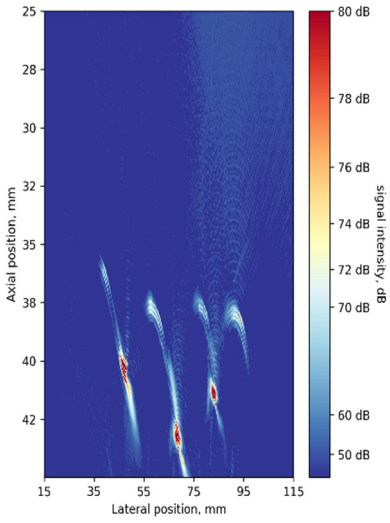

(b) –MDAS 1° step

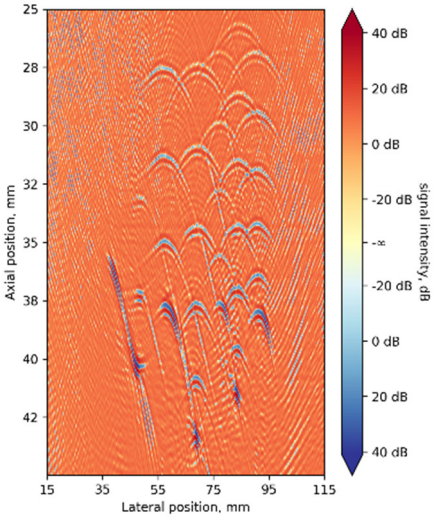

(c) – DAS 5° step

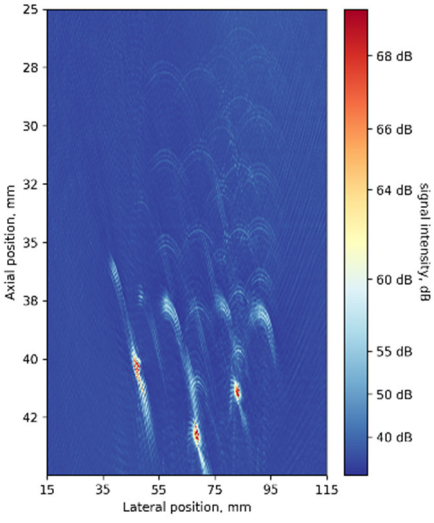

(d) – MDAS 5° step

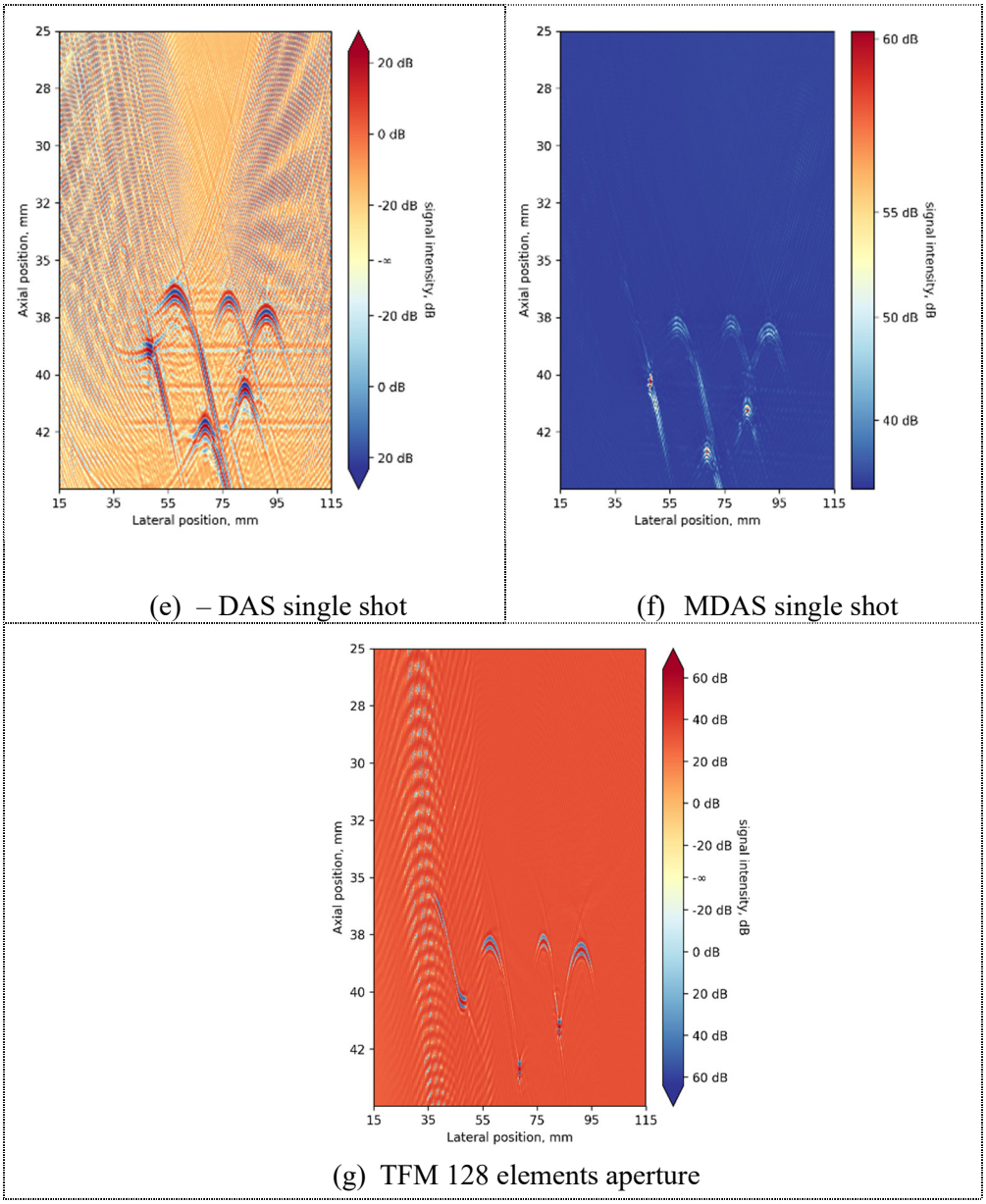

(e) – DAS single shot

(f) MDAS single shot

(g) TFM 128 elements aperture

Figure 5.7 Focused B-scan data used in image reconstruction, a,d,f – DAS algorithm, b,e,g – MDAS (note the linear color scale) and c – TFM. The data is shown without a filter

A complex surface for reconstruction was chosen as an object with a surface which can be b-spline approximated (Figure 5.1c).

Figure 5.2 shows the experimental setup for complex reconstruction, and, in this application, we care only about the object's surface.

The algorithms used for the reconstruction are described in Chapter 2 in the first part of the method description. As for the complete experiment, the three main methods were used: DAS, MDAS and TFM.

After preparing the pixels for curve reconstruction, a point was chosen by finding the highest energy peak on each lateral position step. For this experiment, the selected b-spline grid size involved 0.1λ, 0.25λ, 0.5λ, 2λ (along the X-axis). Visually, the interpolation with various wavelengths has little dependence (Fig 5.8), although, it should still be noted for very small grid sizes that the ringing effect can create false representation data, as it is visible in the following figure:

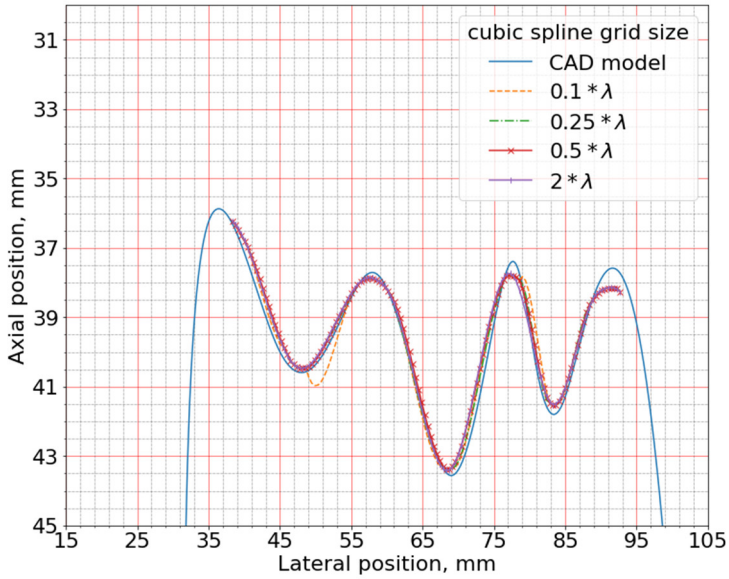

Figure 5.8 Surface reconstruction using TFM. We note the over-fitting with a small grid size

When using the delay and sum reconstruction method (Fig 5.9), visually, the best results were obtained by using the reconstruction grid with 0.25λ grid size; due to the nature of the plane wave, the reconstruction quality visually looks much worse, but, as we can note, numerically, later, the error is not prominently higher:

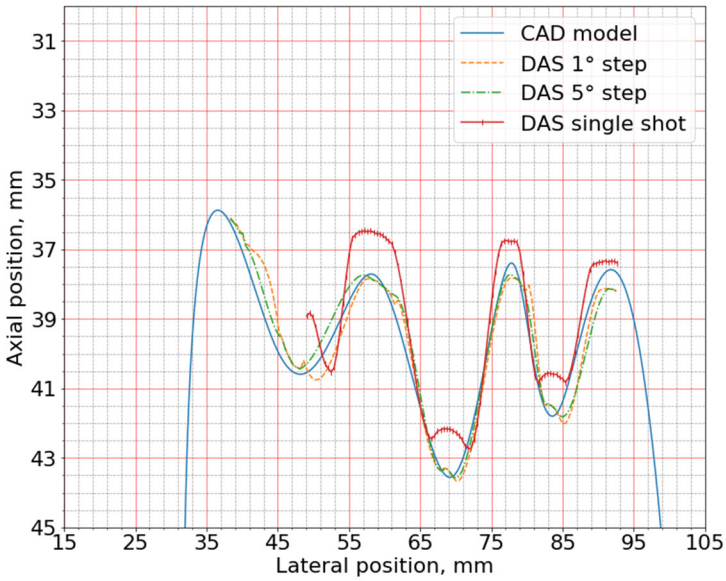

Figure 5.9 Surface reconstruction using DAS imaging with 0.25-wavelength interpolation grid size

The average error for TFM was approximately 0.5 mm, with one more significant error for a sharp peak. For DAS, the reconstruction error was more significant while taking into account the fact that there was no compensation for the transducer.

The reconstruction accuracy can be evaluated by using an optimization technique, such as the Broyden–Fletcher–Goldfarb–Shannon algorithm [251], or by using the least-squares optimization method in any linear algebra packages, such as the python scipy package *scipy.optimize.minimize* method [222]. This method is applicable as long as it can solve the following mathematical problem:

$$\epsilon = \min_{x,y,\phi} \sum \left((C_x - R_x)^2 + (C_y - R_y)^2\right), where\ C_{x,y}\ is\ rotated\ by\ \phi\ and\ translated\ by\ (x,y) \quad \textbf{(5.1)}$$

where ϵ is the estimated error, R is the reconstructed spline point, and C is the CAD model point. It should be noted that, when using translation, not all the discrete points can cover $\boldsymbol{C}$ and $\boldsymbol{R}$ sets, thus necessary the set limit is necessary (in this work, the error numeric value is taken into account when at least 95% points of $\boldsymbol{C}$ and $\boldsymbol{R}$ sets can cover).

In numerical terms, we calculated the absolute maximum error and the mean error of reconstruction by using the best horizontal grid-step. The single-shot results were omitted because they did not provide any meaningful information. Detailed error estimation is shown in Table 5.5.

Table 5.5 Error estimation table.

Method	Maximum absolute error of Δx	Average error
TFM	0.60 mm	0.24 mm
DAS (1-degree step)	0.54 mm	0.18 mm
DAS (5-degree step)	0.65 mm	0.22 mm

From Table 5.5, it is evident that TFM did not yield the best results. The primary source of the error was the lack of reflected energy coupled with the transducer's delays. As for the experiment, even when doing iterative sound speed correction and taking into account the environment inhomogeneity it would take additional time and new assumptions about sample. Aditionally, *a priori* knowledge of the speed of sound would reduce the error, but, here, the worst case scenario was investigated by assuming that the accurate speed of sound is not known and cannot be measured.

This chapter shall demonstrate that, when using an object of a complex shape with ~0.6 mm wavelength center frequency and a 128-element transducer, it is possible to reconstruct the surface with a 0.18–0.24 mm average error, which is about half of the wavelength.

5.4 Experiment of the inspection of defects

In this section, the final results of the proposed methodology shall be presented. The previously presented samples (Fig. 5.1) were used. Before studying the results, we can expect a slightly worse position information because of the environmental impact.

The accuracy of the results was evaluated by matching the computer models of the defects with the reconstructed image. For our reconstruction, 3 shots with an aperture of 128 elements are used, except in the 'wavy' case, because of the cumulative error it is still necessary to perform an additional step of error correction. In the second step, the known information with the reconstructed information was overlaid.

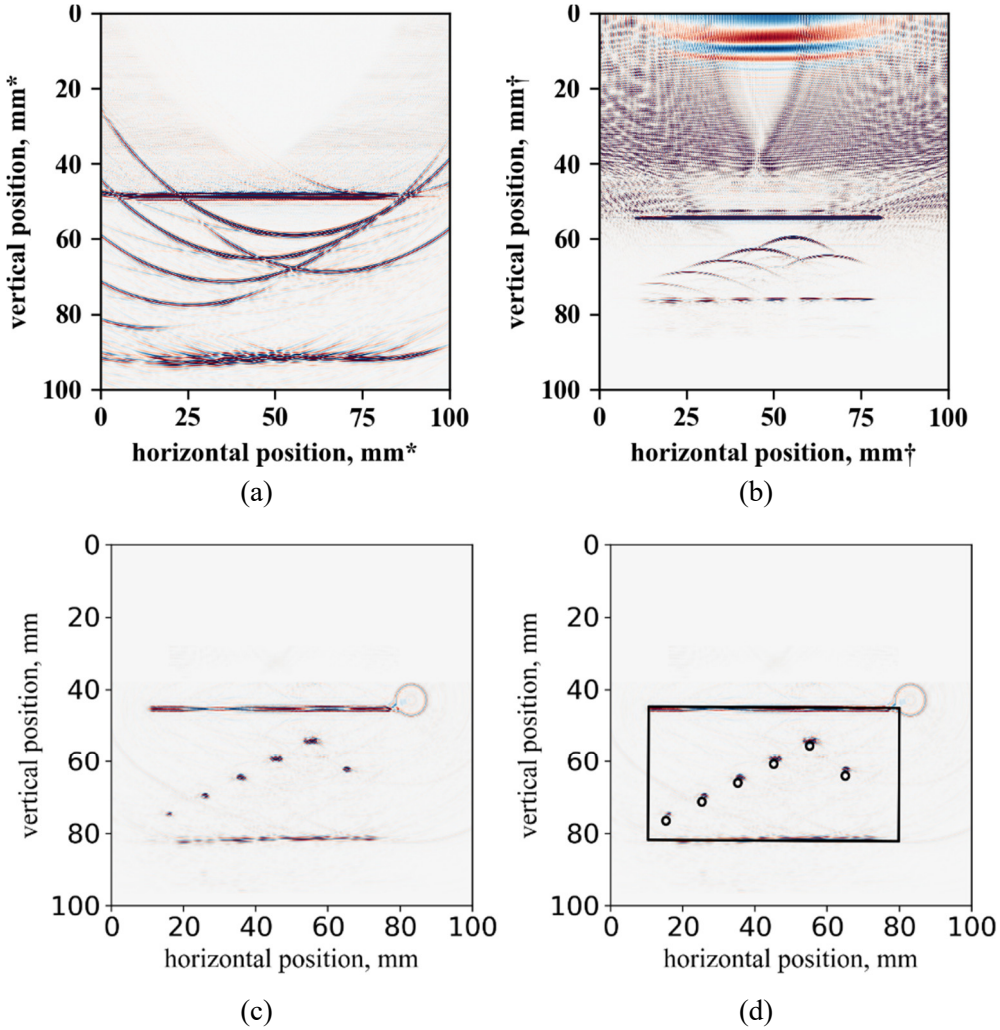

Figure 5.10 Object from fig 5.1a: (a) – TFM using c_1 sound speed (b) –TFM using c_2 speed of sound, (c) – the proposed methodology (d) – the proposed methodology with overlay; the object (position coordinates are calculated * – assuming that the environment is homogenous with C2 speed of sound, †p – assuming that the environment has C1 speed of sound)

When using the regular shape for the proposed method, the reconstruction image has good lateral resolution. The matched CAD template of the object (Fig. 5.1a) has a good match (the circle in Fig. 5.10c and 5.10d has a processing artifact – the reconstructed circle due to the corner point position error).

As for the convex shape (Fig. 5.11), the reconstruction has more noise and increased errors:

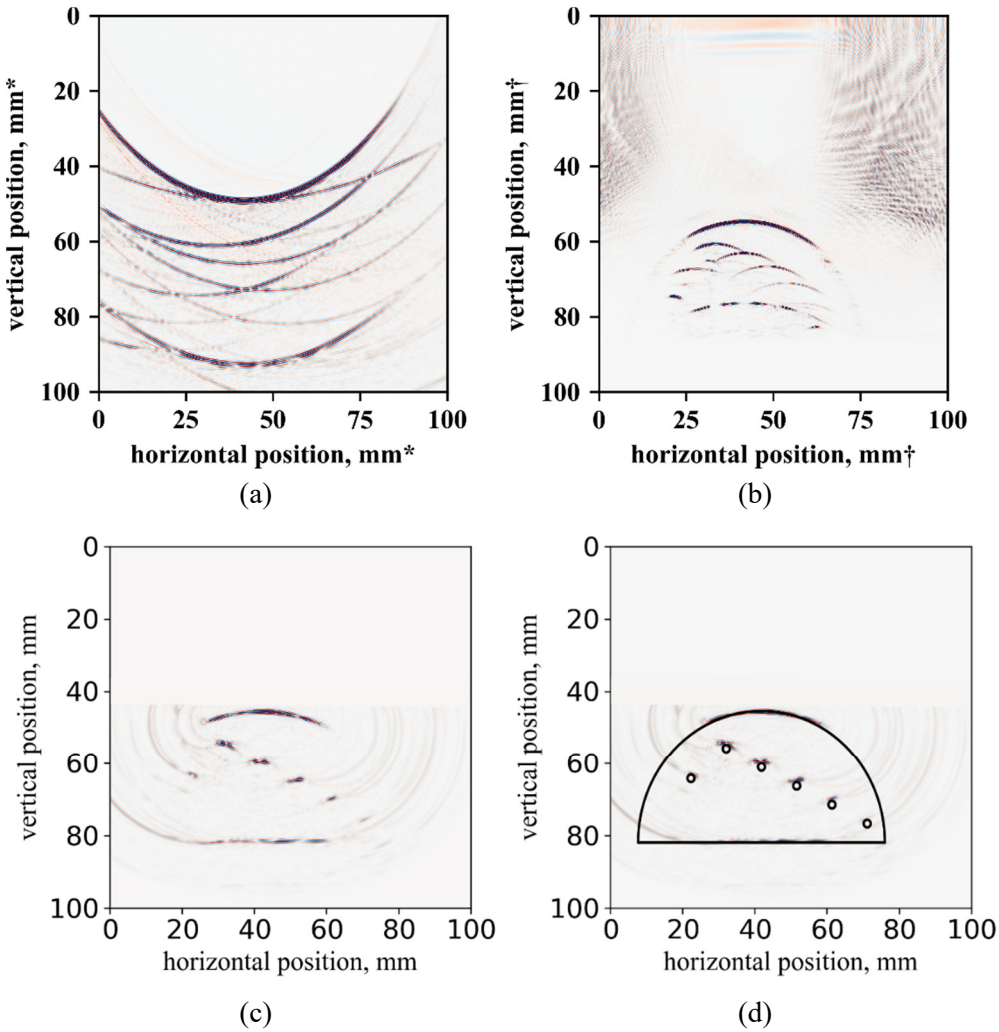

Figure 5.11 Object from Fig. 5.1b: (a) – TFM using c_1 sound speed (b) –TFM using c_2 speed of sound, (c) – the proposed methodology, (d) – the proposed methodology with overlay (position coordinates are calculated * – assuming that the environment is homogenous with C2 speed of sound, † – assuming that the environment has C1 speed of sound)

With the curved surface method reconstruction of defects, although without the model CAD template, it is still more complicated to interpret the data due to the speckle noise.

As for the worst case scenario, the results can hardly be interpreted (due to the surface error and imperfectly accurate speed of sound), but the interpretation is still possible (see Fig. 5.12):

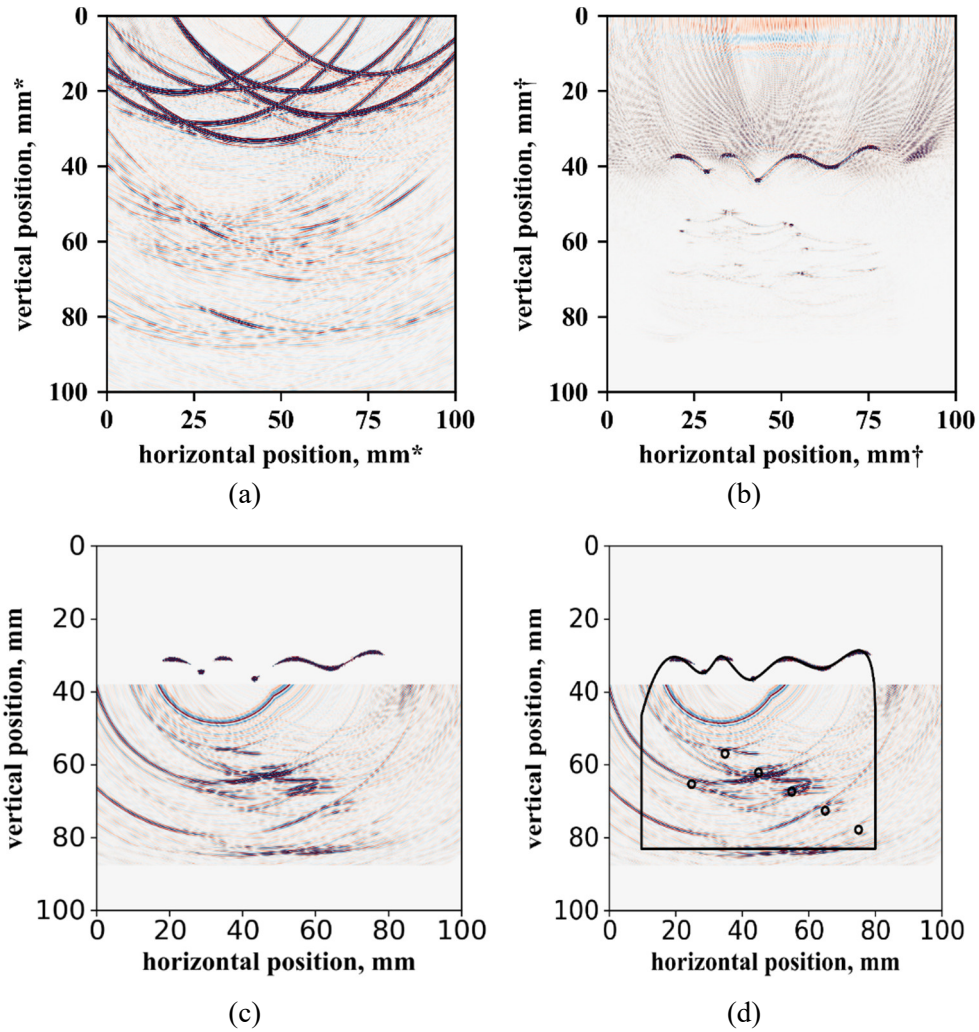

Figure 5.12 Object from Fig. 5.1b: (a) – TFM using c_1 speed of sound; (b) – TFM using c_2 speed of sound; (c) – the proposed methodology; (d) – the proposed methodology with overlay. We note that this figure involves huge number of artefacts (c) and (d) (position coordinates are calculated; * – assuming that the environment is homogenous with C2 speed of sound, † – assuming that the environment has C1 speed of sound)

From Figure 5.12c, it can be noted that the outline of the sample should be known, the focus data outside the sample can be treated as the speckle noise (algorithmic artifacts) and the reflections from the sample volume; the shear waves are not accounted for in this experiment. As for the error calculation, the accuracy is calculated by touching any parts of SDH in the model (as long as there is a signal in the defect area, it is assumed as the perfect match) and aligning them with the reconstructed signals.

The reconstruction error is increasing with the depth, which shows that the sound speed value was not accurate. The numerical errors are presented in Table 5.6:

Table 5.6 Reconstructed positions of defects

	Defect (SDH) position error from the CAD model, (Δx, Δy) mm					
Object	SDH1	SDH2	SDH3	SDH4	***SDH5***	SDH6
5.1a (5.10)	(-39.53, 20.80)	(-29.64, -15.63)	(-19.61, -10.42)	(-9.76, -5.21)	***(0,0)***	(9.85, -8.25)
5.1b (5.11)	(-37.30,-19.63)	(-27.65,-14.95)	(-19.34,-10.16)	(-10.41,-5.21)	***(0,0)***	(8.33,-7.17)
5.1c (5.12)	~	~	~	~	***(0,0)***	~

From Table 5.6, we see that the average margin of error is approximately 1 mm when using the proposed methodology (the error calculation methodology is the minimization mean square error using the CAD template). The same lateral resolution errors which cannot be removed without complicated shading are also seen, but, otherwise, the results provide accurate defect positions on irregular objects. As for the drawback, using imperfectly reconstructed data as in Fig. 5.1c object, the fact of the defect can be noted, but, due to low-level lateral resolution information, there is no definitive information on the position.

5.5 Practical application of the proposed methodology

The proposed methodology can be applied to various fields, where it is necessary to perform ultrasonic NDT inspection. One of the fields is the aircraft industry [2], the oil industry – oil rigs, heavy machinery industry, or other fields where the knowledge of defects is required.

On the other hand, another method can be used for the inspection, but the proposed methodology works only by using the ultrasonic phased array transducer and requires only the knowledge of the approximate speed of sound. If there is no knowledge of the speed of sound, it is difficult to recover the real positions where the method loses its purpose.

5.6 Conclusions from Chapter Five

1. The experimental setup demonstrated that the worst case surface reconstruction is possible with 0.6 mm accuracy when the information on the speed of sound is not perfect, although it still has influence on defectoscopy.
2. The proposed method demonstrated its feasibility and accuracy around 2 mm when using a phased array ultrasonic transducer while not possessing the perfect information on the speed of sound.
3. For the perfect reconstruction information, it is possible to register the presence of the defect and partial information on the position, which is not possible when using the total focusing method.

6 GENERAL CONCLUSIONS

1. Analysis of methods for the inspection of objects with complex surface morphology and volume reconstruction demonstrated that there are no straightforward algorithms to achieve reconstruction. As for the reflected signal interpretation, each method has its advantages and weaknesses as the methods can be divided into two groups by their reflection approximation assumption. Mainly, the investigated methods assume point size reflection with uncorrelated responses, and, when using a medium where the algebraic acoustic path calculation is possible, the values are easily calculated. Therefore, it is necessary to investigate the acoustic propagation in objects with a complex surface where the reflections are usually correlated.
2. After investigating the method for the surface morphology reconstruction, the developed method is based on TFM and uses FMC signal capturing. After TFM focusing, the data is interpreted by using a B-spline curve for low intensity reflection interpolation as, due to the complex nature of acoustic interactions, it is the least error-prone implementation, although if the surface can be approximated with the segment, an alternative approach can be proposed.
3. A method for 2D volume reconstruction for an object with complex geometry with a computer model has been created. The investigation shows that the acoustic path model uses analytic solution of Snell's law, although, for a more accurate model, Huygens principle needs to be used, particularly for the defects which are not perfectly aligned for Snell's law rays. A more accurate model is the α-shape based on Huygens principle propagation model. Although the method is iterative, its accuracy depends on the wave evolution time steps, and another point is that the number of emission circular wave fronts is used, which increases the error with the distance, and a higher impact in error stems from the speed of sound.
4. The numerical verification of the proposed method can be divided into two classes due to the limitation of computing resources. Initially, we used FEA analysis which provided the direct wavefront path in the numerical results, which demonstrated that the use of the proposed alpha shape algorithms is feasible. The second part of the numerical experiments with CIVA software yielded results that it is possible to achieve an accuracy level of 2mm.
5. Experimentally, the verification for object inspection and its inner structure reconstruction has been performed by using *Dasel Sitau* equipment. Our experiment shows that, with the use of the proposed methodology, it is possible to reconstruct the position of a defect in objects with a complex surface with 2 mm accuracy by using only the information on the speed of sound with relaxed lateral resolution requirements for extreme cases.

7 LIST OF THE PUBLICATIONS

Publications referred in Journals from the master list of Thomson Reuters Web of Science (with impact factor)

1. **Fyleris, Tautvydas**; Jasiūnienė, Elena. Comparative analysis of plane-wave imaging and the total focusing method in the reconstruction of complex geometrical surfaces // Surface topography: metrology and properties. Bristol: IOP Publishing. ISSN 2051-672X. eISSN 2051-672X. 2019, vol. 7, iss. 3, art. no. 035011, p. [1-9]. DOI: 10.1088/2051-672X/ab383d. [Science Citation Index Expanded (Web of Science); Scopus] [IF: 2.439; AIF: 3.562; IF/AIF: 0.684; Q2 (2018, InCites JCR SCIE)] [CiteScore: 2.88; SNIP: 1.731; SJR: 0.774; Q1 (2018, Scopus Sources)] [FOR: T 010 ; T 001] [Input: 0.500]

2. **Fyleris, Tautvydas**; Jasiūnienė, Elena. Analytic approach for 2D phased array delay law calculation in case of inspection of objects with complex geometry // Elektronika ir elektrotechnika = Electronics and electrical engineering. Kaunas: Technologija. ISSN 1392-1215. eISSN 2029-5731. 2019, vol. 25, iss. 2, p. 28-31. DOI: 10.5755/j01.eie.25.2.23200. [Science Citation Index Expanded (Web of Science); Scopus; Computers & Applied Sciences Complete] [IF: 0.684; AIF: 3.195; IF/AIF: 0.214; Q4 (2018, InCites JCR SCIE)] [CiteScore: 0.81; SNIP: 0.488; SJR: 0.182; Q3 (2018, Scopus Sources)] [FOR: T 001] [Input: 0.500]

Results of research presented in scientific conferences:

1. **Fyleris, Tautvydas**; Jasiūnienė, Elena. The development of ultrasonic adaptive method for inspection of objects with complex geometry: poster // Open readings 2019: 62nd international conference for students of physics and natural sciences, March 19-22, Vilnius, Lithuania: abstract book. Vilnius: Vilnius University, 2019, P3-60. ISBN 9786090701379. p. 336. Internet access: http://www.openreadings.eu/thesismanager/thesis19/P3-60.pdf [accessed on March 28, 2019].

2. **Fyleris, Tautvydas**; Jasiūnienė, Elena. Analytic approach for 2D phased array delay law calculation in case of inspection of objects with complex geometry // Elektronika ir elektrotechnika = Electronics and electrical engineering. Kaunas // The 22nd International Conference Electronics 2018. Palanga

8 REFERENCES

[1] G.-R. Gillich and Z.-I. Praisach, “Modal identification and damage detection in beam-like structures using the power spectrum and time–frequency analysis,” *Signal Processing*, vol. 96, pp. 29–44, Mar. 2014, doi: 10.1016/j.sigpro.2013.04.027.

[2] A. Katunin, K. Dragan, and M. Dziendzikowski, “Damage identification in aircraft composite structures: A case study using various non-destructive testing techniques,” *Composite Structures*, vol. 127, pp. 1–9, Sep. 2015, doi: 10.1016/j.compstruct.2015.02.080.

[3] *Fundamentals of ultrasonic nondestructive evaluation*. New York, NY: Springer Science+Business Media, 2016.

[4] S. J. Davies, C. Edwards, G. S. Taylor, and S. B. Palmer, “Laser-generated ultrasound: its properties, mechanisms and multifarious applications,” *J. Phys. D: Appl. Phys.*, vol. 26, no. 3, p. 329, 1993, doi: 10.1088/0022-3727/26/3/001.

[5] K. Mizutani, N. Wakatsuki, and T. Ebihara, “Introduction of measurement techniques in ultrasonic electronics: Basic principles and recent trends,” *Japanese Journal of Applied Physics*, vol. 55, no. 7S1, p. 07KA02, Jul. 2016, doi: 10.7567/JJAP.55.07KA02.

[6] S. Okada, O. Nakamura, and Y. Esaki, “Development and commercialization of laser inspection system to detect surface flaws of machined holes,” p. 13, 2018.

[7] X. Dong, C. J. Taylor, and T. F. Cootes, “Automatic Inspection of Aerospace Welds Using X-Ray Images,” in *2018 24th International Conference on Pattern Recognition (ICPR)*, Beijing, Aug. 2018, pp. 2002–2007, doi: 10.1109/ICPR.2018.8545738.

[8] M. Kageyama *et al.*, “X-ray phase-imaging scanner with tiled bent gratings for large-field-of-view nondestructive testing,” *NDT & E International*, vol. 105, pp. 19–24, Jul. 2019, doi: 10.1016/j.ndteint.2019.04.007.

[9] T. E. García, B. Arroyo, C. Rodríguez, F. J. Belzunce, and J. A. Álvarez, “Small punch test methodologies for the analysis of the hydrogen embrittlement of structural steels,” *Theoretical and Applied Fracture Mechanics*, vol. 86, pp. 89–100, Dec. 2016, doi: 10.1016/j.tafmec.2016.09.005.

[10] S. Le Roux, M. Salem, and A. Hor, “Improvement of the bridge curvature method to assess residual stresses in selective laser melting,” *Additive Manufacturing*, vol. 22, pp. 320–329, Aug. 2018, doi: 10.1016/j.addma.2018.05.025.

[11] R. Coray, M. Zeltner, and M. Özcan, “Fracture strength of implant abutments after fatigue testing: A systematic review and a meta-analysis,” *Journal of the Mechanical Behavior of Biomedical Materials*, vol. 62, pp. 333–346, Sep. 2016, doi: 10.1016/j.jmbbm.2016.05.011.

[12] D. Liu and P. E. J. Flewitt, “Deformation and fracture of carbonaceous materials using in situ micro-mechanical testing,” *Carbon*, vol. 114, pp. 261–274, Apr. 2017, doi: 10.1016/j.carbon.2016.11.084.

[13] R. Madjitey, H. Thomson, C. M. E. Simpson, D. M. Frigo, and G. M. Graham, “Corrosion Testing in Moderate and Ultra High Shear Production Environments,” in *SPE International Oilfield Corrosion Conference and Exhibition*, Aberdeen, Scotland, UK, 2018, doi: 10.2118/190906-MS.

[14] T. D. Rossing, Ed., *Springer handbook of acoustics*. New York, N.Y: Springer, 2007.

[15] N. Ida and N. Meyendorf, *Handbook of advanced nondestructive evaluation*. 2019.

[16] A. G. J. Besson, “Imaging from Echoes: On Inverse Problems in Ultrasound,” p. 236.

[17] M. Fink, Ed., *Imaging of complex media with acoustic and seismic waves*. Berlin; New York: Springer, 2002.

[18] W. Du, Y. Zhao, R. Roy, S. Addepalli, and L. Tinsley, “A review of miniaturised Non-Destructive Testing technologies for in-situ inspections,” *Procedia Manufacturing*, vol. 16, pp. 16–23, 2018, doi: 10.1016/j.promfg.2018.10.152.

[19] W. Harara and A. Altahan, “Attempt Towards the Replacement of Radiography with Phased Array Ultrasonic Testing of Steel Plate Welded Joints Performed on Bridges and Other Applications,” *Russ J Nondestruct Test*, vol. 54, no. 5, pp. 335–344, May 2018, doi: 10.1134/S1061830918050054.

[20] B. Byram, “Aperture Domain Model Image REconstruction (ADMIRE) for improved ultrasound imaging,” in *2017 IEEE International Conference on Acoustics, Speech and Signal Processing (ICASSP)*, New Orleans, LA, Mar. 2017, pp. 6250–6253, doi: 10.1109/ICASSP.2017.7953358.

[21] M. Zielińska and M. Rucka, “Non-Destructive Assessment of Masonry Pillars using Ultrasonic Tomography,” *Materials*, vol. 11, no. 12, p. 2543, Dec. 2018, doi: 10.3390/ma11122543.

[22] M. Pérez-Liva, J. L. Herraiz, J. M. Udías, E. Miller, B. T. Cox, and B. E. Treeby, “Time domain reconstruction of sound speed and attenuation in ultrasound computed tomography using full wave inversion,” *The Journal of the Acoustical Society of America*, vol. 141, no. 3, pp. 1595–1604, Mar. 2017, doi: 10.1121/1.4976688.

[23] J. A. Brown and G. R. Lockwood, “Low-cost, high-performance pulse generator for ultrasound imaging,” *IEEE Transactions on Ultrasonics, Ferroelectrics, and Frequency Control*, vol. 49, no. 6, pp. 848–851, Jun. 2002, doi: 10.1109/TUFFC.2002.1009345.

[24] H. Peng, J. Sabate, and K. Wall, “High frequency GaN-based ultrasound pulse generator for high energy delivery,” in *2017 IEEE Applied Power Electronics Conference and Exposition (APEC)*, Mar. 2017, pp. 1652–1658, doi: 10.1109/APEC.2017.7930921.

[25] L. Svilainis, A. Chaziachmetovas, and V. Dumbrava, “Half bridge topology 500V pulser for ultrasonic transducer excitation,” *Ultrasonics*, vol. 59, pp. 79–85, May 2015, doi: 10.1016/j.ultras.2015.01.014.

[26] J. M. G. Borsboom, C. T. Chin, A. Bouakaz, M. Versluis, and N. de Jong, “Harmonic chirp imaging method for ultrasound contrast agent,” *IEEE Transactions on Ultrasonics, Ferroelectrics, and Frequency Control*, vol. 52, no. 2, pp. 241–249, Feb. 2005, doi: 10.1109/TUFFC.2005.1406550.

[27] S. Harput, J. McLaughlan, D. M. J. Cowell, and S. Freear, “Superharmonic imaging with chirp coded excitation: filtering spectrally overlapped harmonics,” *IEEE Transactions on Ultrasonics, Ferroelectrics, and Frequency Control*, vol. 61, no. 11, pp. 1802–1814, Nov. 2014, doi: 10.1109/TUFFC.2014.006424.

[28] C. P. Karunakaran and M. L. Oelze, “Amplitude modulated chirp excitation to reduce grating lobes and maintain ultrasound intensity at the focus of an array,” *Ultrasonics*, vol. 53, no. 7, pp. 1293–1303, Sep. 2013, doi: 10.1016/j.ultras.2013.03.014.

[29] J.-F. Cardoso and A. Souloumiac, “Blind beamforming for non-Gaussian signals,” in *IEE proceedings F (radar and signal processing)*, 1993, vol. 140, pp. 362–370.

[30] L. Demi, J. Viti, L. Kusters, F. Guidi, P. Tortoli, and M. Mischi, “Implementation of parallel transmit beamforming using orthogonal frequency division multiplexing-achievable resolution and interbeam interference,” *IEEE Transactions on Ultrasonics, Ferroelectrics, and Frequency Control*, vol. 60, no. 11, pp. 2310–2320, Nov. 2013, doi: 10.1109/TUFFC.2013.6644735.

[31] P. Gong, P. Song, and S. Chen, “Ultrafast Synthetic Transmit Aperture Imaging Using Hadamard-Encoded Virtual Sources With Overlapping Sub-Apertures,” *IEEE Transactions on Medical Imaging*, vol. 36, no. 6, pp. 1372–1381, Jun. 2017, doi: 10.1109/TMI.2017.2687400.

[32] M. Inerfield, G. R. Lockwood, and S. L. Garverick, “A sigma-delta-based sparse synthetic aperture beamformer for real-time 3-D ultrasound,” *IEEE Transactions on Ultrasonics, Ferroelectrics, and Frequency Control*, vol. 49, no. 2, pp. 243–254, Feb. 2002, doi: 10.1109/58.985708.

[33] G. Matrone, A. Ramalli, A. S. Savoia, P. Tortoli, and G. Magenes, “High Frame-Rate, High Resolution Ultrasound Imaging With Multi-Line Transmission and Filtered-Delay Multiply And Sum Beamforming,” *IEEE Transactions on Medical Imaging*, vol. 36, no. 2, pp. 478–486, Feb. 2017, doi: 10.1109/TMI.2016.2615069.

[34] R. Y. Chiao and Xiaohui Hao, “Coded excitation for diagnostic ultrasound: a system developer’s perspective,” *IEEE Trans. Ultrason., Ferroelect., Freq. Contr.*, vol. 52, no. 2, pp. 160–170, Feb. 2005, doi: 10.1109/TUFFC.2005.1406543.

[35] “M2M Gekko®,” [Online]. Available: https://eddyfi.com/doc/Downloadables/201906_M2M-GEKKO-specifications-sheet_A4-01.pdf.

[36] “SITAU MX FP,” [Online]. Available: http://www.daselsistemas.com/en/products/phasedarray/full-parallel.

[37] “OmniScan MX2,” [Online]. Available: https://www.olympus-ims.com/ru/omniscan-mx2/.

[38] J. F. Cruza and J. Camacho, “Total Focusing Method With Virtual Sources in the Presence of Unknown Geometry Interfaces,” *IEEE Transactions on Ultrasonics, Ferroelectrics, and Frequency Control*, vol. 63, no. 10, pp. 1581–1592, Oct. 2016, doi: 10.1109/TUFFC.2016.2593439.

[39] C. Holmes, B. Drinkwater, and P. Wilcox, “The post-processing of ultrasonic array data using the total focusing method,” *Insight - Non-Destructive Testing and Condition Monitoring*, vol. 46, no. 11, pp. 677–680, Nov. 2004, doi: 10.1784/insi.46.11.677.52285.

[40] A. J. Hunter, B. W. Drinkwater, and P. D. Wilcox, “The wavenumber algorithm for full-matrix imaging using an ultrasonic array,” *IEEE Transactions on Ultrasonics, Ferroelectrics, and Frequency Control*, vol. 55, no. 11, pp. 2450–2462, Nov. 2008, doi: 10.1109/TUFFC.952.

[41] E. A. Marengo, F. K. Gruber, and F. Simonetti, “Time-Reversal MUSIC Imaging of Extended Targets,” *IEEE Transactions on Image Processing*, vol. 16, no. 8, pp. 1967–1984, Aug. 2007, doi: 10.1109/TIP.2007.899193.

[42] M. Mozaffarzadeh, A. Mahloojifar, and M. Orooji, “Medical photoacoustic beamforming using minimum variance-based delay multiply and sum,” in *Digital Optical Technologies 2017*, 2017, vol. 10335, p. 1033522.

[43] “Eigenspace-based minimum variance beamforming applied to medical ultrasound imaging - IEEE Journals & Magazine.” http://ieeexplore.ieee.org/document/5611687/#full-text-section (accessed Mar. 05, 2018).

[44] D. L. Hopkins, M. Brassard, G. A. Neau, J.-N. Noiret, W. V. Johnson, and L. Le Ber, “Surface-Adaptive Ultrasound (SAUL) for phased-array inspection of composite specimens with curved edges and complex geometry,” *AIP Conference Proceedings*, vol. 1511, no. 1, pp. 809–816, Jan. 2013, doi: 10.1063/1.4789128.

[45] M. Sutcliffe, M. Weston, P. Charlton, K. Donne, B. Wright, and I. Cooper, “Full matrix capture with time-efficient auto-focusing of unknown geometry through dual-layered media,” *Insight - Non-Destructive Testing and Condition Monitoring*, vol. 55, no. 6, pp. 297–301, Jun. 2013, doi: 10.1784/insi.2012.55.6.297.

[46] M. Weston, P. Mudge, C. Davis, and A. Peyton, “Time efficient auto-focussing algorithms for ultrasonic inspection of dual-layered media using Full Matrix Capture,” *NDT & E International*, vol. 47, pp. 43–50, Apr. 2012, doi: 10.1016/j.ndteint.2011.10.006.

[47] A. J. Devaney, E. A. Marengo, and F. K. Gruber, “Time-reversal-based imaging and inverse scattering of multiply scattering point targets,” *The Journal of the Acoustical Society of America*, vol. 118, no. 5, pp. 3129–3138, Nov. 2005, doi: 10.1121/1.2042987.

[48] C. Fan, M. Pan, F. Luo, and B. W. Drinkwater, “Multi-frequency time-reversal-based imaging for ultrasonic nondestructive evaluation using full matrix capture,” *IEEE Transactions on Ultrasonics, Ferroelectrics, and Frequency Control*, vol. 61, no. 12, pp. 2067–2074, Dec. 2014, doi: 10.1109/TUFFC.2014.006574.

[49] M. Fink, “Time reversal of ultrasonic fields. I. Basic principles,” *IEEE Transactions on Ultrasonics, Ferroelectrics, and Frequency Control*, vol. 39, no. 5, pp. 555–566, Sep. 1992, doi: 10.1109/58.156174.

[50] C. Prada, J. Thomas, and M. Fink, “The iterative time reversal process: Analysis of the convergence,” *The Journal of the Acoustical Society of America*, vol. 97, no. 1, pp. 62–71, Jan. 1995, doi: 10.1121/1.412285.

[51] B. M. Asl and A. M. Deylami, “A low complexity minimum variance beamformer for ultrasound imaging using dominant mode rejection,” *Ultrasonics*, vol. 85, pp. 49–60, Apr. 2018, doi: 10.1016/j.ultras.2017.12.012.

[52] R. G. Lorenz and S. P. Boyd, “Robust minimum variance beamforming,” *IEEE Transactions on Signal Processing*, vol. 53, no. 5, pp. 1684–1696, May 2005, doi: 10.1109/TSP.2005.845436.

[53] M. Mozaffarzadeh, A. Mahloojifar, M. Nasiriavanaki, and M. Orooji, “Eigenspace-based minimum variance adaptive beamformer combined with delay multiply and sum: experimental study,” in *Photonics in Dermatology and Plastic Surgery 2018*, 2018, vol. 10467, p. 1046717.

[54] M. Sutcliffe, P. Charlton, M. Weston, and S. Mosey, “Virtual source aperture imaging and calibration for ultrasonic inspections through dual-layered media for non-destructive testing,” *Insight - Non-Destructive Testing and Condition Monitoring*, vol. 59, no. 11, pp. 596–602, Nov. 2017, doi: 10.1784/insi.2017.59.11.596.

[55] P. S. Lowe, T. Scholehwar, J. Yau, J. Kanfoud, T. H. Gan, and C. Selcuk, “Flexible Shear Mode Transducer for Structural Health Monitoring using Ultrasonic Guided Waves,” *IEEE Transactions on Industrial Informatics*, vol. PP, no. 99, pp. 1–1, 2017, doi: 10.1109/TII.2017.2775343.

[56] K. Nakahata, S. Tokumasu, A. Sakai, Y. Iwata, K. Ohira, and Y. Ogura, “Ultrasonic imaging using signal post-processing for a flexible array transducer,” *NDT & E International*, vol. 82, pp. 13–25, Sep. 2016, doi: 10.1016/j.ndteint.2016.04.002.

[57] T. C. Wu, M. Kobayashi, M. Tanabe, and C. H. Yang, “The Use of Flexible Ultrasound Transducers for the Detection of Laser-Induced Guided Waves on Curved Surfaces at Elevated Temperatures,” *Sensors*, vol. 17, no. 6, p. 1285, Jun. 2017, doi: 10.3390/s17061285.

[58] S.-C. Wooh and Y. Shi, “Optimum beam steering of linear phased arrays,” *Wave Motion*, vol. 29, no. 3, pp. 245–265, Apr. 1999, doi: 10.1016/S0165-2125(98)00039-0.

[59] R. Bamler, “A comparison of range-Doppler and wavenumber domain SAR focusing algorithms,” *IEEE Transactions on Geoscience and Remote Sensing*, vol. 30, no. 4, pp. 706–713, Jul. 1992, doi: 10.1109/36.158864.

[60] C. Fan, M. Caleap, M. Pan, and B. W. Drinkwater, “A comparison between ultrasonic array beamforming and super resolution imaging algorithms for non-destructive evaluation,” *Ultrasonics*, vol. 54, no. 7, pp. 1842–1850, Sep. 2014, doi: 10.1016/j.ultras.2013.12.012.

[61] L.-J. Gelius and E. Asgedom, “Diffraction-limited imaging and beyond - the concept of super resolution‡: Diffraction-limited imaging and beyond,” *Geophysical Prospecting*, vol. 59, no. 3, pp. 400–421, May 2011, doi: 10.1111/j.1365-2478.2010.00928.x.

[62] D. Garcia, L. L. Tarnec, S. Muth, E. Montagnon, J. Porée, and G. Cloutier, “Stolt’s f-k migration for plane wave ultrasound imaging,” *IEEE Transactions on Ultrasonics, Ferroelectrics, and Frequency Control*, vol. 60, no. 9, pp. 1853–1867, Sep. 2013, doi: 10.1109/TUFFC.2013.2771.

[63] P. Gupta and S. P. Kar, “MUSIC and improved MUSIC algorithm to estimate direction of arrival,” in *2015 International Conference on Communications and Signal Processing (ICCSP)*, Apr. 2015, pp. 0757–0761, doi: 10.1109/ICCSP.2015.7322593.

[64] E. A. Marengo and F. K. Gruber, “Subspace-Based Localization and Inverse Scattering of Multiple Scattering Point Targets,” *EURASIP Journal on Advances in Signal Processing*, vol. 2007, no. 1, Dec. 2006, doi: 10.1155/2007/17342.

[65] M. Fink, G. Montaldo, and M. Tanter, “Time reversal acoustics,” in *IEEE Ultrasonics Symposium, 2004*, Aug. 2004, vol. 2, pp. 850-859 Vol.2, doi: 10.1109/ULTSYM.2004.1417870.

[66] P. Sava and B. Biondi, “Wave-equation migration velocity analysis. I. Theory,” *Geophysical Prospecting*, vol. 52, no. 6, pp. 593–606, doi: 10.1111/j.1365-2478.2004.00447.x.

[67] F. Reverdy and G. Benoist, “Advantages and Complementarity of Phased-Array Technology and Total Focusing Method,” p. 8.

[68] J. Camacho, J. F. Cruza, C. Fritsch, and J. M. Moreno, “Automatic dynamic depth focusing for NDT,” presented at the 40th Annual Review of Progress in Quantitative Nondestructive

Evaluation: Incorporating the 10th International Conference on Barkhausen Noise and Micromagnetic Testing, Baltimore, Maryland, USA, 2014, pp. 57–64, doi: 10.1063/1.4864802.

[69] O. Nowers, D. J. Duxbury, and B. W. Drinkwater, "Ultrasonic array imaging through an anisotropic austenitic steel weld using an efficient ray-tracing algorithm," *NDT & E International*, vol. 79, pp. 98–108, Apr. 2016, doi: 10.1016/j.ndteint.2015.12.009.

[70] S. R. Doctor, T. E. Hall, and L. D. Reid, "SAFT — the evolution of a signal processing technology for ultrasonic testing," *NDT International*, vol. 19, no. 3, pp. 163–167, Jun. 1986, doi: 10.1016/0308-9126(86)90105-7.

[71] B. Lam, M. Price, and A. P. Chandrakasan, "An ASIC for Energy-Scalable, Low-Power Digital Ultrasound Beamforming," in *2016 IEEE International Workshop on Signal Processing Systems (SiPS)*, Oct. 2016, pp. 57–62, doi: 10.1109/SiPS.2016.18.

[72] N. Quaegebeur and P. Masson, "Correlation-based imaging technique using ultrasonic transmit-receive array for Non-Destructive Evaluation," *Ultrasonics*, vol. 52, no. 8, pp. 1056–1064, Dec. 2012, doi: 10.1016/j.ultras.2012.08.017.

[73] Y. H. Hu and S.-Y. Kung, "Systolic Arrays," in *Handbook of Signal Processing Systems*, S. S. Bhattacharyya, E. F. Deprettere, R. Leupers, and J. Takala, Eds. Cham: Springer International Publishing, 2019, pp. 939–977.

[74] T. G. Rochow and P. A. Tucker, *Introduction to Microscopy by Means of Light, Electrons, X Rays, or Acoustics*. Boston, MA: Springer US, 1994.

[75] Y. Humeida, P. D. Wilcox, M. D. Todd, and B. W. Drinkwater, "A probabilistic approach for the optimisation of ultrasonic array inspection techniques," *NDT & E International*, vol. 68, pp. 43–52, Dec. 2014, doi: 10.1016/j.ndteint.2014.07.007.

[76] J. Jang and J. Chang, "Design and Fabrication of Double-Focused Ultrasound Transducers to Achieve Tight Focusing," *Sensors*, vol. 16, no. 8, p. 1248, Aug. 2016, doi: 10.3390/s16081248.

[77] J. A. Jensen and N. B. Svendsen, "Calculation of pressure fields from arbitrarily shaped, apodized, and excited ultrasound transducers," *IEEE Transactions on Ultrasonics, Ferroelectrics, and Frequency Control*, vol. 39, no. 2, pp. 262–267, Mar. 1992, doi: 10.1109/58.139123.

[78] T. S. Jerome, Y. A. Ilinskii, E. A. Zabolotskaya, and M. F. Hamilton, "Born approximation of acoustic radiation force and torque on soft objects of arbitrary shape," *The Journal of the Acoustical Society of America*, vol. 145, no. 1, pp. 36–44, Jan. 2019, doi: 10.1121/1.5084045.

[79] M. Fazlyyyakhmatov, "Radiation Pattern of Ultrasonic Transducer with Polymer-Powder Matching Layer," in *2018 19th International Conference of Young Specialists on Micro/Nanotechnologies and Electron Devices (EDM)*, Erlagol, Jun. 2018, pp. 363–366, doi: 10.1109/EDM.2018.8434934.

[80] S. Holm, "Bessel and conical beams and approximation with annular arrays," *IEEE Trans. Ultrason., Ferroelect., Freq. Contr.*, vol. 45, no. 3, pp. 712–718, May 1998, doi: 10.1109/58.677615.

[81] V. K. Chillara, E. S. Davis, C. Pantea, and D. N. Sinha, "Ultrasonic Bessel beam generation from radial modes of piezoelectric discs," *Ultrasonics*, vol. 96, pp. 140–148, Jul. 2019, doi: 10.1016/j.ultras.2019.02.002.

[82] J. A. Jensen, "A multi-threaded version of Field II," in *2014 IEEE International Ultrasonics Symposium*, Chicago, IL, USA, Sep. 2014, pp. 2229–2232, doi: 10.1109/ULTSYM.2014.0555.

[83] S. R. Kolkoori, P. Shokouhi, C. Hoehne, M.-U. Rahman, M. Kreutzbruck, and J. Prager, "A comparative study of ray tracing and CIVA simulation for ultrasonic examination of anisotropic inhomogeneous austenitic welds," *AIP Conference Proceedings*, vol. 1511, no. 1, pp. 1043–1050, Jan. 2013, doi: 10.1063/1.4789158.

[84] T. Kundu, D. Placko, E. K. Rahani, T. Yanagita, and Cac Minh Dao, "Ultrasonic field modeling: a comparison of analytical, semi-analytical, and numerical techniques," *IEEE Transactions on Ultrasonics, Ferroelectrics and Frequency Control*, vol. 57, no. 12, pp. 2795–2807, Dec. 2010, doi: 10.1109/TUFFC.2010.1753.

[85] W. Kuperman and P. Roux, “Underwater Acoustics,” in *Springer Handbook of Acoustics*, T. D. Rossing, Ed. New York, NY: Springer New York, 2007, pp. 149–204.

[86] P. D. Wilcox and J. Zhang, “Quantification of the Effect of Array Element Pitch on Imaging Performance,” *IEEE Transactions on Ultrasonics, Ferroelectrics, and Frequency Control*, vol. PP, no. 99, pp. 1–1, 2018, doi: 10.1109/TUFFC.2018.2794627.

[87] G. Ameri, J. S. H. Baxter, A. J. McLeod, T. M. Peters, and E. C. S. Chen, “Effects of line fiducial parameters and beamforming on ultrasound calibration,” *JMI, JMIOBU*, vol. 4, no. 1, p. 015002, Feb. 2017, doi: 10.1117/1.JMI.4.1.015002.

[88] M. Ingram *et al.*, “Calibration of ultrasonic phased arrays for industrial applications,” in *IEEE SENSORS 2017*, Scottish Exhibition and Conference Centre, Oct. 2017, Accessed: Mar. 27, 2018. [Online]. Available: https://strathprints.strath.ac.uk/62383/.

[89] J. N. Potter, P. D. Wilcox, and A. J. Croxford, “Diffuse field full matrix capture for near surface ultrasonic imaging,” *Ultrasonics*, vol. 82, pp. 44–48, Jan. 2018, doi: 10.1016/j.ultras.2017.07.009.

[90] B. R. Mace and E. Manconi, “Modelling wave propagation in two-dimensional structures using finite element analysis,” *Journal of Sound and Vibration*, vol. 318, no. 4–5, pp. 884–902, Dec. 2008, doi: 10.1016/j.jsv.2008.04.039.

[91] “The Finite Element Method: Its Basis and Fundamentals - 6th Edition.” https://www.elsevier.com/books/the-finite-element-method-its-basis-and-fundamentals/zienkiewicz/978-0-08-047277-5 (accessed Mar. 29, 2018).

[92] J. Chen, “An efficient layered finite element method with domain decomposition for simulations of resistivity well logging,” *Journal of Petroleum Science and Engineering*, vol. 150, pp. 217–223, Feb. 2017, doi: 10.1016/j.petrol.2016.11.039.

[93] A. Rozanova, “The Khokhlov–Zabolotskaya–Kuznetsov equation,” *Comptes Rendus Mathematique*, vol. 344, no. 5, pp. 337–342, Mar. 2007, doi: 10.1016/j.crma.2007.01.010.

[94] B. E. Treeby, J. Jaros, A. P. Rendell, and B. T. Cox, “Modeling nonlinear ultrasound propagation in heterogeneous media with power law absorption using a k-space pseudospectral method,” *The Journal of the Acoustical Society of America*, vol. 131, no. 6, pp. 4324–4336, Jun. 2012, doi: 10.1121/1.4712021.

[95] X. Zhao, M. F. Hamilton, and R. J. McGough, “Simulations of nonlinear continuous wave pressure fields in FOCUS,” *AIP Conference Proceedings*, vol. 1821, no. 1, p. 080001, Mar. 2017, doi: 10.1063/1.4977631.

[96] B. E. Treeby and B. T. Cox, “k-Wave: MATLAB toolbox for the simulation and reconstruction of photoacoustic wave fields,” *JBO, JBOPFO*, vol. 15, no. 2, p. 021314, Mar. 2010, doi: 10.1117/1.3360308.

[97] J. Jaros, A. P. Rendell, and B. E. Treeby, “Full-wave nonlinear ultrasound simulation on distributed clusters with applications in high-intensity focused ultrasound,” *The International Journal of High Performance Computing Applications*, vol. 30, no. 2, pp. 137–155, May 2016, doi: 10.1177/1094342015581024.

[98] J. Jaros, A. P. Rendell, and B. E. Treeby, “Full-wave nonlinear ultrasound simulation on distributed clusters with applications in high-intensity focused ultrasound,” *arXiv:1408.4675 [physics]*, Aug. 2014, Accessed: Dec. 26, 2018. [Online]. Available: http://arxiv.org/abs/1408.4675.

[99] L. Aguilar, J. Wong, D. A. Steinman, and R. S. C. Cobbold, “FAMUS II: A Fast and Mechanistic Ultrasound Simulator Using an Impulse Response Approach,” *IEEE Transactions on Ultrasonics, Ferroelectrics, and Frequency Control*, vol. 64, no. 2, pp. 362–373, Feb. 2017, doi: 10.1109/TUFFC.2016.2632706.

[100] J. F. Cruza, J. Camacho, L. Serrano-Iribarnegaray, and C. Fritsch, “New method for real-time dynamic focusing through interfaces,” *IEEE Transactions on Ultrasonics, Ferroelectrics, and Frequency Control*, vol. 60, no. 4, pp. 739–751, Apr. 2013, doi: 10.1109/TUFFC.2013.2622.

[101] N. Gengembre and A. Lhémery, “Pencil method in elastodynamics: application to ultrasonic field computation,” *Ultrasonics*, vol. 38, no. 1, pp. 495–499, Mar. 2000, doi: 10.1016/S0041-624X(99)00068-2.

[102] H. Chouh, G. Rougeron, S. Chatillon, J. C. Iehl, J. P. Farrugia, and V. Ostromoukhov, “High performance ultrasonic field simulation on complex geometries,” *AIP Conference Proceedings*, vol. 1706, no. 1, p. 050002, Feb. 2016, doi: 10.1063/1.4940501.

[103] P. Calmon, A. Lhemery, and L. Paradis, “Modeling of ultrasonic fields and their interaction with defects,” in *1998 IEEE Ultrasonics Symposium. Proceedings (Cat. No. 98CH36102)*, 1998, vol. 1, pp. 779–783 vol.1, doi: 10.1109/ULTSYM.1998.762263.

[104] N. Gengembre, “Pencil method for ultrasonic beam computation,” p. 4, 2003.

[105] S. Tamano *et al.*, “Improvement of high-voltage staircase drive circuit waveform for high-intensity therapeutic ultrasound,” *Jpn. J. Appl. Phys.*, vol. 55, no. 7S1, p. 07KF17, Jun. 2016, doi: 10.7567/JJAP.55.07KF17.

[106] T. Harrison, A. Sampaleanu, and R. J. Zemp, “S-sequence spatially-encoded synthetic aperture ultrasound imaging [Correspondence],” *IEEE Transactions on Ultrasonics, Ferroelectrics, and Frequency Control*, vol. 61, no. 5, pp. 886–890, May 2014, doi: 10.1109/TUFFC.2014.2979.

[107] D. A. Kiefer, M. Fink, and S. J. Rupitsch, “Simultaneous Ultrasonic Measurement of Thickness and Speed of Sound in Elastic Plates Using Coded Excitation Signals,” *IEEE Transactions on Ultrasonics, Ferroelectrics, and Frequency Control*, vol. 64, no. 11, pp. 1744–1757, Nov. 2017, doi: 10.1109/TUFFC.2017.2746900.

[108] M. M. Betcke, B. T. Cox, N. Huynh, E. Z. Zhang, P. C. Beard, and S. R. Arridge, “Acoustic Wave Field Reconstruction From Compressed Measurements With Application in Photoacoustic Tomography,” *IEEE Transactions on Computational Imaging*, vol. 3, no. 4, pp. 710–721, Dec. 2017, doi: 10.1109/TCI.2017.2706029.

[109] E. Tiran *et al.*, “Multiplane wave imaging increases signal-to-noise ratio in ultrafast ultrasound imaging,” *Phys. Med. Biol.*, vol. 60, no. 21, p. 8549, 2015, doi: 10.1088/0031-9155/60/21/8549.

[110] T. Misaridis and J. A. Jensen, “Use of modulated excitation signals in medical ultrasound. Part III: high frame rate imaging,” *IEEE Transactions on Ultrasonics, Ferroelectrics, and Frequency Control*, vol. 52, no. 2, pp. 208–219, Feb. 2005, doi: 10.1109/TUFFC.2005.1406547.

[111] D. Ghisu, A. Gambero, M. Terenzi, G. Ricotti, A. Moroni, and S. Rossi, “180Vpp output voltage, 24MHz bandwidth, low power class AB current-feedback high voltage amplifier for ultrasound transmitters,” in *2018 IEEE Custom Integrated Circuits Conference (CICC)*, San Diego, CA, Apr. 2018, pp. 1–4, doi: 10.1109/CICC.2018.8357014.

[112] Weibao Qiu, Yanyan Yu, Fu Keung Tsang, and Lei Sun, “A multifunctional, reconfigurable pulse generator for high-frequency ultrasound imaging,” *IEEE Trans. Ultrason., Ferroelect., Freq. Contr.*, vol. 59, no. 7, pp. 1558–1567, Jul. 2012, doi: 10.1109/TUFFC.2012.2355.

[113] J.-X. Wu, Y.-C. Du, C.-H. Lin, P.-J. Chen, and T. Chen, “A novel bipolar pulse generator for high-frequency ultrasound system,” in *2013 IEEE International Ultrasonics Symposium (IUS)*, Jul. 2013, pp. 1571–1574, doi: 10.1109/ULTSYM.2013.0400.

[114] A. A. Assef, J. M. Maia, F. K. Schneider, E. T. Costa, and V. L. S. N. Button, “Design of a 128-channel FPGA-based ultrasound imaging beamformer for research activities,” in *2012 IEEE International Ultrasonics Symposium*, Dresden, Germany, Oct. 2012, pp. 635–638, doi: 10.1109/ULTSYM.2012.0158.

[115] B. Wang and J. Saniie, “Ultrasonic Signal Acquisition and Processing platform based on Zynq SoC,” in *2016 IEEE International Conference on Electro Information Technology (EIT)*, May 2016, pp. 0448–0451, doi: 10.1109/EIT.2016.7535282.

[116] “Analysis and Design of a High Voltage Integrated Class-B Amplifier for Ultra-Sound Transducers - IEEE Journals & Magazine.” http://ieeexplore.ieee.org/abstract/document/6731600/ (accessed Mar. 29, 2018).

[117] J. D. N. Cheeke, *Fundamentals and Applications of Ultrasonic Waves, Second Edition*. CRC Press, 2017.

[118] T. Fyleris and E. Jasiuniene, “Analytic Approach for 2D Phased Array Delay Law Calculation in Case of Inspection of Objects with Complex Geometry,” *Elektronika ir elektrotechnika*, vol. 25, no. 2, p. 4, 2019.

[119] A. J. Brath and F. Simonetti, “Phased Array Imaging of Complex-Geometry Composite Components,” *IEEE Transactions on Ultrasonics, Ferroelectrics, and Frequency Control*, vol. 64, no. 10, pp. 1573–1582, Oct. 2017, doi: 10.1109/TUFFC.2017.2726819.

[120] B. M. Asl and A. Mahloojifar, “Eigenspace-based minimum variance beamforming applied to medical ultrasound imaging,” *IEEE Transactions on Ultrasonics, Ferroelectrics, and Frequency Control*, vol. 57, no. 11, pp. 2381–2390, Nov. 2010, doi: 10.1109/TUFFC.2010.1706.

[121] K. Ranganathan and W. F. Walker, “A novel beamformer design method for medical ultrasound. Part I: Theory,” *IEEE Transactions on Ultrasonics, Ferroelectrics, and Frequency Control*, vol. 50, no. 1, pp. 15–24, Jan. 2003, doi: 10.1109/TUFFC.2003.1176522.

[122] K. E. Thomenius, “Evolution of ultrasound beamformers,” in *1996 IEEE Ultrasonics Symposium. Proceedings*, Nov. 1996, vol. 2, pp. 1615–1622 vol.2, doi: 10.1109/ULTSYM.1996.584398.

[123] D. Bera, J. G. Bosch, M. D. Verweij, N. de Jong, and H. J. Vos, “Dual stage beamforming in the absence of front-end receive focusing,” *Phys. Med. Biol.*, vol. 62, no. 16, p. 6631, 2017, doi: 10.1088/1361-6560/aa78df.

[124] G. Matrone, A. Ramalli, P. Tortoli, and G. Magenes, “Experimental evaluation of ultrasound higher-order harmonic imaging with Filtered-Delay Multiply And Sum (F-DMAS) non-linear beamforming,” *Ultrasonics*, vol. 86, pp. 59–68, May 2018, doi: 10.1016/j.ultras.2018.01.002.

[125] G. Matrone, A. S. Savoia, G. Caliano, and G. Magenes, “The Delay Multiply and Sum Beamforming Algorithm in Ultrasound B-Mode Medical Imaging,” *IEEE Transactions on Medical Imaging*, vol. 34, no. 4, pp. 940–949, Apr. 2015, doi: 10.1109/TMI.2014.2371235.

[126] G. Matrone, A. S. Savoia, G. Caliano, and G. Magenes, “Ultrasound plane-wave imaging with delay multiply and sum beamforming and coherent compounding,” in *2016 38th Annual International Conference of the IEEE Engineering in Medicine and Biology Society (EMBC)*, Aug. 2016, pp. 3223–3226, doi: 10.1109/EMBC.2016.7591415.

[127] M. Mozaffarzadeh, A. Mahloojifar, M. Orooji, S. Adabi, and M. Nasiriavanaki, “Double-Stage Delay Multiply and Sum Beamforming Algorithm: Application to Linear-Array Photoacoustic Imaging,” *IEEE Transactions on Biomedical Engineering*, vol. 65, no. 1, pp. 31–42, Jan. 2018, doi: 10.1109/TBME.2017.2690959.

[128] N. Laroche, E. Carcreff, S. Bourguignon, J. Idier, and A. Duclos, “An Inverse Approach for Ultrasonic Imaging by Total Focusing Point for Close Reflectors Separation,” in *2018 IEEE International Ultrasonics Symposium (IUS)*, Oct. 2018, pp. 1–4, doi: 10.1109/ULTSYM.2018.8580073.

[129] H. Hasegawa, “Apodized adaptive beamformer,” *J Med Ultrasonics*, vol. 44, no. 2, pp. 155–165, Apr. 2017, doi: 10.1007/s10396-016-0764-3.

[130] J. Wojcik, M. Lewandowski, and N. Żołek, “Grating lobes suppression by adding virtual receiving subaperture in synthetic aperture imaging,” *Ultrasonics*, vol. 76, pp. 125–135, Apr. 2017, doi: 10.1016/j.ultras.2016.12.013.

[131] S. Robert, O. Casula, O. Roy, and G. Neau, “Real-time nondestructive testing of composite aeronautical structures with a self-adaptive ultrasonic technique,” *Meas. Sci. Technol.*, vol. 24, no. 7, p. 074011, 2013, doi: 10.1088/0957-0233/24/7/074011.

[132] M. Fink, C. Prada, F. Wu, and D. Cassereau, “Self focusing in inhomogeneous media with time reversal acoustic mirrors,” in *Proceedings., IEEE Ultrasonics Symposium,* Oct. 1989, pp. 681–686 vol.2, doi: 10.1109/ULTSYM.1989.67072.

[133] G. F. Margrave and M. P. Lamoureux, “Elementary Migration Methods,” in *Numerical Methods of Exploration Seismology: With Algorithms in MATLAB®*, Cambridge University Press, 2019, pp. 351–434.

[134] F. Deng and F. L. Teixeira, “Locating small structural damages in pipes using space-frequency DORT processing,” *Results in Physics*, vol. 7, pp. 1637–1643, Jan. 2017, doi: 10.1016/j.rinp.2017.04.024.

[135] B. W. Drinkwater and P. D. Wilcox, “Ultrasonic arrays for non-destructive evaluation: A review,” *NDT & E International*, vol. 39, no. 7, pp. 525–541, Oct. 2006, doi: 10.1016/j.ndteint.2006.03.006.

[136] G. Dao, D. Braconnier, and M. Gruber, “Full-matrix capture with a customizable phased array instrument,” presented at the 41st Annual Review of Progress in Quantitative Nondestructive Evaluation: Volume 34, Boise, Idaho, 2015, pp. 1001–1006, doi: 10.1063/1.4914707.

[137] L. W. S. Jr, “Imaging with Phased Arrays - An Introduction,” in *Fundamentals of Ultrasonic Phased Arrays*, Springer, Cham, 2015, pp. 241–277.

[138] W. M. Brown and L. J. Porcello, “An introduction to synthetic-aperture radar,” *IEEE Spectrum*, vol. 6, no. 9, pp. 52–62, Sep. 1969, doi: 10.1109/MSPEC.1969.5213674.

[139] C. Chen, G. A. G. M. Hendriks, R. J. G. van Sloun, H. H. G. Hansen, and C. L. de Korte, “Improved Plane Wave Ultrasound Beamforming by Incorporating Angular Weighting and Coherent Compounding in Fourier Domain,” *IEEE Transactions on Ultrasonics, Ferroelectrics, and Frequency Control*, vol. PP, no. 99, pp. 1–1, 2018, doi: 10.1109/TUFFC.2018.2811865.

[140] T. Fyleris and E. Jasiūnienė, “Comparative analysis of plane-wave imaging and the total focusing method in the reconstruction of complex geometrical surfaces,” *Surf. Topogr.: Metrol. Prop.*, Aug. 2019, doi: 10.1088/2051-672X/ab383d.

[141] H. B. Lim, N. T. T. Nhung, E. P. Li, and N. D. Thang, “Confocal Microwave Imaging for Breast Cancer Detection: Delay-Multiply-and-Sum Image Reconstruction Algorithm,” *IEEE Transactions on Biomedical Engineering*, vol. 55, no. 6, pp. 1697–1704, Jun. 2008, doi: 10.1109/TBME.2008.919716.

[142] T. Su, D. Li, and S. Zhang, “An efficient subarray average delay multiply and sum beamformer algorithm in ultrasound imaging,” *Ultrasonics*, vol. 84, pp. 411–420, Mar. 2018, doi: 10.1016/j.ultras.2017.12.004.

[143] J. Capon, “High-resolution frequency-wavenumber spectrum analysis,” *Proceedings of the IEEE*, vol. 57, no. 8, pp. 1408–1418, Aug. 1969, doi: 10.1109/PROC.1969.7278.

[144] C. Camarero, “Simple, Fast and Practicable Algorithms for Cholesky, LU and QR Decomposition Using Fast Rectangular Matrix Multiplication,” *arXiv:1812.02056 [cs]*, Dec. 2018, Accessed: Apr. 04, 2019. [Online]. Available: http://arxiv.org/abs/1812.02056.

[145] K. Diamantis, A. Greenaway, T. Anderson, J. A. Jensen, and V. Sboros, “Experimental performance assessment of the sub-band minimum variance beamformer for ultrasound imaging,” *Ultrasonics*, vol. 79, pp. 87–95, Aug. 2017, doi: 10.1016/j.ultras.2017.04.011.

[146] M. Mozaffarzadeh, A. Mahloojifar, M. Orooji, K. Kratkiewicz, S. Adabi, and M. Nasiriavanaki, “Linear-array photoacoustic imaging using minimum variance-based delay multiply and sum adaptive beamforming algorithm,” *JBO, JBOPFO*, vol. 23, no. 2, p. 026002, Feb. 2018, doi: 10.1117/1.JBO.23.2.026002.

[147] J. F. Synnevag, A. Austeng, and S. Holm, “Adaptive Beamforming Applied to Medical Ultrasound Imaging,” *IEEE Transactions on Ultrasonics, Ferroelectrics, and Frequency Control*, vol. 54, no. 8, pp. 1606–1613, Aug. 2007, doi: 10.1109/TUFFC.2007.431.

[148] Zhisong Wang, Jian Li, and Renbiao Wu, “Time-delay- and time-reversal-based robust capon beamformers for ultrasound imaging,” *IEEE Transactions on Medical Imaging*, vol. 24, no. 10, pp. 1308–1322, Oct. 2005, doi: 10.1109/TMI.2005.857222.

[149] Jung-Lang Yu and Chien-Chung Yeh, “Generalized eigenspace-based beamformers,” *IEEE Transactions on Signal Processing*, vol. 43, no. 11, pp. 2453–2461, Nov. 1995, doi: 10.1109/78.482097.

[150] Carpenter Joel, Eggleton Benjamin J., and Schröder Jochen, “Comparison of principal modes and spatial eigenmodes in multimode optical fibre,” *Laser & Photonics Reviews*, vol. 11, no. 1, p. 1600259, Dec. 2016, doi: 10.1002/lpor.201600259.

[151] M. H. Heidari, M. Mozaffarzadeh, R. Manwar, and M. Nasiriavanaki, “Effects of important parameters variations on computing Eigenspace-based minimum variance weights for ultrasound tissue harmonic imaging,” in *Photons Plus Ultrasound: Imaging and Sensing 2018*, 2018, vol. 10494, p. 104946R.

[152] E. Moghimirad, C. A. V. Hoyos, A. Mahloojifar, B. M. Asl, and J. A. Jensen, “Synthetic Aperture Ultrasound Fourier Beamformation Using Virtual Sources,” *IEEE Transactions on Ultrasonics, Ferroelectrics, and Frequency Control*, vol. 63, no. 12, pp. 2018–2030, Dec. 2016, doi: 10.1109/TUFFC.2016.2606878.

[153] C. Bai, M. Ji, and M. Wan, “Fast adaptive beamforming combined with multiple apodization in ultrasound plane wave imaging,” in *2016 IEEE International Ultrasonics Symposium (IUS)*, Sep. 2016, pp. 1–3, doi: 10.1109/ULTSYM.2016.7728904.

[154] J. Reeg and M. L. Oelze, “Improving lateral resolution in ultrasonic Imaging by utilizing nulls in the beam pattern,” in *2015 IEEE International Ultrasonics Symposium (IUS)*, Oct. 2015, pp. 1–4, doi: 10.1109/ULTSYM.2015.0198.

[155] Chi Seo and Jesse Yen, “Sidelobe suppression in ultrasound imaging using dual apodization with cross-correlation,” *IEEE Transactions on Ultrasonics, Ferroelectrics and Frequency Control*, vol. 55, no. 10, pp. 2198–2210, Oct. 2008, doi: 10.1109/TUFFC.919.

[156] 14:00-17:00, “ISO 80000-3:2006,” *ISO*. http://www.iso.org/cms/render/live/en/sites/isoorg/contents/data/standard/03/18/31888.html (accessed Apr. 09, 2019).

[157] R. Stolt, “Migration by Fourier transform,” *Geophysics*, vol. 43, no. 1, pp. 23–48, Feb. 1978, doi: 10.1190/1.1440826.

[158] A. Sorna, X. Cheng, E. D’Azevedo, K. Won, and S. Tomov, “Optimizing the Fast Fourier Transform Using Mixed Precision on Tensor Core Hardware,” in *2018 IEEE 25th International Conference on High Performance Computing Workshops (HiPCW)*, Bengaluru, India, Dec. 2018, pp. 3–7, doi: 10.1109/HiPCW.2018.8634417.

[159] K.-S. Chen, “Generic Range–Doppler Algorithm,” in *Principles of Synthetic Aperture Radar Imaging*, 2015, pp. 91–98.

[160] K.-S. Chen, “Chirp Scaling Algorithm,” in *Principles of Synthetic Aperture Radar Imaging*, 2015, pp. 104–116.

[161] I. G. Cumming, “Interpretations of the Omega-K Algorithm and Comparisons with other Algorithms,” p. 4.

[162] M. H. Skjelvareid, T. Olofsson, Y. Birkelund, and Y. Larsen, “Synthetic aperture focusing of ultrasonic data from multilayered media using an omega-K algorithm,” *IEEE Transactions on Ultrasonics, Ferroelectrics, and Frequency Control*, vol. 58, no. 5, pp. 1037–1048, May 2011, doi: 10.1109/TUFFC.2011.1904.

[163] L. Merabet, S. Robert, and C. Prada, “2-D and 3-D Reconstruction Algorithms in the Fourier Domain for Plane-Wave Imaging in Nondestructive Testing,” *IEEE Trans. Ultrason., Ferroelect., Freq. Contr.*, vol. 66, no. 4, pp. 772–788, Apr. 2019, doi: 10.1109/TUFFC.2019.2895995.

[164] H. J. Callow, M. P. Hayes, and P. T. Gough, “Wavenumber domain reconstruction of SAR/SAS imagery using single transmitter and multiple-receiver geometry,” *Electronics Letters*, vol. 38, no. 7, pp. 336–338, Mar. 2002, doi: 10.1049/el:20020219.

[165] W. C. Chew, *Waves and fields in inhomogeneous media*. New York: IEEE Press, 1995.

[166] A. J. Hunter, B. W. Drinkwater, and P. D. Wilcox, “The wavenumber algorithm: fast fourier-domain imaging using full matrix capture,” *AIP Conference Proceedings*, vol. 1096, no. 1, pp. 856–863, Mar. 2009, doi: 10.1063/1.3114346.

[167] H. Jung, W. Kang, and K. Kim, “Multilayer Stolt Migration Algorithm for Subsurface Target Imaging in Oblique Layers,” *IEEE Journal of Selected Topics in Applied Earth Observations and Remote Sensing*, vol. 10, no. 10, pp. 4295–4303, Oct. 2017, doi: 10.1109/JSTARS.2016.2615867.

[168] N. Zhao, A. Basarab, D. Kouame, and J.-Y. Tourneret, “Joint Segmentation and Deconvolution of Ultrasound Images Using a Hierarchical Bayesian Model Based on Generalized Gaussian Priors,” *IEEE Transactions on Image Processing*, vol. 25, no. 8, pp. 3736–3750, Aug. 2016, doi: 10.1109/TIP.2016.2567074.

[169] R. Schmidt, “Multiple emitter location and signal parameter estimation,” *IEEE Transactions on Antennas and Propagation*, vol. 34, no. 3, pp. 276–280, Mar. 1986, doi: 10.1109/TAP.1986.1143830.

[170] Z. Hongmei, G. Zhenguo, and F. Huixuan, “A high resolution random linear sonar array based MUSIC method for underwater DOA estimation,” p. 4.

[171] Y. J. Huang, Y. W. Wang, F. J. Meng, and G. L. Wang, “A spatial spectrum estimation algorithm based on adaptive beamforming nulling,” in *2013 Fourth International Conference on Intelligent Control and Information Processing (ICICIP)*, Beijing, China, Jun. 2013, pp. 220–224, doi: 10.1109/ICICIP.2013.6568071.

[172] M. Ochmann, “Exact solution for the acoustical impulse response of a line source above an absorbing plane,” *The Journal of the Acoustical Society of America*, vol. 144, no. 3, pp. 1539–1549, Sep. 2018, doi: 10.1121/1.5054301.

[173] M. L. Diong, A. Roueff, P. Lasaygues, and A. Litman, “Impact of the Born approximation on the estimation error in 2D inverse scattering,” *Inverse Problems*, vol. 32, no. 6, p. 065006, Jun. 2016, doi: 10.1088/0266-5611/32/6/065006.

[174] T. S. Jerome, Y. A. Ilinskii, E. A. Zabolotskaya, and M. F. Hamilton, “Acoustic radiation force and torque on nonspherical scatterers in the Born approximation,” presented at the 21st International Symposium on Nonlinear Acoustics, Santa Fe, New Mexico, USA, 2018, p. 045013, doi: 10.1121/2.0000858.

[175] Y. Labyed and L. Huang, “Super-resolution ultrasound imaging using a phase-coherent MUSIC method with compensation for the phase response of transducer elements,” *IEEE Transactions on Ultrasonics, Ferroelectrics, and Frequency Control*, vol. 60, no. 6, pp. 1048–1060, Jun. 2013, doi: 10.1109/TUFFC.2013.2669.

[176] L. Le Jeune, S. Robert, P. Dumas, A. Membre, and C. Prada, “Adaptive ultrasonic imaging with the total focusing method for inspection of complex components immersed in water,” *AIP Conference Proceedings*, vol. 1650, no. 1, pp. 1037–1046, Mar. 2015, doi: 10.1063/1.4914712.

[177] C.-C. Shen, Y.-Q. Xing, and G. Jeng, “Autocorrelation-based generalized coherence factor for low-complexity adaptive beamforming,” *Ultrasonics*, vol. 72, pp. 177–183, Dec. 2016, doi: 10.1016/j.ultras.2016.07.015.

[178] M. H. H. Varnosfaderani, B. M. Asl, and S. Faridsoltani, “An Adaptive Synthetic Aperture Method Applied to Ultrasound Tissue Harmonic Imaging,” *IEEE Transactions on Ultrasonics, Ferroelectrics, and Frequency Control*, vol. PP, no. 99, pp. 1–1, 2018, doi: 10.1109/TUFFC.2018.2799870.

[179] S. A. Vorobyov, “Chapter 12 - Adaptive and Robust Beamforming*Dedicated to the memory of Professor Alex B. Gershman.*,” in *Academic Press Library in Signal Processing*, vol. 3, A. M. Zoubir, M. Viberg, R. Chellappa, and S. Theodoridis, Eds. Elsevier, 2014, pp. 503–552.

[180] E. S. Samundeeswari, “A Study on Multi-scale Approach for Despeckling Ultrasound Image,” *International Journal of Computer Applications*, p. 7.

[181] P. Perona and J. Malik, “Scale-space and edge detection using anisotropic diffusion,” *IEEE Transactions on Pattern Analysis and Machine Intelligence*, vol. 12, no. 7, pp. 629–639, Jul. 1990, doi: 10.1109/34.56205.

[182] F. Zhang, Y. M. Yoo, L. M. Koh, and Y. Kim, “Nonlinear Diffusion in Laplacian Pyramid Domain for Ultrasonic Speckle Reduction,” *IEEE Transactions on Medical Imaging*, vol. 26, no. 2, pp. 200–211, Feb. 2007, doi: 10.1109/TMI.2006.889735.

[183] P. Burt and E. Adelson, “The Laplacian Pyramid as a Compact Image Code,” *IEEE Transactions on Communications*, vol. 31, no. 4, pp. 532–540, Apr. 1983, doi: 10.1109/TCOM.1983.1095851.

[184] M. Mafi, H. Martin, M. Cabrerizo, J. Andrian, A. Barreto, and M. Adjouadi, “A comprehensive survey on impulse and Gaussian denoising filters for digital images,” *Signal Processing*, vol. 157, pp. 236–260, Apr. 2019, doi: 10.1016/j.sigpro.2018.12.006.

[185] Y. Yu and S. T. Acton, “Speckle reducing anisotropic diffusion,” *IEEE Transactions on Image Processing*, vol. 11, no. 11, pp. 1260–1270, Nov. 2002, doi: 10.1109/TIP.2002.804276.

[186] B. Wu, Y. Huang, and S. Krishnaswamy, “A Bayesian approach for sparse flaw detection from noisy signals for ultrasonic NDT,” *NDT & E International*, vol. 85, pp. 76–85, Jan. 2017, doi: 10.1016/j.ndteint.2016.10.005.

[187] D. China, P. Mitra, C. Chakraborty, and K. M. Mandana, “Wavelet based non local means filter for despeckling of intravascular ultrasound image,” in *2015 International Conference on Advances in Computing, Communications and Informatics (ICACCI)*, Aug. 2015, pp. 1361–1365, doi: 10.1109/ICACCI.2015.7275802.

[188] S. Finn, M. Glavin, and E. Jones, “Echocardiographic speckle reduction comparison,” *IEEE Transactions on Ultrasonics, Ferroelectrics, and Frequency Control*, vol. 58, no. 1, pp. 82–101, Jan. 2011, doi: 10.1109/TUFFC.2011.1776.

[189] D. Ghosh, D. Nandi, P. Ghosal, and A. Kumar, “A Novel Speckle Reducing Scan Conversion in Ultrasound Imaging System,” in *Progress in Intelligent Computing Techniques: Theory, Practice, and Applications*, Springer, Singapore, 2018, pp. 335–345.

[190] K. Krissian, C. F. Westin, R. Kikinis, and K. G. Vosburgh, “Oriented Speckle Reducing Anisotropic Diffusion,” *IEEE Transactions on Image Processing*, vol. 16, no. 5, pp. 1412–1424, May 2007, doi: 10.1109/TIP.2007.891803.

[191] S. V. Mohd Sagheer and S. N. George, “Ultrasound image despeckling using low rank matrix approximation approach,” *Biomedical Signal Processing and Control*, vol. 38, pp. 236–249, Sep. 2017, doi: 10.1016/j.bspc.2017.06.011.

[192] I. Galton and C. Weltin-Wu, “Understanding Phase Error and Jitter: Definitions, Implications, Simulations, and Measurement,” *IEEE Transactions on Circuits and Systems*, vol. 66, no. 1, p. 19, 2019.

[193] P. R. Smith, D. M. J. Cowell, B. Raiton, C. V. Ky, and S. Freear, “Ultrasound array transmitter architecture with high timing resolution using embedded phase-locked loops,” *IEEE Trans. Ultrason., Ferroelect., Freq. Contr.*, vol. 59, no. 1, pp. 40–49, Jan. 2012, doi: 10.1109/TUFFC.2012.2154.

[194] M. Unser, “Sampling - 50 Years After Shannon,” *Proceedings of the IEEE*, vol. 88, no. 4, p. 19, 2000.

[195] A. Papoulis, “Error analysis in sampling theory,” p. 9, 1966.

[196] M. Kröning, A. Bulavinov, K. M. Reddy, L. von Bernus, and D. Joneit, “Sampling phased array: a new technique for signal processing and ultrasonic imaging,” in *Nondestructive Characterization for Composite Materials, Aerospace Engineering, Civil Infrastructure, and Homeland Security 2007*, Apr. 2007, vol. 6531, p. 653119, doi: 10.1117/12.717891.

[197] C.-P. Jeannerod and S. M. Rump, “On relative errors of floating-point operations: Optimal bounds and applications,” *Mathematics of Computation*, vol. 87, no. 310, pp. 803–819, Jul. 2017, doi: 10.1090/mcom/3234.

[198] P. Panchekha, A. Sanchez-Stern, J. R. Wilcox, and Z. Tatlock, “Automatically improving accuracy for floating point expressions,” in *ACM SIGPLAN Notices*, 2015, vol. 50, pp. 1–11.

[199] L. L. Foldy, “The Multiple Scattering of Waves. I. General Theory of Isotropic Scattering by Randomly Distributed Scatterers,” *Phys. Rev.*, vol. 67, no. 3–4, pp. 107–119, Feb. 1945, doi: 10.1103/PhysRev.67.107.

[200] M. Lax, “Multiple Scattering of Waves,” *Rev. Mod. Phys.*, vol. 23, no. 4, pp. 287–310, Oct. 1951, doi: 10.1103/RevModPhys.23.287.

[201] M. H. Hafezi, R. Alebrahim, and T. Kundu, “Peri-ultrasound for modeling linear and nonlinear ultrasonic response,” *Ultrasonics*, vol. 80, pp. 47–57, Sep. 2017, doi: 10.1016/j.ultras.2017.04.015.

[202] K. Huang, P. Li, and H. Zhao, “An efficient algorithm for the generalized Foldy–Lax formulation,” *Journal of Computational Physics*, vol. 234, pp. 376–398, Feb. 2013, doi: 10.1016/j.jcp.2012.09.027.

[203] K. Huang, K. Solna, and H. Zhao, “Generalized Foldy-Lax formulation,” *Journal of Computational Physics*, vol. 229, no. 12, pp. 4544–4553, Jun. 2010, doi: 10.1016/j.jcp.2010.02.021.

[204] “An efficient algorithm for the generalized Foldy-Lax formulation - ScienceDirect.” https://www.sciencedirect.com/science/article/pii/S0021999112005724 (accessed Apr. 03, 2018).

[205] B. Kaltenbacher, “Mathematics of nonlinear acoustics,” *Evolution Equations & Control Theory2015, Volume 4, Pages 447-491*, Nov. 01, 2015. http://aimsciences.org/article/doi/10.3934/eect.2015.4.447 (accessed Apr. 09, 2018).

[206] T. L. Christiansen, M. F. Rasmussen, J. P. Bagge, L. N. Moesner, J. A. Jensen, and E. V. Thomsen, “3-D imaging using row???column-addressed arrays with integrated apodization??? part ii: transducer fabrication and experimental results,” *IEEE Transactions on Ultrasonics, Ferroelectrics, and Frequency Control*, vol. 62, no. 5, pp. 959–971, May 2015, doi: 10.1109/TUFFC.2014.006819.

[207] L. W. Schmerr, “An Ultrasonic System,” in *Fundamentals of Ultrasonic Nondestructive Evaluation*, Springer, Cham, 2016, pp. 1–13.

[208] R. Sharma, R. Agarwal, and A. Arora, “Evaluation of Ultrasonic Transducer with Divergent Membrane Materials and Geometries,” in *Smart Trends in Information Technology and Computer Communications*, Aug. 2016, pp. 779–787, doi: 10.1007/978-981-10-3433-6_93.

[209] M. A. Alsmirat, Y. Jararweh, M. Al-Ayyoub, M. A. Shehab, and B. B. Gupta, “Accelerating compute intensive medical imaging segmentation algorithms using hybrid CPU-GPU implementations,” *Multimedia Tools and Applications*, vol. 76, no. 3, pp. 3537–3555, Feb. 2017, doi: 10.1007/s11042-016-3884-2.

[210] S. Hong and H. Kim, “An Analytical Model for a GPU Architecture with Memory-level and Thread-level Parallelism Awareness,” p. 12.

[211] V. W. Lee *et al.*, “Debunking the 100X GPU vs. CPU Myth: An Evaluation of Throughput Computing on CPU and GPU,” p. 10.

[212] F. Li, Y. Ye, Z. Tian, and X. Zhang, “CPU versus GPU: which can perform matrix computation faster - performance comparison for basic linear algebra subprograms,” *Neural Computing and Applications*, Jan. 2018, doi: 10.1007/s00521-018-3354-z.

[213] S. Mittal and J. S. Vetter, “A Survey of CPU-GPU Heterogeneous Computing Techniques,” *ACM Computing Surveys*, vol. 47, no. 4, pp. 1–35, Jul. 2015, doi: 10.1145/2788396.

[214] A. Belouchrani, K. Abed-Meraim, J.-F. Cardoso, and E. Moulines, “A blind source separation technique using second-order statistics,” *IEEE Transactions on signal processing*, vol. 45, no. 2, pp. 434–444, 1997.

[215] G. Montaldo, M. Tanter, J. Bercoff, N. Benech, and M. Fink, “Coherent plane-wave compounding for very high frame rate ultrasonography and transient elastography,” *IEEE Transactions on Ultrasonics, Ferroelectrics, and Frequency Control*, vol. 56, no. 3, pp. 489–506, Mar. 2009, doi: 10.1109/TUFFC.2009.1067.

[216] C. Hong *et al.*, “GPU code optimization using abstract kernel emulation and sensitivity analysis,” in *Proceedings of the 39th ACM SIGPLAN Conference on Programming Language Design and Implementation - PLDI 2018*, Philadelphia, PA, USA, 2018, pp. 736–751, doi: 10.1145/3192366.3192397.

[217] G. Casasanta and R. Garra, “Towards a Generalized Beer-Lambert Law,” *Fractal Fract*, vol. 2, no. 1, p. 8, Jan. 2018, doi: 10.3390/fractalfract2010008.

[218] T. I. Zohdi, “Modeling and Simulation of Laser Processing of Particulate-Functionalized Materials,” *Arch Computat Methods Eng*, vol. 24, no. 1, pp. 89–113, Jan. 2017, doi: 10.1007/s11831-015-9160-1.

[219] Mattausch Oliver, Makhinya Maxim, and Goksel Orcun, “Realistic Ultrasound Simulation of Complex Surface Models Using Interactive Monte-Carlo Path Tracing,” *Computer Graphics Forum*, vol. 37, no. 1, pp. 202–213, Aug. 2017, doi: 10.1111/cgf.13260.

[220] C. De Boor, “A practical guide to splines, revised Edition, Vol. 27 of Applied Mathematical Sciences,” *Mechanical Sciences, year*, 2001.

[221] MATLAB and S. T. Release, “The MathWorks, Inc., Natick, Massachusetts, United States,” 2012.

[222] SciPy 1.0 Contributors *et al.*, “SciPy 1.0: fundamental algorithms for scientific computing in Python,” *Nat Methods*, Feb. 2020, doi: 10.1038/s41592-019-0686-2.

[223] M. A. Gray, “Sage: A New Mathematics Software System,” *Computing in Science Engineering*, vol. 10, no. 6, pp. 72–75, Nov. 2008, doi: 10.1109/MCSE.2008.154.

[224] T. J. Ypma, “Historical Development of the Newton–Raphson Method,” *SIAM Review*, vol. 37, no. 4, pp. 531–551, Dec. 1995, doi: 10.1137/1037125.

[225] A. Tumeo, N. Gawande, and O. Villa, “A Flexible CUDA LU-Based Solver for Small, Batched Linear Systems,” in *Numerical Computations with GPUs*, V. Kindratenko, Ed. Cham: Springer International Publishing, 2014, pp. 87–101.

[226] M. Parrilla, J. Brizuela, J. Camacho, A. Ibanez, P. Nevado, and C. Fritsch, “Dynamic focusing through arbitrary geometry interfaces,” in *2008 IEEE Ultrasonics Symposium*, Nov. 2008, pp. 1195–1198, doi: 10.1109/ULTSYM.2008.0288.

[227] K. Nagai, “A New Synthetic-Aperture Focusing Method for Ultrasonic B-Scan Imaging by the Fourier Transform,” *IEEE Transactions on Sonics and Ultrasonics*, vol. 32, no. 4, pp. 531–536, Jul. 1985, doi: 10.1109/T-SU.1985.31627.

[228] *Handbook of signal processing systems*. New York, NY: Springer Science+Business Media, LLC, 2018.

[229] J. Nickolls, I. Buck, and M. Garland, “Scalable parallel programming,” in *2008 IEEE Hot Chips 20 Symposium (HCS)*, Aug. 2008, pp. 40–53, doi: 10.1109/HOTCHIPS.2008.7476525.

[230] S. Xu *et al.*, “Taming the ‘Monster’: Overcoming Program Optimization Challenges on SW26010 Through Precise Performance Modeling,” in *2018 IEEE International Parallel and Distributed Processing Symposium (IPDPS)*, Vancouver, BC, May 2018, pp. 763–773, doi: 10.1109/IPDPS.2018.00086.

[231] T. K. F. Da, “2D Alpha Shapes,” in *CGAL User and Reference Manual*, 4.14., CGAL Editorial Board, 2019.

[232] H. Edelsbrunner, D. Kirkpatrick, and R. Seidel, “On the shape of a set of points in the plane,” *IEEE Trans. Inform. Theory*, vol. 29, no. 4, pp. 551–559, Jul. 1983, doi: 10.1109/TIT.1983.1056714.

[233] H. Edelsbrunner and E. P. Mucke, “Three-dimensional Alpha Shapes,” p. 32.

[234] L. Lin, H. Cao, and Z. Luo, “Total focusing method imaging of multidirectional CFRP laminate with model-based time delay correction,” *NDT & E International*, vol. 97, pp. 51–58, Jul. 2018, doi: 10.1016/j.ndteint.2018.03.011.

[235] E. Carcreff, N. Laroche, D. Braconnier, A. Duclos, and S. Bourguignon, “Improvement of the total focusing method using an inverse problem approach,” in *2017 IEEE International Ultrasonics Symposium (IUS)*, Sep. 2017, pp. 1–4, doi: 10.1109/ULTSYM.2017.8092258.

[236] W. Kerr, S. G. Pierce, and P. Rowe, “Investigation of synthetic aperture methods in ultrasound surface imaging using elementary surface types,” *Ultrasonics*, vol. 72, pp. 165–176, Dec. 2016, doi: 10.1016/j.ultras.2016.08.007.

[237] P. Nanekar, A. Kumar, and T. Jayakumar, “SAFT-assisted sound beam focusing using phased arrays (PA-SAFT) for non-destructive evaluation,” *Nondestructive Testing and Evaluation*, vol. 30, no. 2, pp. 105–123, Apr. 2015, doi: 10.1080/10589759.2014.1002837.

[238] T. K. F. Da, S. Loriot, and M. Yvinec, “3D Alpha Shapes,” in *CGAL User and Reference Manual*, 4.14., CGAL Editorial Board, 2019.

[239] K. Fischer, “Introduction to alpha shapes,” *Department of Information and Computing Sciences, Faculty of Science, Utrecht University*, vol. 17, 2000.

[240] P. Hachenberger, “Convex Decomposition of Polyhedra,” in *CGAL User and Reference Manual*, 4.14., CGAL Editorial Board, 2019.

[241] S. Hert and S. Schirra, “2D Convex Hulls and Extreme Points,” in *CGAL User and Reference Manual*, 4.14., CGAL Editorial Board, 2019.

[242] S. Hert and M. Seel, “dD Convex Hulls and Delaunay Triangulations,” in *CGAL User and Reference Manual*, 4.14., CGAL Editorial Board, 2019.

[243] O. Devillers, S. Hornus, and C. Jamin, “dD Triangulations,” in *CGAL User and Reference Manual*, 4.14., CGAL Editorial Board, 2019.

[244] M. Yvinec, “2D Triangulation,” in *CGAL User and Reference Manual*, 4.14., CGAL Editorial Board, 2019.

[245] *The finite element method and applications in engineering using ansys*. New York, NY: Springer Science+Business Media, 2014.

[246] P. T. Bauman and R. H. Stogner, “GRINS: A Multiphysics Framework Based on the libMesh Finite Element Library,” *arXiv:1506.06102 [cs]*, Jun. 2015, Accessed: Jun. 27, 2019. [Online]. Available: http://arxiv.org/abs/1506.06102.

[247] B. S. Kirk, J. W. Peterson, R. H. Stogner, and G. F. Carey, “libMesh : a C++ library for parallel adaptive mesh refinement/coarsening simulations,” *Engineering with Computers*, vol. 22, no. 3–4, pp. 237–254, Dec. 2006, doi: 10.1007/s00366-006-0049-3.

[248] A. Baccigalupi, M. DArco, and A. Liccardo, “Parameters and Methods for ADCs Testing Compliant With the Guide to the Expression of Uncertainty in Measurements,” *IEEE Trans. Instrum. Meas.*, vol. 66, no. 3, pp. 424–431, Mar. 2017, doi: 10.1109/TIM.2016.2644878.

[249] H. Attarzadeh, Y. Xu, and T. Ytterdal, “A Low-Power High-Dynamic-Range Receiver System for In-Probe 3-D Ultrasonic Imaging,” *IEEE Trans. Biomed. Circuits Syst.*, vol. 11, no. 5, pp. 1053–1064, Oct. 2017, doi: 10.1109/TBCAS.2017.2716836.

[250] G. T. Schuster, *Seismic interferometry*. Cambridge ; New York: Cambridge University Press, 2009.

[251] C. Zhu, R. H. Byrd, P. Lu, and J. Nocedal, “Algorithm 778: L-BFGS-B: Fortran subroutines for large-scale bound-constrained optimization,” *ACM Transactions on Mathematical Software*, vol. 23, no. 4, pp. 550–560, Dec. 1997, doi: 10.1145/279232.279236.

9 APPENDIX

Algorithm A1 example of TFM implementation

```
    Assumtions: thread number is an active aperture, for example, 128 elements (threadidx.x ∈ 0…127)
    pixel_pos – (x,y) – ROI position z – is a wave propagation time in sample
    glob_tr_pos – transducer element position (x,y) and z – t0 (time to first surface point)
    blockIdx.x – the result number/point, the request data is given by (x,y) point list
    DATA_PITCH – number of samples in one time trace
1  __shared__ float suma[128];
2  __shared__ float2 trpos[128];
3  const int tid = threadIdx.x;
4  suma[tid] = 0;
5  trpos[tid] = glob_tr_pos[tid];
6  float2 fp = focus_points[blockIdx.x];
7  __syncthreads();
8   for a = 0..127
9   int sample = (int)((norm(fp.x - trpos[tid].x,fp.y - trpos[tid].y) + norm(fp.x - trpos[a].x,fp.y - trpos[a].y))  * Cinv * SAMPLING_RATE_MHZ);
10 if ( sample ∈  (0..DATA_PITCH) )
11   suma[tid] += data[ (tid * DATA_PITCH + sample) + (128*DATA_PITCH)*a ];
12 end if
13 end for

14 for s = 64, s > 0, s>>= 1
15   __synthreads();
16  if (tid < s)
17    suma[tid] = suma[tid] = suma [tid + s];
18  end if
19 end for
20 if tid == 0
21   atomicAdd(&result[blockIdx.x],suma[0])
22 end if
```

Algorithm A2 Forward step1 CUDA pseudocode

```
    Assumptions: thread block size 1024 (threadIdx.x ∈ 0…1023)
    uint16_t* evolution_data // propagation model quadrant (1024x1024 size)
    uint3 * focus_emit_points // (x,y,z) – boundary points (x,y) , z – time offset
    uint32_t world // the world table in unitless coordinate system (4096x4096 size)
```

```
uint3 ep = focus_emit_points[blockIdx.x];
uint16_t tmp;
for i = 0 < 1024
 uint16_t ld = evolution_data[1024*i + threadIdx.x];
  __syncthreads();
 int (x,y) = (ep.x + threadIdx.x, ep.y + i);  // right pixel bottom ROI
  if  (x,y) ∈ world
   tmp = ep.z + ld;
   atomicMin(&world[y * 4096 + x],tmp);
 end if

 int (x,y) = (ep.x + threadIdx.x, ep.y - i);  // right top ROI
 if  (x,y) ∈ world
   tmp = ep.z + ld;
   atomicMin(&world[y * 4096 + x],tmp);
 end if

 int (x,y) = (ep.x - threadIdx.x, ep.y + i);  // left bottom ROI
 if  (x,y) ∈ world
   tmp = ep.z + ld;
   atomicMin(&world[y * 4096 + x],tmp);
 end if
 int (x,y) = (ep.x - threadIdx.x, ep.y - i); // left top ROI
 if  (x,y) ∈ world
   tmp = ep.z + ld;
   atomicMin(&world[y * 4096 + x],tmp);
end if
```

Algorithm A3. The focusing step of proposed method (similar to TFM)

Assumtions: **thread number is an active aperture for example 128 elements (threadidx.x ∈ 0…127)**

Boundary points are given by group of 128 (optimisation propose).

pixel_pos – (x,y) – ROI position z – is a wave propagation time in sample

glob_tr_pos – transducer element position (x,y) and z – t0 (time to first surface point)

blockIdx.x – the result number/point, the request data is given by (x,y) point list

DATA_PITCH – number of samples in one time trace

```
1  const int tid = threadIdx.x;
2  __shared__ float pixel_value[128];
```

```
__shared__ float3 pixel_pos;
__shared__ float2 bndr[128];

float3 tr_pos = glob_tr_pos[threadIdx.x];

pixel_value[threadIdx.x] = 0;

if (threadIdx.x == 0)
  pixel_pos = focus_points[blockIdx.x];
end if
__syncthreads();
 if (pixel_pos.z >= ∞){
  if (tid == 0){
    result[blockIdx.x] = 0;
    return
    end if
end if

float tmin = ∞;int tmin_idx = ∞
for i = 0 < (boundary_points_len >> 7)
  bndr[tid] = boundary_points[128*i + tid];
  __syncthreads();
  for j = 0..127
     float a = sqrt( (pixel_pos.x - bndr[jval].x)² + (pixel_pos.y - bndr[jval].y)² ) * C2inv;
    float b = sqrt ( ((bndr[jval].x  - tr_pos.x)² + (bndr[jval].y - tr_pos.y)² ) * C1inv
    float t = a + b +  pixel_pos.z + t0;
    if (t < tmin)
      tmin = t; tmin_idx = 128*i + jval
    end if
  end for
end for
// processing remainder
int mmax = boundary_points_len - ((boundary_points_len >> 7)*128);
int mof = ((boundary_points_len >> 7)*128);
if (tid < mmax)
  bndr[tid] = boundary_points[mof + tid];
end if
__syncthreads();
for j = 0 < mmax
   float a = sqrt( (pixel_pos.x - bndr[jval].x)² + (pixel_pos.y - bndr[jval].y)² ) * C2inv;
   float b = sqrt ( ((bndr[jval].x  - tr_pos.x)² + (bndr[jval].y - tr_pos.y)² ) * C1inv
```

```
     42   float t = a + b +  pixel_pos.z + t0;
     43     if (t < tmin)
     44       tmin = t; tmin_idx = 128*i + jval
     45     end if
     46 end for
     47 int sample = tmin*SAMPLING_RATE_MHZ;
     48 if ( sample ∈  (0..DATA_PITCH) )
     49        pixel_value[tid] =   data[  (tid  *  DATA_PITCH  +  sample)  +
(128*DATA_PITCH)*emmiter ];
     50 for s = 64, s > 0, s>>= 1
     51   __synthreads();
     52  if (tid < s)
     53    suma[tid] = suma[tid] = suma [tid + s];
     54  end if
     55 end for
     56 if tid == 0
     57   atomicAdd(&result[blockIdx.x],suma[0])
     58 end if
```

SL344. 2020-*-*, * leidyb. apsk. l. Tiražas * egz. Užsakymas * .
Išleido Kauno technologijos universitetas, K. Donelaičio g. 73, 44249 Kaunas
Spausdino leidyklos „Technologija“ spaustuvė, Studentų g. 54, 51424 Kaunas